

**Metallic nanoparticle-graphene quantum dot nanocomposites for the
electrochemical detection of methyl parathion**

by

Sinayo Ndwabu

Submitted in fulfilment of the academic requirements of

Master of Science

in

Chemistry

School of Chemistry and Physics

College of Agriculture, Engineering and Science

University of KwaZulu-Natal

Durban

South Africa

December 2017

PREFACE

The research contained in this dissertation was completed by the candidate while based in the Discipline of Chemistry, School of Chemistry and Physics of the College of Agriculture, Engineering and Science, University of KwaZulu-Natal, Westville campus, South Africa. The research was financially supported by the Department of Science and Technology and National Research Foundation (DST-NRF).

The contents of this work have not been submitted in any form to another university and, except where the work of others is acknowledged in the text, the results reported are due to investigations by the candidate.

Signed: Dr N. Nombona (supervisor)

Date: 13 December 2017

DECLARATION 1: PLAGIARISM

I, Sinayo Ndwabu, declare that:

- (i) the research reported in this dissertation, except where otherwise indicated or acknowledged, is my original work;
- (ii) this dissertation has not been submitted in full or in part for any degree or examination to any other university;
- (iii) this dissertation does not contain other persons' data, pictures, graphs or other information, unless specifically acknowledged as being sourced from other persons;
- (iv) this dissertation does not contain other persons' writing, unless specifically acknowledged as being sourced from other researchers. Where other written sources have been quoted, then:
 - a) their words have been re-written but the general information attributed to them has been referenced;
 - b) where their exact words have been used, their writing has been placed inside quotation marks, and referenced;
- (v) where I have used material for which publications followed, I have indicated in detail my role in the work;
- (vi) this dissertation is primarily a collection of material, prepared by myself, published as journal articles or presented as a poster and oral presentations at conferences. In some cases, additional material has been included;
- (vii) this dissertation does not contain text, graphics or tables copied and pasted from the Internet, unless specifically acknowledged, and the source being detailed in the dissertation and in the References sections.

Signed: Sinayo Ndwabu

Date: 13 December 2017

ABSTRACT

This work reports on the detection of methyl parathion (MP) on electrodes constructed or decorated with graphene based nanomaterials. The sensing nanomaterials used include graphene quantum dots (GQDs), metal oxide [(MO): Cu₂O, NiO, Al₂O₃ and MnO₂] and metal hydroxide [(MOH): Cu(OH)₂, Ni(OH)₂, Al(OH)₃ and Mn(OH)₂] nanoparticles (NPs). The nanomaterials were synthesized using prescribed procedures. Characterisation of the materials was achieved using various techniques including transmission electron microscope (TEM) and scanning electron microscope (SEM). The MO NPs sizes were determined by TEM to be between 31 nm and 70 nm whereas the MOH NPs sizes were found to be smaller with particle sizes ranging between 20 nm and 55 nm. The nanocomposites of GQDs/MO and GQDs/MOH were synthesized and characterised using SEM. SEM revealed that the MO and MOH nanoparticles were well-dispersed on the surface as well as within the graphene quantum dot sheets. The following electrodes were prepared: a graphene quantum dot paste electrode (GQDPE) decorated with either MO or MOH NPs and a glassy carbon electrode (GCE) modified with either GQDs/MO or GQDs/MOH nanocomposites. The electrochemical characterisation of these electrodes revealed that faster electron transfer kinetics occurred at the GQDPE. The ability of the modified electrodes to electrochemically detect MP was evaluated using cyclic voltammetry and the results revealed that the modified GQDPE did not exhibit any electrocatalytic performance. However, the GCE modified with the GQDs/MOH nanocomposite showed the best catalytic activity with lower detection limits compared to GQDs/MO modified electrodes. Electrochemical characterisation further revealed that amongst all of the metal based nanocomposites, GQDs/Cu(OH)₂ exhibited the best catalytic activity with the highest sensitivity towards MP. This work demonstrated for the first time that these sensing nanomaterials have a favourable catalytic behaviour, ideal for the detection of organophosphate pesticides.

ACKNOWLEDGEMENTS

The writing of this thesis has been one of the most significant academic challenges I have ever had to face and without the love, support, patience and guidance of the following people, I don't see how I would have completed this study. It is to them that I owe my deepest gratitude.

Firstly thank you to God for seeing me through every day!

Dr Nolwazi Nombona my supervisor, thank you for taking me under your wing through this study despite your other professional commitments. Your wisdom, knowledge and commitment towards excellence is inspiring. Dr Mbuso Mlambo thank you for lending a helping hand whenever necessary.

The National Research Foundation (NRF) and Department of Science and Technology (DST) for the financial support.

To my late grandparents I hope you looking down and proud of the woman I have become.

My amazing parents Mfuneko and Ndileka Ndwabu your unconditional love and support is unmeasurable. Mother I do not know where I would be if it wasn't for your prayers ndiyabulela Mazondi. Xhanga, Khwetshube, Mhlamb' olali ntaka I can never thank you enough for working so hard for us ndiyabulela daddy.

The awesome trio, my day ones, my brothers Gugu, Toto and Lolo I am so grateful for you and I am so happy to be doing life with you, Thank you for the laughter, love and support.

To my friends thank you for always listening when I needed to vent. Dalingwe you so supportive just all-around amazing!

DEDICATION

To my family for supporting and encouraging me to believe in my dreams

TABLE OF CONTENTS

PREFACE	i
DECLARATION 1: PLAGIARISM	ii
ABSTRACT	iii
ACKNOWLEDGEMENTS	iv
DEDICATION	v
ABBREVIATIONS	ix
LIST OF SYMBOLS	xiii
LIST OF FIGURES	xiv
LIST OF TABLES	xviii
LIST OF SCHEMES	xix
Chapter 1 Literature review	1
1. Introduction	2
1.1 Water pollution	2
1.2.1 Brief history of water pollution	2
1.3 Pesticides: history and perspective	3
1.3.1 Organophosphate Pesticides	4
1.3.2 Techniques used for pesticide detection	5
1.4 Graphene	7
1.4.1 Electronic properties of graphene	9
1.4.2 Graphene oxide (GO) and reduced graphene oxide (rGO)	9
1.4.3 Graphene quantum dots (GQDs)	12
1.5 Graphene based electrodes as pesticide sensors	13
1.5.1 Graphene based nanomaterials for pesticide sensors	14
1.6 Metal based nanomaterials as pesticide sensors	19
1.6.1 Nickel oxide (NiO) and nickel hydroxide (Ni(OH)₂) nanoparticles as sensor materials	20
1.6.2 Copper oxide (Cu₂O) and copper hydroxide (Cu(OH)₂) nanoparticles as sensor material	22
1.6.3 Manganese oxide (MnO₂) and manganese hydroxide (Mn(OH)₂) nanoparticles as a sensor material	24
1.6.4 Aluminium oxide (Al₂O₃) and aluminium hydroxide (Al(OH)₃) nanoparticles as a sensor material	26
1.7 Aims and objectives of this work	28
1.7.1 Aims	28
1.7.2 Objectives	29

2. Experimental	39
2.1 Materials and solvents	39
2.2 Equipment	39
2.3 Electrochemical methods	40
2.4 Synthesis of graphene based materials	41
2.4.1 Graphene oxide (GO) and graphene quantum dots (GQDs)	41
2.5 Synthesis of metal oxide nanoparticles	42
2.5.1 Copper oxide (Cu₂O) nanoparticles	42
2.5.2 Nickel oxide (NiO) nanoparticles	43
2.5.3 Aluminium oxide (Al₂O₃) nanoparticles	43
2.5.4 Manganese oxide (MnO₂) nanoparticles	43
2.6 Synthesis of metal hydroxide nanoparticles	44
2.6.1 Copper hydroxide Cu(OH)₂ nanoparticles	44
2.6.2 Nickel hydroxide (Ni(OH)₂) nanoparticles	44
2.6.3 Aluminium hydroxide (Al(OH)₃) nanoparticles	44
2.6.4 Manganese hydroxide (Mn(OH)₂) nanoparticles	45
2.8 References	46
Results and discussion	49
3. Synthesis and characterisation of nanomaterials	50
3.1 Synthesis of graphene quantum dots (GQDs)	50
3.2 Synthesis of metal oxide (MO) and metal hydroxide (MOH) nanoparticles	50
3.2.1 Synthesis of GQDs-MO or GQDs-MOH composites	52
3.3 Characterisation of synthesized nanomaterials	52
3.3.1 UV-vis spectroscopy of graphene nanoparticles	52
3.3.2 Fourier transform infrared analysis (FTIR) of GQDs	54
3.3.3 Raman analysis of graphene nanoparticles	55
3.4 Characterisation of metal oxide and metal hydroxide nanoparticles	57
3.4.1 FTIR spectra for copper nanoparticles	57
3.4.2 FTIR spectra for nickel nanoparticles	58
3.4.3 FTIR spectra for aluminium nanoparticles	58
3.4.4 FTIR spectra for manganese nanoparticles	59
3.5 X-ray diffraction (XRD) spectra	60
3.5.1 XRD pattern for graphene nanoparticles	60
3.5.2 XRD pattern for metal nanoparticles	61
3.6 TEM and SEM/EDX analysis of nanomaterials	65

3.6.1 TEM and SEM/EDX analysis of GQDs	66
3.6.2 TEM and SEM/EDX analysis of metal oxide NPs.....	67
3.6.3 TEM and SEM/EDX analysis of metal hydroxides.....	73
3.7 Effects of particle size in catalytic behaviour	79
3.8 Thermal gravimetric analysis (TGA) of nanomaterials	80
3.8.1 TGA profile of graphene NPs	80
3.8.2 TGA profile of metal nanoparticles.....	81
3.8.2.4 TGA profile of manganese NPs.....	84
3.9 References.....	86
4. Electrode fabrication and electrocatalysis	92
4.1 Electrode fabrication	92
4.1.1 Electrode characterisation	92
4.2 Electrocatalysis.....	97
4.2.1 Electrochemical behaviour of methyl parathion (MP) on GQDPE.....	97
4.2.2 Electrochemical behaviour of MP on MO or MOH modified electrodes	99
4.2.3 Influence of MP concentration.....	109
4.4 References.....	115
5.1 Conclusion	118
5.2 Future work recommendation	118

ABBREVIATIONS

0D	zero-dimensional
1D	one-dimensional
2D	two-dimensional
3D	three-dimensional
4-AMP	4-aminophenol
4-CP	4- chlorophenol
4-NP	4- nitrophenol
AChE	acetylcholinesterase
Ag	silver
Al	aluminium
BPA	bisphenol A
BPF	1,1 bisphenylacetyl ferrocenele
BUA	bottom-up approach
CC	catechol
CeO ₂	cerium oxide
Co	cobalt
CoTCPP	cobalt porphyrin
CO ₂	carbon dioxide
CG	carboxylic graphene
CH ₄	methane
CP	chlorpyrifos
CPE	carbon paste electrode
CNTs	carbon nanotubes
CS	chitosan
Cu	copper
CV	cyclic voltammetry
DDT	dichlorodiphenyltrichloroethane
DHB	dihydroxybenzene

DHPID	2- (3,4 dihydroxyphenethyl isoindoline) 1,3 dione
DFT	density functional theory
DMF	dimethylformamide
DTC	dithiocarbamate
EC	electrochemical
E_{pa}	anodic potential
E_{pc}	cathodic potential
EDX	energy dispersive X-ray
EIS	electrolyte insulator silicon
EMIMPF6	1-ethyl-3-methylimidazolium hexafluorophosphate
ES	endosulfan
FeCN	ferricyanide
FCC	face centred cubic
FT	fenitrothion
FTIR	fourier transform infrared spectroscopy
GCE	glassy carbon electrode
GHGs	greenhouse gases
GO	graphene oxide
GQDPE	graphene quantum dot paste electrode
GQDs	graphene quantum dots
GR	graphene
GrO	graphite oxide
GSH	gluthathione
HX	hydroxylamine
IARC	international Agency for Research on Cancer
I_{pa}	anodic peak current
I_{pc}	cathodic peak current
JCPDS	joint Committee on Powder Diffraction standards
LACC	laccase
LD	lethal dose

LDHS	layered double hydroxide
LOD	limit of detection
LOQ	limit of quantification
LPCVD	low pressure chemical vapour deposition
MEMS	micromechanical systems
Mn	manganese
ML	malathion
MO	metal oxide
MOH	metal hydroxide
Mp	mesoporous
MP	methyl parathion
MWCNTs	multiwalled carbon nanotubes
NC	nanocomposite
NH ₄ OH	ammonium solution
NF	nafion
Nickel	nickel
NMs	nanomaterials
NPs	nanoparticles
NRs	nanoribbons
OPs	organophosphates
OPH	organophosphorus hydrolase
PA	Paris agreement
PAM	pralodoxime
PB	prussian blue
PBS	phosphate buffer solution
PCBs	polychlorinated biphenyls
PDA	polydopamine
PL	photoluminescence
PLD	pulsed lased deposition
PP	polypyrrol

Pt	platinum
RC	resorcinol
rGO	reduced graphene oxide
SA	South Africa
SAWS	South African weather service
SDA	size distribution analysis
SEM	scanning electron microscope
SERS	surface-enhanced raman scattering
SPE	solid phase extraction
TEM	transmission electron microscope
TDA	top-down approach
TGA	thermal gravimetric analysis
TRGO	thermally reduced graphene oxide
UNFCCC	United Nations framework convention on climate change
UV-vis	ultraviolet visible spectroscopy
VOCs	volatile organic compounds
XRD	X-ray Diffraction

LIST OF SYMBOLS

Å	angstrom
α	alpha
β	beta
Δ	delta
γ	gamma
μ	micro
ν	scan rate
θ	theta

LIST OF FIGURES

Fig 1.1: Schematic representation of graphene and its derivatives: (a) graphene 2D, (b) fullerene 0D, (c) nanotube 1D, (d) graphite 3D and (e) quantum dots 0D.....	8
Fig1.2: Structure of graphene oxide.	10
Fig 1.3: Structure of graphene quantum dots.....	12
Fig 3.1: UV-vis (a) and emission (b) spectra for GQDs.....	53
Fig 3.2: Jablosnki diagram showing (a) absorption, (b) internal conversion and vibrational relaxation and (c) fluorescence processes.....	54
Fig 3.3: FTIR spectra of (a) GO and (b) GQDs.....	55
Fig 3.4: The Raman Spectra of (a) Gr; (b) GO and (c) GQDs.	56
Fig 3.5: FTIR spectra of (a) Cu ₂ O and (b) Cu(OH) ₂ NPs.....	57
Fig 3.6: FTIR spectra of (a) NiO and (b) Ni(OH) ₂ NPs.	58
Fig 3.7: FTIR spectra of (a) Al ₂ O ₃ and (b) Al(OH) ₃ NPs.....	59
Fig 3.8: FTIR spectra of (a) MnO ₂ and (b) Mn(OH) ₂ nanoparticles.	60
Fig 3.9: XRD spectra of (a) Gr, (b) GO (insert) and (c) GQDs.....	61
Fig 3.10: XRD spectra of (a) Cu ₂ O and (b) Cu(OH) ₂ NPs.....	62
Fig 3.11: XRD spectra of (a) NiO and (b) Ni(OH) ₂ NPs.....	63
Fig 3.12: XRD spectra of (a) Al ₂ O ₃ and (b) Al(OH) ₃ NPs.	64
Fig 3.13: XRD spectra of (a) MnO ₂ and (b) Mn(OH) ₂ NPs.	65
Fig 3.14: (a) TEM image, (b) SDA plot, (c) SEM image and (d) EDX spectrum of GQDs. ...	66
Fig 3.15: (a) TEM image, (b) SDA plot, (c) SEM image, (d) EDX spectrum of Cu ₂ O NPs and (e) SEM image of GQDs Cu ₂ O- NC.....	68

Fig 3.16: (a) TEM image, (b) SDA plot, (c) SEM image, (d) EDX spectrum of NiO NPs and (e) SEM image of GQDs-NiO NC.....	69
Fig 3.17: (a) TEM image, (b) SDA plot, (c) SEM images (insert: at nanoscale), (d) EDX spectrum of Al ₂ O ₃ NPs and (e) SEM image of GQDs-Al ₂ O ₃ NC.	71
Fig 3.18: (a) TEM image, (b) SDA plot, (c) SEM images (insert: at nanoscale), (d) EDX spectrum for MnO ₂ NPs and (e) SEM image of GQDs-MnO ₂ NC.....	72
Fig 3.19: (a) TEM image, (b) SDA plot, (c) SEM image and (d) EDX spectrum for Cu(OH) ₂ NPs and (e) SEM image of GQDs-Cu(OH) ₂ NC.....	74
Fig 3.20: (a) TEM image, (b) SDA plot (c) SEM images (insert: at nanoscale), (d) EDX spectrum of Ni(OH) ₂ NPs and (e) SEM image of GQDs-Ni(OH) ₂ NC.	75
Fig 3.21: (a) TEM image, (b) SDA plot, (c) SEM image, (d) EDX spectrum of Al(OH) ₃ NPs and (e) SEM image of GQDs-Al(OH) ₃ NC.	77
Fig 3.22: (a) TEM image, (b) SDA plot, (c) SEM image, (d) EDX spectrum of Mn(OH) ₂ NPs and (e) SEM image of GQDs-Mn(OH) ₂ NC.....	78
Fig 3.23: TGA profile of (a) Gr, (b) GO and (c) GQDs.	81
Fig 3.24: TGA profile of (a) Cu ₂ O and (b) Cu(OH) ₂ NPs.	82
Fig 3.25: TGA profile of (a) NiO and (b) Ni(OH) ₂ NPs.	83
Fig 3.26: TGA profile of (a) Al ₂ O ₃ and (b) Al(OH) ₃ NPs.	84
Fig 3.27: TGA profile of (a) MnO ₂ and (b) Mn(OH) ₂ NPs.....	85
Fig 4.1: Cyclic voltammograms of (a) GQDPE (b) (i) bare and (ii) GQDs/GCE.....	93
Fig 4.2: Cyclic voltammograms of (a) (i) GQDs/GCE (ii) GQDs/Cu ₂ O/GCE (iii) GQDs/Cu(OH) ₂ /GCE, (b) (i) GQDs/GCE (ii) GQDs/NiO/GCE (iii) GQDs/Ni(OH) ₂ /GCE, (c) (i) GQDs/GCE (ii) GQDs/Al ₂ O ₃ /GCE (iii) GQDs/Al(OH) ₃ /GCE and (d) (i) GQDs/GCE (ii)	

GQDs/MnO₂/GCE (iii) GQDs/Mn(OH)₂/GCE in 5 mM [Fe(CN)₆]³⁻/[Fe(CN)₆]⁴⁻ containing 0.1 M KCl solution.....94

Fig 4.3: Cyclic voltammogram of GQDPE in 0.1 M PBS in the (a) absence and (b) presence of MP.97

Fig 4.4: (a) Cyclic voltammograms of 0.2 μM MP at different scan rates (10 - 100 mV.s⁻¹) on GQDPE in 0.1 M PBS at pH 7, (b) corresponding peak current variation with square root of scan rate and (c) corresponding logarithm peak potential variation with logarithm of scan rate.....99

Fig 4.5: Cyclic voltammograms of 0.2 μM MP on (i) bare GCE, (ii) GQDs/Cu₂O/GCE and (iii) GQDs/Cu(OH)₂/GCE, in 0.1 M PBS..... 100

Fig 4.6: Plot of square root of scan rate vs peak current for (a) GQDs/Cu₂O/GCE and (b) GQDs/Cu(OH)₂/GCE. Plot of log v vs log I_{pa} for (c) GQDs/Cu₂O/GCE and (d) GQDs/Cu(OH)₂/GCE..... 101

Fig 4.7: Cyclic voltammograms of 0.2 μM MP on (i) bare GCE, (ii) GQDs/NiO/GCE and (iii) GQDs/Ni(OH)₂/GCE in 0.1 M PBS..... 102

Fig 4.8: Plot of square root of scan rate vs peak current for (a) GQDs/NiO/GCE and (b) GQDs/Ni(OH)₂/GCE. Plot of log v vs log I_{pa} for (c) GQDs/NiO/GCE and (d) GQDs/Ni(OH)₂/GCE. 103

Fig 4.9: Cyclic voltammograms of 0.2 μM MP on (i) bare GCE, (ii) GQDs/Al₂O₃/GCE and (iii) GQDs/Al(OH)₃/GCE in 0.1 M PBS..... 104

Fig 4.10: Plot of square root of scan rate vs peak current for (a) GQDs/Al₂O₃/GCE and (b) GQDs/Al(OH)₃/GCE. Plot of log v vs log I_{pa} for (c) GQDs/Al₂O₃/GCE and (d) GQDs/Al(OH)₃/GCE. 105

Fig 4.11: Cyclic voltammograms of 0.2 μM MP on (i) bare GCE, (ii) GQDs/MnO₂/GCE and (iii) GQDs/Mn(OH)₂/GCE in 0.1 M PBS..... 106

Fig 4.12: Plot of square root of scan rate vs peak current for (a) GQDs/MnO ₂ /GCE and (b) GQDs/Mn(OH) ₂ /GCE. Plot of log v vs log I_{pa} for (c) GQDs/MnO ₂ /GCE and (d) GQDs/Mn(OH) ₂ /GCE.....	107
Fig 4.13: (a) Cyclic voltammograms of GQDPE in 0.1 M PBS containing different concentrations of MP and (b) the corresponding MP concentration vs current plot.	109
Fig 4.14: Cyclic voltammograms of (a) GQDs/Cu(OH) ₂ /GCE and (b) GQDs/Cu ₂ O/GCE in 0.1 M PBS containing different concentrations of MP.....	111
Fig 4.15: Cyclic voltammograms of (a) GQDs/Ni(OH) ₂ /GCE and (b) GQDs/NiO/GCE in 0.1 M PBS containing different concentrations of MP.....	112
Fig 4.16: Cyclic voltammograms of (a) GQDs/Al(OH) ₃ /GCE and (b) GQDs/Al ₂ O ₃ /GCE in 0.1 M PBS containing different concentrations of MP.....	113
Fig 4.17: Cyclic voltammograms of (a) GQDs/Mn(OH) ₂ /GCE and (b) GQDs/MnO ₂ /GCE in 0.1 M PBS containing different concentrations of MP.....	114

LIST OF TABLES

Table 1.1: International Agency for Research on Cancer human carcinogenic classifications.	5
Table 1.2: Developed graphene based electrochemical sensors for pesticide detection.....	14
Table 1.3: Developed nickel oxide/hydroxide electrochemical sensors for pesticide detection.	21
Table 1.4: Developed copper oxide/hydroxide electrochemical sensors for pesticide detection.....	23
Table 1.5: Developed manganese oxide/hydroxide electrochemical sensors for pesticide detection.....	25
Table 1.6: Developed aluminium oxide/hydroxide electrochemical sensors for pesticide detection.....	27
Table 3 1: Particle sizes of MO and MOH nanoparticles.	79
Table 4.1: The electroactive surface area and ΔE values of the modified electrodes.....	96
Table 4.2: ΔE , current ratios and slope of $\log I_{pc}$ vs $\log v$ for MP on GQDs/GCE modified with relevant metal nanoparticles.	108
Table 4.3: LODs, LOQs and sensitivities for MP detection on modified electrodes.....	110

LIST OF SCHEMES

Scheme 2.1: Synthesis of GQDs via a modified Hummer's method.....	42
Scheme 4.1: The electrochemical reaction of MP.....	98

Chapter 1

Literature

review

1. Introduction

1.1 Water pollution

Access to safe drinking water is a basic human right which is being threatened by pollution. Water pollution poses danger to humans, plants, and animals.¹ South Africa is generally a water scarce country with the quality of this water being reduced by pollution.² Water scarcity in South Africa has been escalated by pollution caused by human population growth, industrialization and urbanization.² There are various types of water pollutants including insecticides, herbicides, pollutants due to livestock operations, volatile organic compounds (VOCs), heavy metals and chemical waste.³ A major problem that water contamination poses to human and other living organisms relates to water quantity and quality. The change in water quality and quantity is usually associated with human activity, including mining and agriculture which release toxic substances into rivers and other water resources.⁴ On the other hand climate change threatens water security as it leads to limited water supply.⁵

1.2.1 Brief history of water pollution

The importance of clean water was not understood until the second half of the 19th century.⁶ In ancient Rome, sewers used to carry human waste into the Tiber river, this led to typhoid and cholera outbreaks.⁷ Pollution started in the pre-historic era from when man created fire to when farming and development of settlements began. Pollution increased drastically in the mid-1940s towards the end of World War II.⁷ This was due to the fact that manufacturers in various industries started using synthetic material such as polychlorinated biphenyls (PCBs) and pesticides.⁸ PCBs were used as lubricants in electrical systems but the poor disposal of PCB-containing appliances led to PCB contamination. Pesticides such as dichlorodiphenyltrichloroethane (DDT) were used as insecticides which at certain levels of

exposure led to human poisoning and affected foetal development.⁹ Pesticides are major environmental contaminants mainly because of the way they are administered which makes them difficult to contain in their targeted environment.¹⁰ These materials are non-biodegradable and exposed humans have increased risk of cancer¹¹, birth defects¹⁰ and mental disorders.¹⁰

1.3 Pesticides: history and perspective

The history of pesticide development and its use is the clue to understanding how and why pesticides are an environmental problem to aquatic systems. This will give an understanding of why this problem remains in developing countries.¹² Paris green or copper (II) acetate triarsenite or copper (II) acetoarsenite was the first chemical pesticides to be used at the end of 19th century in the United States. By the 20th century Paris green led to human poisoning and illnesses such as cancer as a result farmers used other pest controls¹², such as sulphur, calcium arsenate and nicotine sulphate which had less harmful effects.¹¹

The availability of DDT in 1945 for agricultural use opened a new period for pest control which led to its wide use and development of other synthetic insecticides. DDT has a broad-spectrum activity against pests, however its persistence in the environment became a major disadvantage.¹¹ The South African government took control by banning the use of DDT in 1996 due to environment concerns, but four years later its use was reinstated based on the increase in malaria death cases.¹³ Alternative chemicals such as aldrin and dieldrin were used due to their inexpensiveness and effectiveness, however with continuous use some pests developed resistance.¹⁴ As a result of the resistance non-targeted plants and animals were affected and pesticide residues were found in non-targeted destinations, leading to human poisoning characterised by headaches, dizziness and gastrointestinal disturbances.^{11,14}

1.3.1 Organophosphate Pesticides

Organophosphate compounds (OPs) are chemicals that have been historically used as pesticides and warfare agents.¹² These chemicals are acetylcholinesterase inhibitors and have detrimental effects on the human nervous system. OP neurotoxins such as sarin, malathion and diazinon were first used at the end of World War II as chemical weapons. The OP chemical weapons used during the Gulf war are believed to have caused some of the symptoms of Gulf War syndrome.¹⁵ These symptoms include muscle pain, short term memory loss, tingling and numbness of limbs and respiratory problems. OP gases were also used in the 1995 terrorist attack in Tokyo.¹⁶ OPs also penetrate the placenta causing damage to the foetus. The International Agency for Research on Cancer (IARC) classifies OPs into five carcinogenic groups: 1, 2A, 2B, 3 and 4. The highly carcinogenic substances are categorized into group 1 while the substances that are least carcinogenic are group 4. Table 1.1 shows some of these carcinogenic substances.¹⁷ The lethal dose (LD) is used to define the level of toxicity and is expressed in milligrams of product per kilogram of body weight (mg/kg)¹⁸. LD₅₀ is a single dose of a carcinogen when orally or dermally applied to test animals that results in 50 percent deaths of the animals. The list of carcinogens were tabulated to educate people about cancer and its potential causes.¹⁸ Carcinogens do not cause cancer in every case because they have different levels of cancer-causing potential.¹⁹ For an individual, the risk of developing cancer depends on various factors, including the duration and intensity of exposure, how one is exposed to the carcinogen and their genetic make-up.¹⁹ Methyl parathion (MP) also known as “cotton-poison” is a slightly hazardous group 3 carcinogenic substance and has a LD₅₀ ranging from 2000 to 5000 mg/kg. It was developed in the 1940s and comes in various forms which include dust, emulsion, granular and wettable powder. It is applied to a number of crops including alfalfa, cotton, barley, soy beans, sunflower, wheat, and sorghum.^{13,9}

Table 1 1: International Agency for Research on Cancer human carcinogenic classifications.¹⁷

Group	Toxicity	LD ₅₀ for the rat body weight (mg/kg)		Carcinogenic substances
		Oral	Dermal	
1	Extremely hazardous	<5	<50	Benzo[a] pyrene
2A	Highly hazardous	5 -50	50 - 200	DDT/ Malathion
2B	Moderately hazardous	200 - 2000	200 - 2000	Ethyl parathion
3	Slightly hazardous	2000 - 5000	2000 - 5000	Methyl Parathion 4-nitrobiphenyl Hydrogen peroxide
4	Unlikely to hazardous	>5000	> 5000	Caprolactam

Regulations were implemented to decrease the detrimental effects caused by the use of these pesticides. These regulations included limiting human exposure by wearing protective clothing (gloves, oxygen masks, etc) when administering the pesticide.²⁰ Methyl parathion has a broad spectrum activity against various pests but its non-selective nature makes other living organisms including humans and animals vulnerable.¹¹ The MP's environmental persistence and potential bioaccumulation is still a major issue.^{9,21}

1.3.2 Techniques used for pesticide detection

Environmental monitoring is an important process that requires frequent practice to minimize health hazards.²² Not only is the process extremely vital for all living things, but it is also very

complicated and expensive to achieve.²³ The determination of environmental contaminants or pollutants, is generally carried out using analytical techniques such as chromatography and spectroscopy.²⁴ The analytical techniques are accurate and sensitive but they require sophisticated and expensive instrumentation to be operated by an expert. These techniques are also labour intensive, time-consuming and on-site monitoring is a struggle.²⁵ In order to overcome these odds, portable, cost-effective, robust, electrochemical devices have been developed for the rapid and sensitive analysis of pollutants such as a pesticide.²⁶

1.3.2.1 Electrochemical (EC) sensors

Sensors are devices that detect and respond to a physical or optical signal. They convert a physical parameter into an electrical signal.²⁷ The most common sensor is the thermometer which converts temperature into numerical values. Sensors have been widely used in various fields including science²⁸, engineering²⁹ and medicine.³⁰ Different types of sensors are used for different applications therefore, a sensor must be fabricated and its properties tuned according to its application.^{31,32} The improvement of electrochemical sensors to give rapid response times, low cost, superior sensitivity and selectivity is an on-going research effort.²⁶ EC sensors have found extensive applications in various industries. The most common examples of such sensors include the glucometer and the pH meter.²⁷

Nanotechnology have found applications in the development of electrochemical sensors. Nanomaterials are materials that are manufactured at nanoscale with at least one dimension less than 100 nm.³³ Nanomaterials include nanotubes, nanowires, nanoparticles, and nanocrystals. They have a unique surface chemistry depending on their synthesis and exhibit distinct thermal, electrical and optical properties. These properties play an important role in enhancing their sensitivity, response times and detection limits in nanosensors.^{28,4} Nanosensors are generally devices with spectacular features such as their portability, green nature and cost

effectiveness. Nanosensors are nanomaterial based sensors that detect molecules at the same or even smaller scale.³⁴ Their applications include detecting various chemicals for environmental monitoring³⁵ and medical diagnostics.³⁴

For instance silica coated graphene for the removal of pesticide pollutants in water was reported by Yang and co-workers.³⁶ A sensitive electrochemical biosensor for the detection of carbaryl pesticide based on covalent immobilization of acetylcholinesterase (AChE) on multiwall carbon nanotubes/graphene oxide nanoribbons (MWCNTs/GONRs) nanostructure was reported by Liu and co-workers.³⁷ The MWCNTs/GONRs hybrid structure showed excellent properties including flexibility and electrical conductivity. They increased the catalytic activity of AChE as a result of the covalent binding technique.³⁷ Due to the covalent bonding no enzyme leakage was observed thus giving a stable enzyme electrode for the successful detection of carbaryl pesticide.³⁷

1.4 Graphene

There is no way of defining graphene without defining graphite first. The term graphite is derived from a Greek word “graphein” which means “to write”.³⁸ Graphite is a three-dimensional (3D) stacked layers of grapheme.³⁹ Graphene is a two-dimensional (2D) nanomaterial made up of carbon atoms arranged in a honeycomb lattice.^{40,41} Graphene has attracted a lot of attention due to its very unique properties like high surface area, mechanical strength, and conductivity.⁴² Fig 1.1a shows that graphene is the basic building block for all graphitic materials.^{39,43} It can be wrapped up into zero-dimensional (0D) fullerene (Fig 1.1b), rolled into one-dimensional (1D) nanotubes (Fig 1.1c), stacked into 3D graphite (Fig 1.1d) or fragmented into 0D quantum dots (Fig 1.1e)

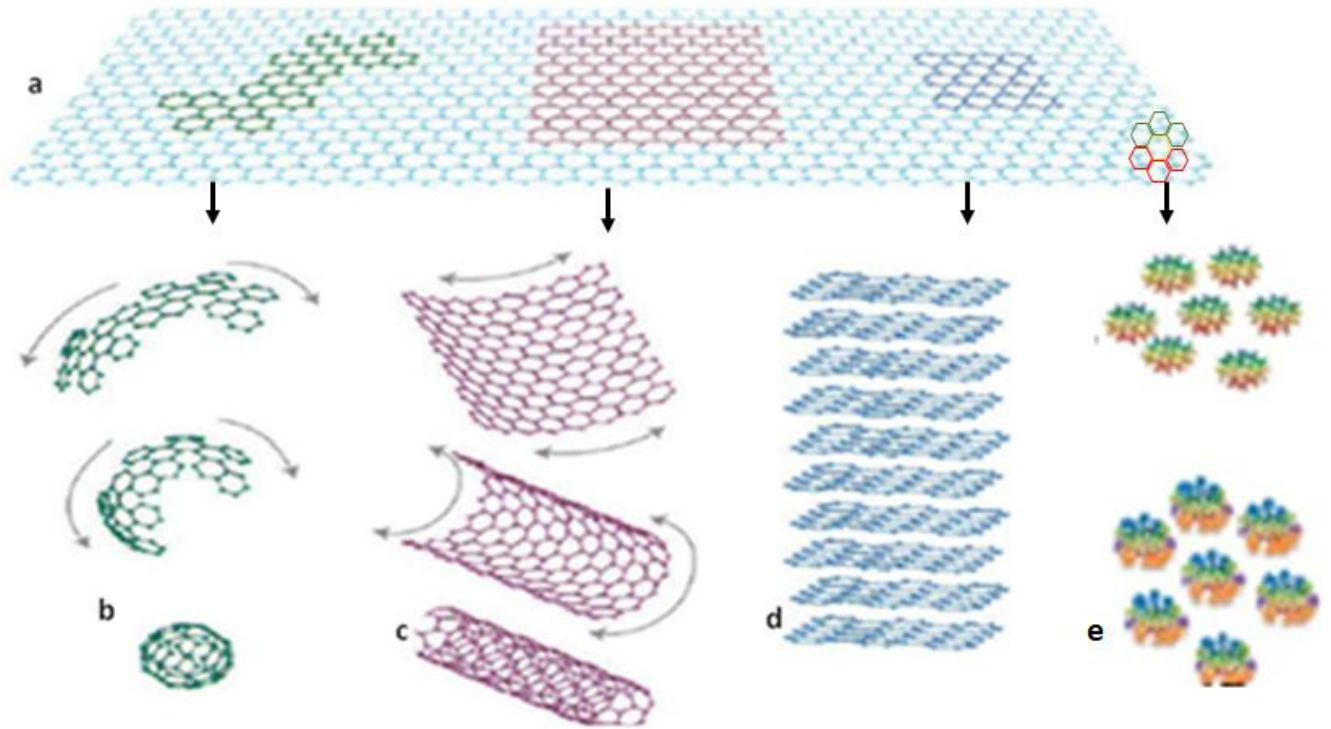


Fig 1.1: Schematic representation of graphene and its derivatives: (a) graphene 2D, (b) fullerene 0D, (c) nanotube 1D, (d) graphite 3D and (e) quantum dots 0D.³⁹

The use of graphene can be traced back to 1859⁴⁴ although it was only in 2004 when Professor Sir Andre Geim and Professor Sir Kostya Novoselov from the University of Manchester discovered and successfully isolated a single layer of graphite also known as grapheme.³⁹ The pair received a Nobel Prize in physics in 2010 as recognition of the ground-breaking work.⁴⁴ The isolation of the single layer flake from graphite was performed using a mechanical exfoliation procedure known as the scotch tape method.⁴⁵

Graphene has unique physicochemical properties, these include ease of functionalization, strong mechanical strength, and semiconductor applications.⁴³ Graphene is a highly elastic and crystalline material that retains its original size after strain.⁴⁶ Graphene is the strongest material ever discovered with a tensile strength higher than that of diamond.⁴⁷ Its crystallinity is believed

to determine the material's conductivity, an amorphous graphene results in high electron mobility leading to high conductivity.⁴⁸

1.4.1 Electronic properties of graphene

Carbon atoms have 6 electrons with 2 electrons in the inner shell and 4 electrons in the outer shell. In graphene, each sp^2 hybridized carbon atom is bonded to 3 other sp^2 hybridized carbon atoms on the 2D plane, leaving one electron freely available for electronic conduction.⁴⁹ The free electron binds covalently to neighbouring carbon atoms forming π -bonds and conducts electricity due to mobile π electrons delocalized above and below the graphene sheets.⁴¹ The electronic properties in graphene are determined by the bonding and anti-bonding of these pi orbitals.^{49,50} The conductivity of graphene is highly influenced by factors such as its crystallinity, chemical modification and the type of nanomaterials used to form graphene based composites. For instance graphene's conductivity can be increased by means of adding a conductive material such as copper.⁵¹ While the addition of nanomaterials such silicon dioxide would result in a decreased conductivity, due to their insulating nature.⁴⁹

1.4.2 Graphene oxide (GO) and reduced graphene oxide (rGO)

Graphene oxide is considered to be the disordered analogue of the highly conducting crystalline graphene.⁵² The chemical modification of graphene to graphene oxide is a promising route for improving physicochemical and optical properties of graphene. Despite the relative novelty of graphene as material of great interest, pristine graphene has a zero-band gap which limits its applications.⁵³ The oxidation of graphene to GO uses a modified Brodie or Hummers method, which now includes the exfoliation process for the formation of graphene from graphite.

The first example of oxidising graphite to graphite oxide came in 1859 by British chemist B. C Brodie. Fig 1.2 shows the structure of GO containing a range of reactive oxygen functional groups such as carbonyls and hydroxyls which makes it a potential candidate for use in many applications such as sensors¹⁵, electrodes¹⁶ and hydrogen storage.¹⁶ The oxygen containing functional groups create defects on the graphene lattice. It also makes covalent bonding with other atoms or molecules possible, aiding in opening of the graphene band gap.⁵³

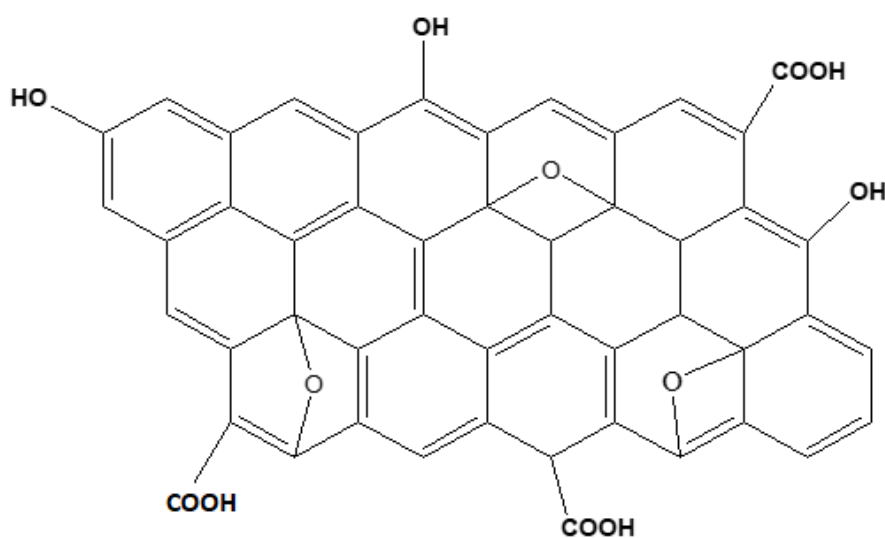


Fig 1.2: Structure of graphene oxide.

Graphene oxide synthesis method is an extension of the graphite oxide preparation. In 1859 Benjamin Brodie prepared the first sample of graphite oxide using strong oxidizing agents such as potassium chlorate (KClO_3) at high temperatures.⁵⁶ Brodie determined that the material obtained constituted of carbon, hydrogen, and oxygen, which led to an increase in the net mass of the flake graphite.⁵⁷ Successful oxidative reactions led to even higher oxygen content, reaching a limit after the fourth treatment.⁵⁸ Brodie also found that the material can be dispersed in pure or basic water, but not in acidic media, which resulted in the term “graphic acid”.⁵⁸ The drawback of this method was the production of chlorine dioxide (ClO_2) gas which often

led to explosions.⁵⁶ In order to rectify this L Staudenmaier developed an improved method which did not make use of heat.⁴³ This new and improved method for graphite oxidation added the chlorates in aliquots over the course of the reaction instead of the single addition done by Brodie.⁵⁸ This method also made use of sulphuric acid (H_2SO_4) with nitric acid (HNO_3) and chlorates, which resulted to a reduced reaction time.⁵⁹

In 1958 Hummers and Offeman prepared graphite oxide using potassium permanganate (KMnO_4) and concentrated sulphuric acid and it achieved a similar level of oxidation as the Staudenmaier method.⁶⁰ This method has been preferred and used although others have developed slightly modified versions for the oxidation of graphene. These three methods are the blueprint routes for forming GO.¹⁴ Importantly, it has since been shown that GO shows variance depending on the particular oxidants, the nature of parent graphite and the reaction conditions used.^{58,61}

Reduced graphene oxide is a product formed from decreasing the content of oxygen containing functional groups on graphene oxide through a reduction process. The reduction controls the degree of oxidation which allows for the tuning of physical properties.^{62,63} rGO is the intermediate between graphene and graphene oxide.⁶³ Reduced graphene oxide brings some of the crystallinity of graphene back, which was lost during the oxidation treatment to form graphene oxide.

There are various methods for the preparation of rGO including micro mechanical exfoliation, chemical vapour deposition and chemical reduction of GO which is regarded as a simple one-step process.⁶⁴ Several reducing agents, such as hydrazine (N_2H_4)⁶⁵, sodium borohydride (NaBH_4)⁶⁶ and hydriodic acid (HI)⁶³ are used. These methods use toxic substances, explosive gases and have many reaction steps.^{61,62} Therefore, methods that make use of greener and more

efficient reducing agents such as metal iodides (MgI_2 , AlI_3 , ZnI_2 , FeI_2) in ethanol solution are preferred.⁶⁷

1.4.3 Graphene quantum dots (GQDs)

GQDs are a fairly new type of nanomaterial with the first feature paper published in 2007.⁶⁸ Fig 1.3 shows the chemical structure of graphene quantum dots, these are fabricated via a redox reaction of graphene and ultrasonication using KMnO_4 as an oxidant.⁶⁹ GQDs have an electronic band gap that renders electrical and optical properties which are important in a number of applications including medicine.^{53,69} Their band gap is increased due to energy restriction caused by the small size of the nanomaterial.⁷⁰ They have a high surface area³⁰, high electron mobility⁷¹, physically and thermally stable⁷¹ making them ideal candidates as catalysts.⁶⁹

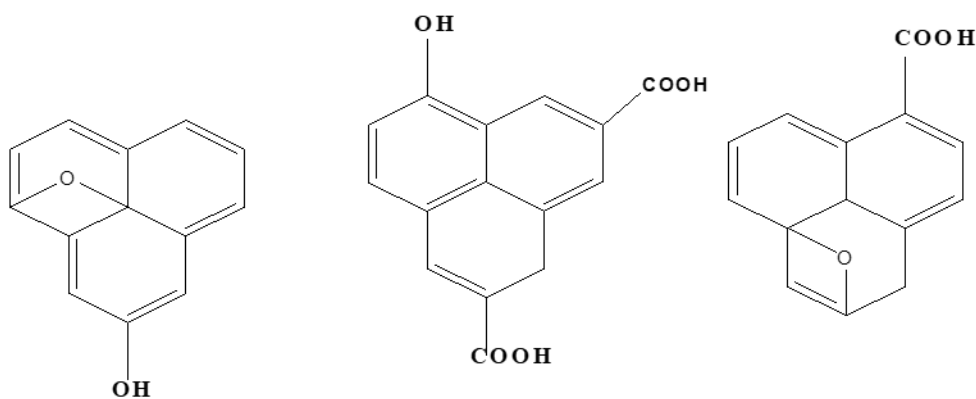


Fig 1.3: Structure of graphene quantum dots.

GQDs are synthesized using the top-down approach (TDA) or bottom-up approach (BUA). TDA refers to the cutting down of bulk to smaller materials and BUA is the building up of materials from the bottom.⁷² Converting the 2D graphene into zero-dimensional material, through oxidative treatment of GO is a top-down approach.²⁶ These approaches yield

heterogeneous samples with particles varying in size, shape and chemical composition, as a result displaying complex fluorescence behaviour.^{68,74} GQDs synthesized by bottom-up approach do not show the same degree of heterogeneity. They can also be prepared by exfoliation of the graphite nanoparticles and partial pyrolysis of organic material such as sugar or citric acid which is a form of BUA.⁷⁵

The fluorescence behaviour of GQDs is reported to be due to the actual size of the nanoparticles.⁷⁴ The most striking property of GQDs is the change in optical properties as a function of size. The change in electronic properties of semiconductor nanoparticles is inevitable as the size of the particles become smaller, the band gap gradually increases as a result of quantum confinement effects.⁷⁶ This effect occurs when quantum dots are smaller than their exciton Bohr radius.

1.5 Graphene based electrodes as pesticide sensors

There is great interest in the use of graphene based materials as sensors for the detection of analytes such as dopamine, hydrogen peroxide, nitric oxide and glucose.⁷⁷ Due to their high surface area, graphene based sensors have higher absorption capability, especially with respect to analytes with π -bonds. For instance, nitro-aromatic compounds such as organophosphates contain sp^2 hybridized carbon atoms that adhere well to graphene sheets.⁴² Graphene based electrodes exhibit better catalytic behaviour compared to the traditional glassy carbon electrode (GCE) and the noble metallic electrodes. This is due to the wider potential window and lower residual currents it possess.⁷⁷ However, GCE and metallic electrodes offer a variety of simple modification techniques and are often preferred candidates for chemically modified electrodes. The electro-catalytic activity of Gr based sensors can be improved by mixing them with other

nanomaterials, forming a nanocomposite. Graphene with a metal oxide (Gr-MO) or metal hydroxide (Gr-MOH) is an example of such nanocomposite.

1.5.1 Graphene based nanomaterials for pesticide sensors.

Table 1.2 shows various electrochemical sensors that have been developed for the detection of OPs. The limit of detection (LOD) values gives an indication of the sensitivity of the sensor.

Table 1.2: Developed graphene based electrochemical sensors for pesticide detection.

Sensor	Electrode	Analyte	LOD	Reference
Graphene oxide	GCE	thiamethoxam	8.3 $\mu\text{mol/L}$	78
		Imidacloprid	7.9 $\mu\text{mol/L}$	78
GO-chitosan nanohybrid	GCE	Methyl parathion	0.8 $\mu\text{g/mL}$	26
Prussian blue film-GQDs NPs	Carbon paste electrode (CPE)	Carbamate	1.0×10^{-7} mol/L	79
Cobalt porphyrin-graphene oxide NP	GCE	Methyl parathion	1.1×10^{-8} M	80
Pralidoxime-GQDs composite	GCE	Fenthion	6.8×10^{-12} M	29
Thermally reduced GO	GCE	Hydroquinone	0.75 μM	81
		Catechol	0.80 μM	81
AgNCs-rGO	GCE	DTC	16 ppb	82
CeO ₂ -GO	GCE	Fenitrothion	3.0 nM	83
rGO/GO		Chlorpyrifos	1200 mg g^{-1}	84
		Endosulfan	1100 mg g^{-1}	84
		Malathion	800 mg g^{-1}	84

Urbanová *et al* reported on the modification of GCE with graphene oxide for the electrochemical detection of insecticides thiamethoxam and imidacloprid.⁷⁸ Different amounts

of GO were used to test the sensors conductivity effectiveness. Increasing the GO content up to 4mg/mL in water gradually increased reduction peak current of thiamethoxam, whereas beyond this value a slight decrease in the peak current was observed.⁷⁸

This was a result of increasing thickness of the GO film that starts to build up on the electrode surface becoming unbeneficial for sensing. The selectivity of the electrodes was investigated by mixing several inorganic species, such as K^+ , Mg^{2+} , Ca^{2+} , NH_4^+ and Na^+ in a buffer solution. Compared to unmodified electrode, the GO modified GCE showed reduction peaks at less negative potentials proving fast electron transfer towards the analytes. The modified electrodes were also used for recovery test of spiked samples such as river water and honey, in order to determine their overall electrochemical performance.⁷⁸

Yang's *et al* reported on a preparation of Gr–chitosan (CS) composite deposited on GCE for MP detection.²⁶ The combination of Gr and CS showed great benefits such as strong adsorption ability and high electrical conductivity. The methyl parathion electrochemical behaviour was determined on CS/GCE and Gr-CS/GCE. The Gr-CS/GCE exhibited good adsorption ability due to CS, MP was strongly attached to CS film and the sensitivity towards MP was greatly enhanced as a result of excellent electrical conductivity and large surface area of Gr.²⁶ The sensor showed fast, simple, low detection limit and storage stability. Therefore, it was concluded that Gr-based composites are a promising sensing nanomaterial for Ops.²⁶

Oliveira *et al*⁷⁹ reported on an enzymatic biosensor developed through immobilization of trametes versicolor laccase (LACC) on graphene doped carbon paste electrode functionalized with prussian blue (PB) films (LACC/PB/GPE) for carbamate pesticides detection and food evaluation.⁷⁹ Trace concentrations of the carbamates were evaluated by inhibition of the reduction process of p-quinone to hydroquinone. Graphene doped carbon paste and LACC presence enhanced electrochemical and catalytic properties of the sensor. PB acted as an

artificial peroxidase, its combination with a natural enzyme, the device exhibited characteristics of a bi-enzymatic system, enhancing the biosensor performance.⁷⁹ The PB films enabled direct immobilization of LACC in acidic conditions, without the use of any crosslinking agent. The PB films were highly soluble in neutral and basic media. Therefore, polymeric films including nafion (NF), polypyrrol (PP), and CS were used to coat over the PB layers. The electrochemical behaviour of the 4-aminophenol (4-AMP) was determined on LACC/GPE and LACC/PB/GPE. Good catalytic effect was observed on the LACC/GPE although the intensity of the peak current obtained with LACC/PB/GPE was higher. LACC/PB/GPE also showed more stability compared to LACC/GPE.⁷⁹ The electroanalytical performance of the developed device in tomato and potato crops spiked with carbamates showed suitable sensitivity, reproducibility, selectivity, accuracy and stability.⁷⁹

A cobalt oxide-graphene oxide (Co_3O_4 -graphene oxide) composite based sensor immobilized on meso-tetra (4-carboxyphenyl) cobalt porphyrin (CoTCPP) was reported by Mei-Liu and co-workers for the electrochemical detection of methyl parathion.⁸⁰ The CoTCPP strongly adsorbed on graphene through π - π stacking and hydrophobic interactions and it was used to stabilize the Co_3O_4 -GO becoming CoTCPP- Co_3O_4 -GO.⁸⁰ It was also used to prevent graphene aggregation and introduce negatively charged groups such as -COOH on the graphene surface. The electrochemical analysis of MP behaviour on the cobalt based sensor showed increased peak currents with positive shifts of peak potentials on increased MP concentration.⁸⁰ A calibration of concentration showed a straight line and it gradually deviated from the straight line when the MP concentration was above 4.0×10^{-7} mol/L, suggesting that the saturated absorption was slowly being reached. The sensor exhibited unique electrochemical properties, and improved stability and catalytic activity as a result of the synergistic effects of GO, Co_3O_4 NPs, and CoTCPP for MP detection.⁸⁰

Dong *et al*²⁹ reported on the fabrication of an oxime-based sensor via attaching pralidoxime (PAM) on graphene quantum dots for the modification of GCE for fenthion detection in water and soil. The PAM was attached to graphene quantum dots via electrostatic attraction and π - π stacking interaction.²⁹ Dong and his group focused on the use of PAM as an electroactive probe, where the non-electroactive OPs sensing relied on the nucleophilic substitution reaction between oxime and OP. Fenthion was determined by measuring the change in oxidation current of PAM before and after reacting with the target analyte.²⁹ The introduction of GQDs significantly increased the electrode's surface area, which in turn enlarged the immobilization quantity of PAM, thus increasing PAM's oxidation current. The fabricated sensor exhibited high sensitivity, good reproducibility, and favourable presentation in real samples such as water and soil.²⁹

An application of an electrocatalyst, thermally reduced graphene oxide (TRGO) modified electrode in the simultaneous determination of dihydroxybenzene (DHB) isomers including hydroquinone (HQ), catechol (CC) and resorcinol (RC) was reported by Li and co-workers.⁸¹ Redox peaks of isomers such as HQ and CC usually overlap due to their electroactive groups, making it hard to detect them with conventional electrodes. Conventional electrodes also show limited selectivity, sensitivity and low electron transfer rate. Therefore, TRGO was used to modify GCE to overcome these inherent difficulties.⁸¹ The enhanced electron transfer rate was demonstrated by the positive and negative potential shift of the cathodic and anodic peak respectively. Two oxidation peaks on a GCE were observed, one due to an overlap of HC and CC and the other to RC. While on the TRGO/ GCE three well-defined redox peaks were observed at different potentials proving that the sensor is selective and can be used to simultaneously determine the three isomers in environmental analysis and bio-electrochemistry.⁸¹

Zhu *et al*⁸² reported on the detection of dithiocarbamate (DTC) pesticides with a sponge-like surface-enhanced raman scattering (SERS) substrate constructed from reduced graphene oxide-wrapped silver nanotubes. SERS provided the characteristic spectrum of pesticides and prevented the use of a molecular recognition probe in the sensor.⁸² High sensitivity, good anti-interference ability and robustness of the sensor was achieved with the incorporation of silver nanotube-reduced graphene oxide (AgNC-rGO) in the sponge. In the AgNC-rGO sponge, the rGO sheets formed a porous scaffold that physically held the AgNCs creating a narrow gap between the surrounding AgNCs which aided in the formation of enhanced detection signal of SERS.⁸² AgNC-rGO sponge exhibited a flat surface and high-density of AgNCs, ensuring good SERS signal uniformity, substrate-to-substrate reproducibility and high SERS activity. When DTC was mixed with thiophanate-methyl, carbendazim and isazofos the sponge selectively detected it, due to its preferential adsorption of DTC pesticides on the Ag surface and aromatic pesticides on the rGO surface. This effectively eliminated the interference of the SERS signals of aromatic pesticides, and enabled the qualitative and quantitative analysis of DTC pesticides.⁸²

Ensafi *et al*⁸³ reported on the preparation of cerium oxide and reduced graphene oxide nanocomposite (CeO₂/rGO) as an efficient mediator for electrochemical detection of fenitrothion (FT). FT is an insecticide which often leads to stomach poisoning on exposure. The CeO₂ nanoparticles increased the surface of the nanocomposite by enlarging the surface roughness while the rGO increased the sensors conductivity. The electrochemical behaviour of FT was evaluated on GCE, rGO/GCE, and CeO₂-rGO/GCE. The CeO₂-rGO/GCE shifted the oxidation and reduction peaks of FT to lower potentials and increased redox peak currents, compared to the rGO-GCE and unmodified GCE.⁸³ These results confirmed the synergetic effect of CeO₂/rGO on the oxidation of FT. The sensor proved to be selective towards FT, even when FT was mixed with common interference species contained in water samples including

NO_3^- , Cl^- , Ca^{2+} and SO_4^{2-} . The results showed that the interference species represented no significant effects on current signals of FT.⁸³

A graphene reusable substrate for the adsorption of pesticides such as chlorpyrifos (CP), endosulfan (ES), and Malathion (ML) was reported by Shihabudheen's group.⁸⁴ An analysis using first-principles pseudopotential-based density functional theory (DFT) was carried out to define the removal mechanism and understand the adsorbent capability. GO and rGO were used as adsorbents and the uptake capabilities for CP, ES and ML were found to increase with decreasing GO/rGO content.⁸⁴ This was a result of increased mass transfer at higher adsorbate to adsorbent ratio. rGO showed better adsorbing ability compared to GO due to increased surface area. The CP, ES and ML uptake capability of rGO was found to be approximately 10–20% higher than that of GO.⁸⁴

1.6 Metal based nanomaterials as pesticide sensors.

Metals are capable of forming compounds with oxygen to produce metal oxides (MO) that are of great technological importance.⁸⁵ MO's can adopt a vast number of structural geometries with an electronic structure that show different characters such as metallic, semiconductor or insulator.⁸⁵ Metal oxides at the nanoscale exhibit better physical and chemical properties compared to their bulk state as a result of high surface area ratio. The fundamental sensing mechanism of metal oxide based sensors relies upon the change in electrical conductivity due to the interaction between the analyte and oxygen on the surface of the nanomaterial.⁸⁶

When mixed with graphene, metal oxides prevent the re-stacking of graphene and in turn graphene suppresses the agglomeration of metal oxides keeping them in a dispersed form.⁸⁷ The oxygen on graphene ensures good bonding, interfacial interactions and electrical contacts between Gr and MO.⁸⁸ It also allows interaction with a wide variety of molecules such as the

absorption of heavy metals and interacts with cationic dyes.⁸⁸ Recently, a number of studies have been published on various applications of graphene/metal oxide nanocomposites such as photo-catalysts and environmental monitoring.⁸⁸ These nanocomposites exhibit exceptional properties such as higher adsorptivity, conductivity, tuneable optical behaviour, stability and longevity.⁸⁸ This work focuses on four metal oxides NiO, MnO₂, Cu₂O and Al₂O₃ and their corresponding hydroxides Ni(OH)₂, Mn(OH)₂, Cu(OH)₂ and Al(OH)₃. These were chosen due to factors like their green nature, abundance and cost-effectiveness.

1.6.1 Nickel oxide (NiO) and nickel hydroxide (Ni(OH)₂) nanoparticles as sensor materials

Nickel nanoparticles have find potential in various fields including electronics, sensors and biomedicines.⁸⁹ Nickel is eco-friendly and is a p-type semiconductor with a bandgap of approximately 3.6 to 4.0 eV.⁸⁹ Nickel oxide is studied widely due to its electro-catalytic properties, high chemical and physical stability and super conductance characteristics.⁸⁹ Table 1.3 shows the nickel oxide and/or hydroxide nanoparticles previously used for pesticide detection. Yang *et al*⁹⁰ reported on the construction of an acetylcholinesterase (AChE) biosensor based on NiO NPs, carboxylic graphene (CG) and NF on a glassy carbon electrode. Biosensors based on AChE are a promising technique for environmental monitoring and food quality control.⁹⁰ AChE based NMs are mainly used for the detection of organophosphate and carbamate pesticides based on enzyme inhibition.⁹⁰ NiO NPs-CGR-NF nanocomposites showed excellent conductivity and catalysis and contained a hydrophilic surface which is perfect for AChE adhesion. CS was used to immobilize the AChE on NiO-NPs/CGR-NF/GCE and enhance the electron transfer.⁹⁰ NF was applied as the protective membrane for the AChE biosensor, therefore improving the stability of the biosensor.⁹⁰

The NiO/NPs and a catechol derivative (2,4-dimethyl-N'-[1-(2,3-dihydroxyphenyl) methylidene] aniline) were used to modify a carbon paste electrode for the simultaneous detection of water pollutants, such as thiosulfate (TS), 4-chlorophenol (4-CP) and nitrite (NT).⁹¹ Keivani and co-workers reported that the NiO NPs were used due to their high conductivity and the catechol derivative was used as a mediator for electro-catalytic interaction with the analytes. The sensor showed high sensitivity and selectivity towards the simultaneous detection of the three analytes in water.⁹¹

Table 1.3: Developed nickel oxide/hydroxide electrochemical sensors for pesticide detection.

Sensor	Electrode	Analyte	LOD	Reference
NiONPs/CG/NF	GCE	methyl parathion	5×10^{-14} M	90
		carboturan	5×10^{-13} M	90
NiO-CC	GCE	Thiosulfate	μ M	91
		4 – chlorophenol	0.70 μ M	91
		nitrite	5 μ M	91
BPF/NiO/CNTs	CPE	hydroxylamine	0.2 μ M	92
PHPID/NiO	CPE	methyldopa	μ M	93
nanoPt-LDHs	SPE	Methyl parathion	0.6 ng mL ⁻¹	94

Similar to Keivani's work, Golestanifar and co-workers reported on the fabrication of a 1,1-bis(phenylacetyl)ferrocene/NiO/CNTs for the modification of the carbon paste electrode (1,1-BPF/NiO/CNTs/CPE) for the detection of the pollutant, hydroxylamine (HX) in water samples.⁹² The 1, 1 BPF was used as the mediator for electrocatalytic interaction of the sensor with analyte. The NiO was used for its high conductivity while the CNTs increased the surface area of the sensing material.⁹² Keyvanfard and co-workers reported on the modification of CPE with NiO nanoparticle (NiO NPs) and 2-(3,4-dihydroxyphenethyl)isoindoline-1,3-dione

(DHPID) (CPE/DHPID/NiO-NPs), for the determination of methyldopa in the presence of tyrosine in drug samples.⁹³ Methyldopa is one of the most important and usable drug for treatment of high blood pressure.⁹³ The electrochemical behaviour of methyldopa was investigated on the surface of CPE/DHPID and CPE/DHPID/NiO-NPs. The CPE/DHPID showed weak peak current compared to CPE/DHPID/NiO-NPs indicating that the NiO NPs improved the electrical conductivity of carbon paste electrode.⁹³

Gong *et al*⁹⁴ reported on a nanoPt intercalated Ni/Al layered double hydroxide (nanoPt-LDHS) based on the solid phase extraction (SPE) of methyl parathion. The NanoPt-LDHs absorbed MP and showed high efficiency of capturing OPs. The electrochemical sensing of MP occurred through electro-synthesis of Ni/Al-LDHs film onto a glassy carbon electrode surface with subsequent exchange of PtCl_6^{2-} , followed by electrochemical reduction to form the assembly of NanoPt and Ni/Al-LDHs onto GCE (NanoPt-LDHs/GCE).⁹⁴ MP was intercalated into the interlayer space of NanoPt-LDHs/GCE and finally the electrochemical stripping detection of the absorbed MP.⁹⁴ To our knowledge there has not been reports on the use of $\text{Ni}(\text{OH})_2$ as a sensor material for pesticide detection.

1.6.2 Copper oxide (Cu_2O) and copper hydroxide ($\text{Cu}(\text{OH})_2$) nanoparticles as sensor material

Copper based nanoparticles, such as Cu_2O have attracted attention in catalysis because of their low cost, abundance and non-toxicity.⁹⁵ Copper is a p-type semiconductor metal with a narrow bandgap of 1.2 eV.^{96,97} Table 1.4 shows the copper oxide and/or hydroxide nanoparticles previously used for pesticide detection. Veeramani and co-workers reported on a development of Cu_2O micro-structured nanoparticles used for GCE modification for the electrochemical detection of 4-nitrophenol (4-NP). Various Cu_2O morphologies including cubes, sheets and

flowers were synthesized for the selective and sensitive electrochemical detection of 4-NP. Amongst the three morphologies, the Cu₂O sheets on GCE showed better selectivity and lower over potential. It also showed maximum background current, resulting in high catalytic activity and conductivity.⁹⁸ An electrochemical sensor based on coupled CuO/Cu₂O nanoparticles and multi-walled carbon nanotubes nanocomposite (CuO/Cu₂O/MWCNTs/GCE) film for L-tyrosine detection was reported by Gu and co-workers.⁹⁹ CuO/Cu₂O nanoparticles have a large specific surface area and high surface reaction activity, combined with MWCNTs high-conductivity and high-catalytic-activity was observed, which aided in improving the stability and sensitivity of CuO/Cu₂O/MWCNTs/GCE sensor.⁹⁹

Table 1.4: Developed copper oxide/hydroxide electrochemical sensors for pesticide detection.

Sensor	Electrode	Analyte	LOD	Reference
Cu ₂ O	GCE	4 - nitrophenol	0.5 μM	98
CuO/Cu ₂ O/MWCNTs	GCE	L-tyrosine	9.6 x 10 ⁻⁹ M	99
Cu ₂ O-rGO	GCE	Bisphenol A	5.0 x 10 ⁻³ M	100
MWCNTs/Cu(OH) ₂ /IL	GCE	diclofenac	0.04 μM	101

Shi et al¹⁰⁰ reported on an electrochemical sensor based on reduced graphene oxide/copper oxide (rGO/Cu₂O) nanocomposite for the modification of glassy carbon electrode, for the detection of BPA. The rGO/GCE showed increased redox peak currents due the excellent conductivity and large specific surface area of rGO. The redox peak currents of Cu₂O-rGO/GCE increased as a result of good synergistic effect of Cu₂O NPs and graphene including the large surface area of rGO and high conductivity of Cu₂O.¹⁰⁰ The Cu₂O-rGO/GCE large surface area enhanced electron transfer rate between BPA and the electrode surface¹⁰⁰.

An electrochemical sensor based on Cu(OH)₂ NPs, hydrophobic ionic liquid 1-ethyl-3-methylimidazolium hexafluorophosphate (EMIMPF₆) and multiwalled carbon nanotubes

(Cu(OH)₂-EMIMPF₆-MWCNTs) nanocomposite modified GCE was reported by Arvand and co-workers.¹⁰¹ The Cu(OH)₂-EMIMPF₆-MWCNTs/GCE sensor was used for the detection of the anti-inflammatory drug diclofenac. It exhibited increased anodic peak current compared to the Cu(OH)₂-MWCNTs/GCE sensor. The results indicated that the combination of MWCNTs, Cu(OH)₂ nanoparticles and EMIMPF₆ enhanced the electrochemical response towards the analyte.¹⁰¹ This is a result of the nanocomposite's high surface area and high conductivity. The EMIMPF₆ interacted with the CNTs through π - π and/or electrostatic interaction, leading to high stability of the sensor.¹⁰¹ There are limited reports on the use of Cu(OH)₂ as sensing material for pesticide detection.

1.6.3 Manganese oxide (MnO₂) and manganese hydroxide (Mn(OH)₂) nanoparticles as a sensor material.

Manganese nanoparticles have been applied in wastewater treatment, catalysis, sensors, supercapacitors, and alkaline rechargeable batteries.¹⁰² In the past decade MnO₂, an oxidant and catalytic agent, has been utilized in many fields, such as in the realm of energy and sensing.¹⁰³ Many experiments indicate that manganese dioxide is an n-type semiconductor^{103,104}, with its conduction mechanism not well defined and a bandgap of 1.3 eV.¹⁶ Table 1.5 shows the manganese oxide and/or hydroxide nanoparticles previously used for pesticide detection. Yan *et al*¹⁰⁶ reported a fluorescence “turn off-on” based graphene quantum dots/manganese dioxide composite nanosensor for the selective detection of Glutathione (GSH) in living cells. The GQDs were used for their fluorescence properties but MnO₂ quenched their fluorescence.¹⁰⁶ The MnO₂ was reduced to Mn²⁺ cations by the GSH, increasing the fluorescence. Therefore, the MnO₂ NPs served as both fluorescence nanoquencher and GSH recognizer on the sensor. The sensing nanomaterial showed a sensitive

response to GSH due to the increased fluorescence. The sensor is potentially ideal for use in disease diagnostics.¹⁰⁶

Zaidi *et al*¹⁰⁷ reported on the fabrication of a sensor via electrodeposition of manganese dioxide nanoparticles (MnO₂-NPs) over reduced graphene oxide (rGO) on a GCE for the determination of 4-NP.¹⁰⁷ The rGO/GCE was immersed in freshly prepared aqueous solution containing 10 mM KMnO₄ and 50 mM H₂SO₄ to obtain MnO₂/rGO/GCE. Superior electric conductivity of rGO resulted in enhanced redox peaks for rGO/GCE compared to MnO₂/GCE.

Table 1.5: Developed manganese oxide/hydroxide electrochemical sensors for pesticide detection.

Sensor	Electrode	Analyte	LOD	Reference
GQDs/MnO ₂	GCE	glutathione	150 nM	106
rGO/MnO ₂	GCE	glutathione	10 nM	107
MnO ₂ /GO	SPE	nitrite	0.09 μM	108
MnO ₂	assay	polydopamine	1.5 μM	109

The MnO₂-rGO/GCE sensor exhibited increased redox peak currents showing the synergic effects from MnO₂ NPs and rGO.¹⁰⁷ It also showed a reduced peak separation due to better electrochemical reversibility, high electro-catalytic activity, high conductivity, large surface area compared to bare rGO/GCE and MnO₂/GCE.¹⁰⁷

Jaiswal and his groups reported on a screen-printed amperometric sensor based on carbon ink bulk-modified with MnO₂ decorated graphene oxide (MnO₂/GO) nanocomposite with use of chitosan as depositing matrix for the determination of nitrite (NO₂⁻).¹⁰⁸ The electrochemical behaviour of NO₂⁻ was investigated on a MnO₂/CS/GO/GCE and MnO₂/GO/SPE. A decrease in over-potential and an increase in the oxidation peak current was observed on the GCE based sensor.¹⁰⁸ While the SPE based sensor exhibited a further decrease in over-potential which

indicated that the modified SPE facilitates electron transfer and NO_2^- oxidation faster compared to modified GCE. It was concluded that the $\text{MnO}_2/\text{GO-SPE}$ showed oxidation at lower overpotential, high sensitivity and reproducibility.¹⁰⁸

MnO_2 was used as an oxidant in the synthesis of polydopamine (PDA) nanoparticles by Kong and co-workers. Dopamine was oxidised to its quinone derivative by MnO_2 and auto-polymerised into fluorescent PDA nanoparticles used as a signal indicator in GSH detection.¹⁰⁹ However, MnO_2 was reduced into Mn^{2+} by GSH, which would inhibit the formation of the fluorescent PDA nanoparticles. Thus, using the fluorescent PDA nanoparticles as a fluorescence signal indicator, the concentration of GSH was detected according to the decreased signal intensity of the fluorescent PDA nanoparticles.¹⁰⁹ The sensor exhibited good sensing performance towards GSH and this strategy showed desirable selectivity for GSH with potential interfering species. The sensor showed, excellent practical applications for GSH detection in human whole blood samples.¹⁰⁹ To our knowledge there has been no reports on the use of $\text{Mn}(\text{OH})_2$ as a sensor material for pesticide detection.

1.6.4 Aluminium oxide (Al_2O_3) and aluminium hydroxide ($\text{Al}(\text{OH})_3$) nanoparticles as a sensor material.

Aluminium nanoparticles are of interest to various fields including pyrotechnic, propellant, and explosive industries.¹¹⁰ Aluminium NPs are effective catalysts due to their high surface area and they possess a bandgap of 3.18 to 3.25 eV.¹¹¹ Table 1.6 shows the aluminium oxide and/or hydroxide nanoparticles previously used for pesticide detection. Wei and co-workers reported on the construction of a substrate utilizing polishing-activated nano $\alpha\text{-Al}_2\text{O}_3$ sorbent for the detection of organophosphate pesticides.¹¹² The polished $\alpha\text{-Al}_2\text{O}_3$ modified GCE for MP detection exhibited a current peak increase with no saturation response up to the concentration

of 2000 ng mL⁻¹. To test the sensor's selectivity, equal amounts of nitro or phenol containing analytes including 2, 4 dinitrotoluene, nitrobenzene, 4NP and hydroquinone were added to the MP solution and no electrochemical redox was observed with these analytes.¹¹² This suggested that the phosphate ion (PO₄³⁻) did not interfere with the adsorption of MP, this is as a result of the adsorption ability of polished α - Al₂O₃ to MP which is much stronger than that of phosphate ion.¹¹² This substrate exhibited high selectivity and the polished α -Al₂O₃ nanoparticle was found to have strong affinity towards the phosphoric group in organophosphate pesticides.¹¹²

Table 1.6: Developed aluminium oxide/hydroxide electrochemical sensors for pesticide detection.

Sensor	Electrode	Analyte	LOD	Reference
α – Al ₂ O ₃	GCE	ethyl parathion	0.035 ng mL ⁻¹	112
		Fenitrothion	0.035 ng mL ⁻¹	112
Ta ₂ O ₅ /Al ₂ O ₃ /Si ₃ N ₄	EIS	paraoxon	-	113
1.0Pt/ICeO ₂ /mp-Al ₂ O ₃	GCE	Volatile organic compounds	-	114

A capacitive field-effect sensor for the direct detection of organophosphorus pesticides (paraoxon) using the enzyme organophosphorus hydrolase (OPH) was reported by Chen's group.¹¹³ Ta₂O₅, Al₂O₃ and Si₃N₄ were used to form the transducer structure of the sensor. The Ta₂O₅ and Al₂O₃ layers were grown via pulsed laser deposition (PLD), while Si₃N₄ was deposited by low pressure chemical vapour deposition (LPCVD) onto a basic structure of Al/p-Si/SiO₂. The analytical method of the fabricated sensor was based on the enzyme OPH catalytic hydrolyses of organophosphorus compounds, thus releasing H⁺ ions. The hydrogen ion concentration increased with increasing amount of the pesticide parathion.¹¹³ A weakly buffered test sample was used to monitor the change in pH, detected by the underlying pH-sensitive material (Si₃N₄) of the electrolyte insulator silicon (EIS) biosensor. The paraoxon

concentration was increased and that resulted in the increase of the H^+ ions from the catalytic reaction. Other OPs can also be hydrolysed by OPH to yield H^+ ions. Therefore, the developed biosensor showed great potential for high catalytic OP sensing.¹¹³

Hyodo *et al*¹¹⁴ reported on volatile organic compounds (VOC, ethanol, toluene and o-xylene) sensing via adsorption/combustion-type gas sensors developed by using the micromechanical systems (MEMS) technology and an oxide-film fabrication technique by drop coating using an air-pulse fluid dispenser.¹¹⁴ The sensor was constructed through loading mesoporous (mp) Al_2O_3 powders with noble metal nanoparticles such as pure Pt, Au/Pt and Pt/Pd via sonochemical reduction technique. The noble NPs aided in enhancing catalytic combustion properties of the VOCs and/or the thermal conductivity of the sensing materials.¹¹⁴ The combination of minimal amounts of Pt with Au was also effective in improving some reactions such as selective oxidation of carbon monoxide (CO). The co-loading of metal oxides including CeO_2 , NiO, CuO, Fe_2O_3 and Mn_2O_3 to mp- Al_2O_3 was investigated on the adsorption/combustion-type sensors. CeO_2 showed large absorption and desorption properties of oxygen attributed to the active Ce^{3+}/Ce^{4+} redox pair compared to other metal oxides, and hence the addition of CeO_2 to various catalysts effectively improved the combustion behaviour towards VOCs.¹¹⁴ To our knowledge there has been no reports on the use of $Al(OH)_3$ as sensing material for the detection of pesticide.

1.7 Aims and objectives of this work

1.7.1 Aims

- To fabricate a sensor based on graphene quantum dots for the detection of methyl parathion.

- To use metal oxide and their corresponding metal hydroxide NPs together with the graphene quantum dots to enhance the electrochemical performance towards the detection of MP.

1.7.2 Objectives

- Synthesis of graphene oxide and graphene quantum dots.
- Synthesis of the following metal oxides NiO, Cu₂O, MnO₂, Al₂O₃ and metal hydroxides Ni(OH)₂, Cu(OH)₂, Mn(OH)₂, Al(OH)₃ NPs.
- Characterisation of nanomaterials using TEM, SEM, XRD, Raman spectroscopy, thermal gravimetric analysis, photoluminescence, ultraviolet visible spectroscopy and Fourier transform Infrared spectroscopy.
- The following electrodes will be prepared:
 - Graphene paste electrode (GPE)
 - GPE modified with metal oxide or metal hydroxide NPs.
 - The glassy carbon electrode modified with metal oxide/graphene quantum dots or metal hydroxide/graphene quantum dots composite.
- To conduct electrochemical studies to determine the efficiency of the modified electrodes towards methyl parathion detection.

1.7 References

- (1) Sartor, J. D.; Boyd, G. B.; Agardy, F. J. *Source J. Water Pollut. Control Fed. Part I* **1974**, *46* (3), 458–467.
- (2) World, C. *Leg. Rep.* **2011**, *6*, 58–73.
- (3) Heath, A. *Water Pollution and Fish Physiology*, 2nd ed.; CRC Press, **1995**.
- (4) Pajares, G.; Peruzzi, A.; Gonzalez-de-Santos, P. *Sensors*. **2013**, *13* (9), 12132–12139.
- (5) Tripathi, A. K.; Pandey, S. N. *Water pollution*; APH Publishing, **1990**.
- (6) Angelakis, A. N. Andreas N. *Evolution of water supply throughout the millennia*; IWA Publishing, **2012**.
- (7) Juuti, P.; Katko, T. S.; Vuorinen, H. S. *Environmental history of water : global views on community water supply and sanitation*; IWA Publishing, **2007**.
- (8) Carson, R. *Silent Spring*; Houghton Mifflin Harcourt, **1962**.
- (9) Edwards, F. L.; Tchounwou, P. B. *Int. J. Environ. Res. Public Health* **2005**, *2* (3), 430–441.
- (10) Kamel, F.; Hoppin, J. A. *Environ. Health Perspect.* **2004**, *112* (9), 950–958.
- (11) Bruce Ames, by N.; Krovoza, J. *Proc. Natl. Acad. Sci* **1992**, *1*, 79–85.
- (12) Özkara, A.; Akyıl, D.; Konuk, M. *Intech-open Sci.* **2016**, 1–27.
- (13) Groenewald, Y. Toxic DDT a huge health risk, Mail & Guardian, **2010**.
- (14) Fishel, F. M. *IFAS extension-UF* **2016**, No. 1, 2–6.
- (15) White, R. F.; Steele, L.; O’Callaghan, J. P.; Sullivan, K.; Binns, J. H.; Golomb, B. A.;

- Bloom, F. E.; Bunker, J. A.; Crawford, F.; Graves, J. C.; Hardie, A.; Klimas, N.; Knox, M.; Meggs, W. J.; Melling, J.; Philbert, M. A.; Grashow, R. *Cortex*. Elsevier January 1, **2016**, 449–475.
- (16) Asai, Y.; Arnold, J. L. *Prehosp. Disaster Med.* **2003**, *18* (2), 106–114.
- (17) Agents Classified by the IARC Monographs. *IARC Monogr.* **2012**, *7* (50), 1–25.
- (18) Holt, H. A. *Model Certification Training Manual for Right-of-Way Pesticide Applicators*, **2002**; 1–12.
- (19) American Cancer Society. *Cancer Organisation: known and probable human carcinigen.* **2013**.
- (20) Halliker, P. E. Environmental Fate, Evaluation of Methyl Parathion as a Toxic Air Contaminant, **1999**.
- (21) Chouhan, R. S.; Vinayaka, A. C.; Thakur, M. S. *Anal. Methods* **2010**, *2* (7), 924.
- (22) Weston, S. *Environ. Manage.* **2011**, 1–9.
- (23) Mancy, K. H.; Allen, H. . *Handb. water water Pollut.* **1972**, *3*, 971–1020.
- (24) National Research Council. *Identifying Future Drinking Water Contaminants*; **1999**.
- (25) Govindasamy, M.; Mani, V.; Chen, S. M.; Chen, T. W.; Sundramoorthy, A. K. *Sci. Rep.* **2017**, *7*, 46471.
- (26) Yang, S.; Luo, S.; Liu, C.; Wei, W. *Colloids Surfaces B: Biointerfaces* **2012**, *96*, 75–79.
- (27) Power, A. C.; Morrin, A. *Intech-open Sci.* **2013**, 141–165.
- (28) Fraceto, L. F.; Grillo, R.; de Medeiros, G. A.; Scognamiglio, V.; Rea, G.; Bartolucci,

- C. *Front. Environ. Sci.* **2016**, *4*, 1–5.
- (29) Dong, J.; Hou, J.; Jiang, J.; Ai, S. *Anal. Chim. Acta* **2015**, *885*, 92–97.
- (30) Fan, Z.; Li, S.; Yuan, F.; Fan, L. *RSC Adv.* **2015**, *5* (25), 19773–19789.
- (31) Artiles, M. S.; Rout, C. S.; Fisher, T.; Rout, C. S.; Fisher, T. S. *Adv. Drug Deliv. Rev.* **2011**, *63*, 1352–1360.
- (32) Zhu, C.; Yang, G.; Li, H.; Du, D.; Lin, Y. *Am. Chem. Soc.* **2014**, *1* (87), 230–249.
- (33) Piriya Wong, V.; Thongpool, V.; Asanithi, P.; Limsuwan, P. *J. Nanomater.* **2012**, *2012*.
- (34) Khot, L. R.; Sankaran, S.; Maja, J. M.; Ehsani, R.; Schuster, E. W. *Crop Protection.*, **2012**, 64–70.
- (35) Lü, M.; Li, J.; Yang, X.; Zhang, C.; Yang, J.; Hu, H.; Wang, X. *Chinese Sci. Bull.* **2013**, *58* (22), 2698–2710.
- (36) Yang, K.; Chen, B.; Zhu, L. *Sci. Rep.* **2015**, *5*, 11641.
- (37) Liu, Q.; Fei, A.; Huan, J.; Mao, H.; Wang, K. *J. Electroanal. Chem.* **2015**, *740*, 8–13.
- (38) Fuchs, J. N.; Goerbig, M. O. *Introd. to Carbon Mater.* **2008**.
- (39) Geim, A. K.; Novoselov, K. S. *Nat. Mater.* **2007**, *6* (3), 183–191.
- (40) Li, X.; Wang, X.; Zhang, L.; Lee, S.; Dai, H. *Science (80)*. **2008**, *319* (5867), 1229–1232.
- (41) Castro Neto, A. H.; Guinea, F.; Peres, N. M. R.; Novoselov, K. S.; Geim, A. K. *Rev. Mod. Phys.* **2009**, *81* (1), 109–162.
- (42) Piyush Sindhu Sharma, Francis D'Souza, and Wlodzimierz K. *Top Curr Chem* **2013**, *11* (1), 13–35.

- (43) Rao, C.; Sood, A. *Graphene: synthesis, properties, and phenomena*, 1st Ed.; WILEY-VCH Verlag, **2013**.
- (44) Dreyer, D. R.; Ruoff, R. S.; Bielawski, C. W. *Angew. Chemie - Int. Ed.* **2010**, *49* (49), 9336–9344.
- (45) Sobon, G.; Sotor, J.; Jagiello, J.; Kozinski, R.; Zdrojek, M.; Holdynski, M.; Paletko, P.; Boguslawski, J.; Lipinska, L.; Abramski, K. M. *Opt. Express* **2012**, *20* (17), 19463.
- (46) Tsai, J. L.; Tu, J. F. *Mater. Des.* **2010**, *31* (1), 194–199.
- (47) Pumera, M. *Mater. Today* **2011**, *14* (7), 308–315.
- (48) Khan, M. S.; Shakoor, A. *J. Chem.* **2015**, *1*, 1–6.
- (49) Castro Neto, A. H.; Guinea, F.; Peres, N. M. R.; Novoselov, K. S.; Geim, A. K. *Rev. Mod. Phys.* **2009**, *81* (1), 109–162.
- (50) Gao, W.; Alemany, L. B.; Ci, L.; Ajayan, P. M. *Nat. Chem.* **2009**, *1* (5), 403–408.
- (51) Qian, Y.; Ye, F.; Xu, J.; Le, Z. G. *Int. J. Electrochem. Sci.* **2012**, *7* (10), 10063–10073.
- (52) Bhuyan, M. S. A.; Uddin, M. N.; Islam, M. M.; Bipasha, F. A.; Hossain, S. S. *Int. Nano Lett.* **2016**, *6* (2), 65–83.
- (53) Duan, Y.; Stinespring, C. D.; Chorpening, B. *Chemistry Open* **2015**, *4* (5), 642–650.
- (54) Sakhaee-Pour, A.; Ahmadian, M. T.; Vafai, A. *Solid State Commun.* **2008**, *145* (4), 168–172.
- (55) Dimitrakakis, G. K.; Tylianakis, E.; Froudakis, G. E. *Nano Lett.* **2008**, *8* (10), 3166–3170.
- (56) Yiqing S, Shiqi W, Li C, Luo P, Tao L, Wei Y and Shi G., *Phys. Chem. Chem. Phys.*

- 2013**, *15* (24), 9907.
- (57) Brodie, B. C. *Philos. Trans. R. Scociety London* **1859**, *149* (1859), 249–259.
- (58) Gao, W. *Graphene Oxide Reduct. Recipes, Spectrosc. Appl.* **2015**, 61–95.
- (59) Lee, D. W.; De Los Santos V., L.; Seo, J. W.; Felix, L. L.; Bustamante D., A.; Cole, J. M.; Barnes, C. H. W. *J. Phys. Chem. B* **2010**, *114* (17), 5723–5728.
- (60) Hummers, W. S.; Offeman, R. E. *J. Am. Chem. Soc.* **1958**, *80* (6), 1339–1339.
- (61) Loryuenyong, V.; Totepvimarn, K.; Eimburanapratvat, P.; Boonchompoo, W.; Buasri, A.; *Adv. Mater. Sci. Eng.* **2013**, *2013*, 1–5.
- (62) Tkachev, S. V.; Yu, E.; Buslaeva, A. V.; Naumkin, S. L.; Kotova, I. V.; Laure, S. P.; Gubin. *Inorg. Mater.* **2012**, *48* (8), 796–802.
- (63) Chen, C.; Long, M.; Xia, M.; Zhang, C.; Cai, W. *Nanoscale Res. Lett.* **2012**, *7* (1), 101.
- (64) Lavin-Lopez, M. P.; Paton-Carrero, A.; Sanchez-Silva, L.; Valverde, J. L.; Romero, A. *Adv. Powder Technol.* **2017**.
- (65) Stankovich, S.; Dikin, D. A.; Piner, R. D.; Kohlhaas, K. A.; Kleinhammes, A.; Jia, Y.; Wu, Y.; Nguyen, S. T.; Ruoff, R. S. *Carbon N. Y.* **2007**, *45* (7), 1558–1565.
- (66) Yang, Z.; Zheng, Q.; Qiu, H.; LI, J.; Yang, J. *New Carbon Mater.* **2015**, *30* (1), 41–47.
- (67) Liu, C.; Hao, F.; Zhao, X.; Zhao, Q.; Luo, S.; Lin, H. *Sci. Rep.* **2014**, *4*, 3965.
- (68) Schroeder, K. L.; Goreham, R. V.; Nann, T. *Pharmaceutical Research.* **2016**, 2337–2357.
- (69) Zhu, Y.; Wang, G.; Jiang, H.; Chen, L.; Zhang, X. *Chem. Commun.* **2015**, *51* (5), 948–951.

- (70) Gong, Y.; Li, D.; Fu, Q.; Pan, C. *Prog. Nat. Sci. Mater. Int.* **2015**, *25* (5), 379–385.
- (71) Bacon, M.; Bradley, S. J.; Nann, T. *Part. Part. Syst. Charact.* **2014**, *31* (4), 415–428.
- (72) Shen, J.; Zhu, Y.; Yang, X.; Li, C. *Chem. Commun.* **2012**, *48* (31), 3686.
- (73) Sun, H.; Wu, L.; Wei, W.; Qu, X. *Mater. Today* **2013**, *16* (11), 433–442.
- (74) Röding, M.; Bradley, S. J.; Nydén, M.; Nann, T. *J. Phys. Chem. C* **2014**, *118* (51), 30282–30290.
- (75) Dong, Y.; Shao, J.; Chen, C.; Li, H.; Wang, R.; Chi, Y.; Lin, X.; Chen, G. *Carbon N. Y.* **2012**, *50* (12), 4738–4743.
- (76) Trindade, T.; O’Brien, P.; Pickett, N. L. *Chem. Mater.* **2001**, *13* (11), 3843–3858.
- (77) Parvin, M. H. *Electrochem. commun.* **2011**, *13* (4), 366–369.
- (78) Urbanová, V.; Bakandritsos, A.; Jakubec, P.; Szambó, T.; Zbořil, R. *Biosens. Bioelectron.* **2017**, *89*, 532–537.
- (79) Oliveira, T. M. B. F.; Fátima Barroso, M.; Morais, S.; Araújo, M.; Freire, C.; de Lima-Neto, P.; Correia, A. N.; Oliveira, M. B. P. P.; Delerue-Matos, C. *Biosens. Bioelectron.* **2013**, *47*, 292–299.
- (80) Liu, F. mei; Du, Y. qiu; Cheng, Y. mei; Yin, W.; Hou, C. jun; Huo, D. qun; Chen, C.; Fa, H. bao. *J. Solid State Electrochem.* **2016**, *20* (3), 599–607.
- (81) Li, S.-J.; Qian, C.; Wang, K.; Hua, B.-Y.; Wang, F.-B.; Sheng, Z.-H.; Xia, X.-H. *Sensors Actuators B. Chem.* **2012**, *174*, 441–448.
- (82) Zhu, C.; Wang, X.; Shi, X.; Yang, F.; Meng, G.; Xiong, Q.; Ke, Y.; Wang, H.; Lu, Y.; Wu, N. *ACS Appl. Mater. Interfaces* **2017**.

- (83) Ensafi, A. A.; Noroozi, R.; Zandi—Atashbar, N.; Rezaei, B. *Sensors Actuators, B Chem.* **2017**, *245*, 980–987.
- (84) Maliyekkal, S. M.; Sreepasad, T. S.; Krishnan, D.; Kouser, S.; Mishra, A. K.; Waghmare, U. V.; Pradeep, T. *Small* **2013**, *9* (2), 273–283.
- (85) Gleiter, H. *Acta Mater.* **2000**, *48* (1), 1–29.
- (86) Hunter, G. W.; Xu, J. C.; Evans, L. J.; Wal, R. L. Vander; Gordon, M. *Chemical Sensors Based on Metal Oxide Nanostructures*; **2006**.
- (87) Wu, Z.-S.; Zhou, G.; Yin, L.-C.; Ren, W.; Li, F.; Cheng, H.-M. *Nano Energy* **2012**, *1* (1), 107–131.
- (88) Upadhyay, R. K.; Soin, N.; Roy, S. S. *RSC Adv.* **2014**, *4* (8), 3823–3851.
- (89) Imran Din, M.; Rani, A. *Int. J. Anal. Chem.* **2016**, *2016*, 1–14.
- (90) Yang, L.; Wang, G.; Liu, Y.; Wang, M. *Talanta* **2013**, *113*, 135–141.
- (91) Keivani, Z.; Shabani-Nooshabadi, M.; Karimi-Maleh, H. *J. Colloid Interface Sci.* **2017**, *507*, 11–17.
- (92) Golestanifar, F.; Karimi-maleh, H.; Atar, N.; Aydoğdu, E.; Ertan, B. *Int. J. Electrochem. Sci* **2015**, *10*, 5456–5464.
- (93) Keyvanfard, M.; Hatami, M.; Gupta, V. K.; Agarwal, S.; Sadeghifar, H.; Khalilzadeh, M. A. *J. Mol. Liq.* **2017**, *230*, 290–294.
- (94) Gong, J.; Wang, L.; Miao, X.; Zhang, L. *Electrochem. commun.* **2010**, *12* (11), 1658–1661.
- (95) Din, M. I.; Rehan, R. *Anal. Lett.* **2017**, *50* (1), 50–62.

- (96) Nolan, M.; Elliott, S. D. *Phys. Chem. Chem. Phys.* **2006**, 8 (45), 5350–5358.
- (97) Tran, T. H.; Nguyen, V. T. *Int. Sch. Res. Not.* **2014**, 2014, 1–14.
- (98) Veeramani, V.; Sivakumar, M.; Chen, S.-M.; Madhu, R.; Dai, Z.-C.; Miyamoto, N. *Anal. Methods* **2016**, 8 (30), 5906–5910.
- (99) Gu, W.; Wang, M.; Mao, X.; Wang, Y.; Li, L.; Xia, W. *Anal. Methods* **2015**, 7 (4), 1313–1320.
- (100) Shi, R.; Liang, J.; Zhao, Z.; Liu, A.; Tian, Y. *Talanta* **2017**, 169, 37–43.
- (101) Arvand, M.; Gholizadeh, T. M.; Zanjanchi, M. A. *Mater. Sci. Eng. C* **2012**, 32 (6), 1682–1689.
- (102) Liu, X.; Chen, C.; Zhao, Y.; Jia, B. *J. Nanomater.* **2013**, 2013, 1–7.
- (103) Preisler, E. *J. Appl. Electrochem.* **1976**, 6 (4), 311–320.
- (104) Foster, I.; Lee, J.; Tye, F. *J. Appl. Chem. Biotechnol.* **1972**, 22 (10), 1085.
- (105) Cockayne, E.; Li, L. *Chem. Phys. Lett.* **2012**, 544, 53.
- (106) Yan, X.; Song, Y.; Zhu, C.; Song, J.; Du, D.; Su, X.; Lin, Y. *ACS Appl. Mater. Interfaces* **2016**, 8 (34), 21990–21996.
- (107) Zaidi, S. A.; Shin, J. H. *RSC Adv.* **2015**, 5, 88996–89002.
- (108) Jaiswal, N.; Tiwari, I.; Foster, C. W.; Banks, C. E. *Electrochim. Acta* **2017**, 227, 255–266.
- (109) Kong, X.-J.; Wu, S.; Chen, T.-T.; Yu, R.-Q.; Chu, X. *Nanoscale* **2016**, 8 (34), 15604–15610.
- (110) Ghorbani, H. R. *Orient. J. Chem.* **2014**, 30 (4), 1941–1949.

- (111) Filatova, E. O.; Konashuk, A. S. *J. Phys. Chem. C* **2015**, *119* (35), 20755–20761.
- (112) Wei, Y.; Xu, R. X.; Gao, C.; Liu, J. H.; Huang, X. J. *Electrochem. commun.* **2012**, *18* (1), 78–80.
- (113) Schöning, M. J.; Arzdorf, M.; Mulchandani, P.; Chen, W.; Mulchandani, A. *Sensors Actuators, B Chem.* **2003**, *91* (1–3), 92–97.
- (114) Hyodo, T.; Hashimoto, T.; Ueda, T.; Nakagoe, O.; Kamada, K.; Sasahara, T.; Tanabe, S.; Shimizu, Y. *Sensors Actuators, B Chem.* **2015**, *220*, 1091–1104.

2. Experimental

2.1 Materials and solvents

Graphite flakes, paraffin oil, O,o-dimethyl O-(4-nitrophenyl) phosphorothioate (methyl parathion), nickel chloride hexahydrate ($\text{NiCl}_2 \cdot 6\text{H}_2\text{O}$), nickel nitrate hexahydrate ($\text{Ni}(\text{NO}_3)_2 \cdot 6\text{H}_2\text{O}$), copper chloride (CuCl_2), copper acetate ($\text{Cu}(\text{Ac})_2$), sodium citrate ($\text{Na}_3\text{C}_6\text{H}_5\text{O}_7$), manganese sulfate (MnSO_4), barium dichloride (BaCl_2), aluminium nitrate hexahydrate ($\text{Al}(\text{NO}_3)_3 \cdot 9\text{H}_2\text{O}$), glycine, ethylene diamine, triethylene diamine, tetraethylene pentamine and ammonia solution (NH_4OH , 30%), were purchased from Sigma-Aldrich. Sulphuric acid (H_2SO_4 , 98%), potassium permanganate (KMnO_4), hydrochloric acid (HCl , 32%), sodium hydroxide (NaOH) and hydrogen peroxide (H_2O_2 , 30%) were purchased from Merck, Durban South Africa.

2.2 Equipment

Fourier transform infrared (FT-IR) spectra were obtained using a Perkin-Elmer Spectrum 100 FT-IR spectrometer equipped with a diamond crystal ATR accessory. Ultraviolet-Visible (UV-vis) absorption spectra were recorded on a Shimadzu UV-2250 spectrophotometer. Photoluminescence (PL) spectra were recorded on a Perkin-Elmer, LS 55 fluorescence spectrometer. The scanning electron microscopy (SEM) images and elemental dispersive x-ray (EDX) graphs were obtained using a Zeiss ultra plus FEG scanning electron microscope equipped with a field emission gun. EDX measurements were acquired through a linked Oxford X-Max detector with an 18 mm spare window and processed using AZtec Software by Oxford instruments. The transmission electron microscopy (TEM) images were obtained from a JEOL 1010 microscope designed with an objective lens pole piece. Particle sizes were obtained using iTEM Software by Soft Imaging Solutions. X-ray diffraction analysis (XRD) were carried out

on a Bruker diffractometer D2 phaser, equipped with monochromatic $\text{CuK}\alpha$, radiation ($\lambda = 1.5406 \text{ \AA}$) for the graphene based materials. Diffractograms for the metal based materials were obtained from a Bruker D8 advance diffractometer equipped with $\text{CuK}\alpha$ radiation ($\lambda = 0.15406 \text{ nm}$). Thermogravimetric analysis (TGA) was carried out on a thermal analyser SDT Q600, V20.9 build 20. The data was collected from 0 - 1000 °C at a heating rate of 2 °C/min. Electrochemical measurements were carried out on a 797 VA Computrace Electrochemical Workstation (Metrohm instruments). Cyclic voltammetry (CV) data measurements were obtained using a three electrode system consisting of a platinum wire auxiliary electrode, a Ag|AgCl pseudo reference electrode and graphene-QD paste or glassy carbon electrode as the working electrode (3 mm).

2.3 Electrochemical methods

The GCE was modified using the drop-dry method.¹ The GCE was cleaned by gentle polishing in aqueous slurry of alumina nano-powder on a silicon carbide-emery paper. The electrode was further cleaned in double distilled water to remove residual alumina particles that could have been trapped on the surface and it was dried at room temperature. The suspensions of GQDs, metal oxide (MO) and metal hydroxide (MOH) nanoparticles were prepared in 2 mL of DMF and vigorously sonicated to obtain a homogenous mixture. 20 μL drops of the prepared suspensions were dropped on the bare GCE and dried at room temperature for 15 min to obtain GCE-GQDs/MO and GCE-GQDs/MOH. Electrocatalysis experiments were performed in a 0.1 M phosphate buffer solution (PBS, pH 7) containing 2 μM of MP.

Graphene electrodes were fabricated using a well-known procedure². A copper wire was cleaned by polishing with sandpaper. The graphene paste mixture was prepared by mixing 0.5 g of graphene powder with 180 μL of paraffin oil using a mortar and a pestle. The mixture was

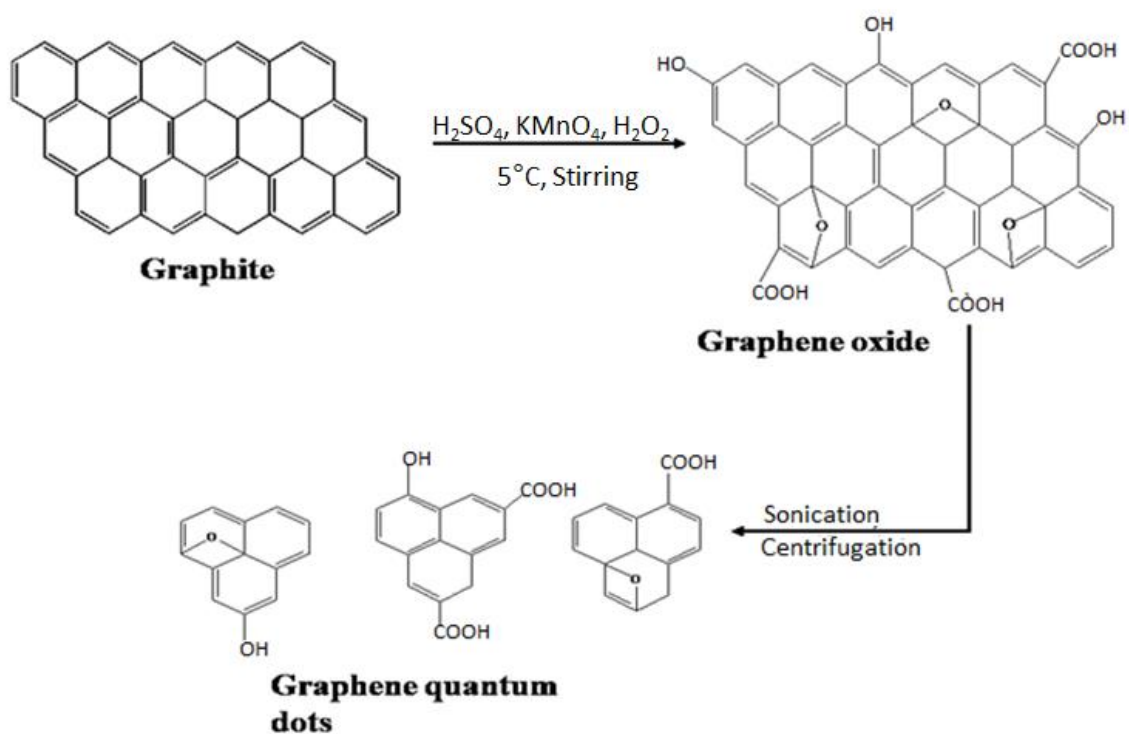
homogenized for 25 min and then packed into an auto pipette tip. The electrical contact was made by pushing a copper wire coated with silver paste down the pipette.

2.4 Synthesis of graphene based materials

2.4.1 Graphene oxide (GO) and graphene quantum dots (GQDs)

Powdered graphite was oxidized to graphite oxide (GrO) by a modified Hummers method.³ Briefly, 2.0 g of graphite powder was added to 100 mL of concentrated H₂SO₄ at room temperature. Under stirring the mixture was cooled to 5 °C using an ice bath and the mixture was maintained at this temperature for 30 min. Thereafter, 8.0 g of KMnO₄ was added gradually over a period of 60 min keeping the temperature below 10 °C. Distilled water (100 mL) and H₂O₂ (20 mL, 30%) were added to the mixture and the suspension was continually stirred for a further 60 min. The GO mixture was filtered and washed with HCl (800 mL, 5%) and left to air dry for 48 h.

In a 250 mL round bottom flask GQDs were synthesized according to scheme 2.1. A homogenous mixture was formed by mixing 50 mL of 0.1 mol KMnO₄ with 50 mL of a 1mg/mL GO suspension. This mixture was sonicated for 4 hours to ensure a sufficient reduction process. The mixture was then centrifuged for 90 min at 6000 rpm. The supernatant containing GQDs was collected and left to air dry for 72h.⁴



Scheme 2.1: Synthesis of GQDs via a modified Hummer's method.³

2.5 Synthesis of metal oxide nanoparticles

2.5.1 Copper oxide (Cu_2O) nanoparticles

Cuprous oxide nanoparticles were prepared using a previously reported procedure.⁵ In a 500 mL three-necked flask, 25 mg of CuCl_2 was dissolved in 200 mL of deionised water (DI). The mixture was sonicated for an hour at room temperature. A sodium citrate solution (120 mL, 10 %) was slowly added to the mixture under continuous stirring at 100°C for 24 hours, resulting in a precipitate of Cu_2O nanoparticles. The mixture was then filtered and washed with DI to dissolve by-products and the solid product was dried at 80°C for 24 hours under vacuum to obtain Cu_2O nanoparticles.

2.5.2 Nickel oxide (NiO) nanoparticles

Nickel (II) chloride hexahydrate ($\text{NiCl}_2 \cdot 6\text{H}_2\text{O}$, 5.9412 g) was dissolved in 250 mL of double distilled water at room temperature. The solution was stirred at 50 °C for 40 min, thereafter 10 mL of NaOH was added dropwise until the solution was at pH 8. The green gel that formed was washed with distilled water and ethanol and then dried at 60 °C for 14 h. The dried sample was calcined at 500 °C to give NiO powder.⁶

2.5.3 Aluminium oxide (Al_2O_3) nanoparticles

Aluminium oxide (Al_2O_3) nanoparticles were prepared according to literature⁷ by dissolving 10 g of aluminium nitrate hexahydrate [$\text{Al}(\text{NO}_3)_3 \cdot 9\text{H}_2\text{O}$] in water while stirring at room temperature. Thereafter 10 g of glycine was added to the solution under stirring and the temperature was increased to 100 °C, resulting in a brown precipitate. The mixture was stirred for 3 hours, cooled to room temperature and finally calcined at 600 °C for 4 hours.

2.5.4 Manganese oxide (MnO_2) nanoparticles

MnO_2 nanoparticles were prepared from the reduction of KMnO_4 with H_2SO_4 during hydrothermal treatment.⁸ Potassium permanganate (4g) was dissolved in H_2SO_4 (2.5 M, 200 mL) at 80 °C for 60 min while stirring. The precipitates obtained underwent a colour change from purple to brown. The brown precipitate was cooled to room temperature, washed thoroughly with deionized water and air dried for 48 hours.

2.6 Synthesis of metal hydroxide nanoparticles.

2.6.1 Copper hydroxide $\text{Cu}(\text{OH})_2$ nanoparticles

The synthesis of copper hydroxide $\text{Cu}(\text{OH})_2$ nanoparticles was carried out through a solution method.⁹ NaOH (1M, 60 mL) was added to a $\text{Cu}(\text{Ac})_2$ (0.4 M, 75 mL) solution under slow stirring at room temperature. After 5 min of stirring, the resultant blue precipitate ($\text{Cu}(\text{OH})_2$) was filtered, washed with distilled water several times and dried at room temperature for 24 h.

2.6.2 Nickel hydroxide $(\text{Ni}(\text{OH})_2)$ nanoparticles

Nickel hydroxide ($\text{Ni}(\text{OH})_2$) nanoparticles were synthesized through a hydrothermal route.¹⁰ Briefly, 1.26 g of nickel nitrate hexahydrate [$\text{Ni}(\text{NO}_3)_2 \cdot 6\text{H}_2\text{O}$] was dissolved in 50 mL of deionised water. The suspension was left to stand for 24 hours. NaOH solution (40 mL, 0.22 M) was added to the solution under vigorous stirring. After 30 min of stirring, the solution was transferred to an autoclave which was kept at 180 °C for 10 hours. The solid product was separated, washed with deionised water and finally air dried.

2.6.3 Aluminium hydroxide $(\text{Al}(\text{OH})_3)$ nanoparticles

Aluminium hydroxide nanoparticles were prepared using a precipitation method.¹¹ Briefly, 1 g aluminium nitrate hexahydrate was dissolved in 33 mL of deionised water. Precipitation agents, such as ethylene diamine, triethylene tetraamine and tetraethylene pentamine were added until the pH of the solution reached 8. A white precipitate was obtained confirming the successful formation of $\text{Al}(\text{OH})_3$. The precipitate was centrifuged and washed with deionised water and later dried at 70 °C for 24 h under a vacuum.

2.6.4 Manganese hydroxide (Mn(OH)₂) nanoparticles

Manganese hydroxide (Mn(OH)₂) nanoparticles were also synthesized via a co-precipitation method.¹² MnSO₄ (5g) was dissolved in 25 mL of aqueous ammonia (NH₄OH, 1M) solution at room temperature. The mixture was left to stand for 2h to increase precipitate yield. The Mn(OH)₂ brown precipitates were filtered and washed several times with distilled water until the SO₄²⁻ ions were non-existent. The efficient removal of SO₄²⁻ ions was determined by the addition of BaCl₂. The absence of a BaSO₄ precipitate indicated the successful removal of SO₄²⁻ ions.

2.7 Metal oxide (MO) or metal hydroxide (MOH)/graphene quantum dot composite preparation

An aqueous suspension of a metal oxide or metal hydroxide (2 mL) was prepared and added dropwise into 2 mL aqueous GQDs suspension under vigorous sonication. The mixture was sonicated for 3h to ensure sufficient interfacial interaction through electrostatic interaction. The resulting MO/GQDs or MOH/GQDs composites. The materials were centrifuged at 8000 rpm for 60 min and the composites were air dried for 24h.¹³

2.8 References

- (1) Mphuthi, N. G.; Adekunle, A. S.; Fayemi, O. E.; Olasunkanmi, L. O.; Ebenso, E. E. *Sci. Rep.* **2017**, *7*, 43181.
- (2) Parvin, M. H. *Electrochem. commun.* **2011**, *13* (4), 366–369.
- (3) Hummers, W. S.; Offeman, R. E. *J. Am. Chem. Soc.* **1958**, *80* (6), 1339–1339.
- (4) Zhu, Y.; Wang, G.; Jiang, H.; Chen, L.; Zhang, X. *Chem. Commun.* **2015**, *51* (5), 948–951.
- (5) Qian, Y.; Ye, F.; Xu, J.; Le, Z. G. *Int. J. Electrochem. Sci.* **2012**, *7* (10), 10063–10073.
- (6) Rahdar, A.; M. Aliahmad; Y. Azizi. *J. nanostructures* **2015**, *5*, 145–151.
- (7) Farahmandjou, M.; Golabiyani, N. *Trans. Phenom. Nano Micro Scales* **2015**, *3* (2), 100–105.
- (8) Gokulakrishnan, K. *Res. J. Chem. Environ. Sci.* **2014**, *2*, 55–58.
- (9) Ayask, H. K.; Khaki, J. V.; Haddad Sabzevar, M. *J. Ultrafine grained nanostructured Mater.* **2015**, *48* (1), 37–44.
- (10) Zheng, C. H.; Liu, X.; Chen, Z. D.; Wu, Z. F.; Fang, D. L. *J. cent. South Univ.* **2014**, *21*, 2596–2603.
- (11) Goudarzi, M.; Ghanbari, D.; Salavati-niasari, M. *J. nanostructures* **2015**, *5* (2), 110–115.
- (12) Peng, T.; Longjun Xu, H. C. *Cent. Eur. J. Chem.* **2010**, *8* (5), 1059–1068.
- (13) Xiao, W.; Zhou, W.; Feng, T.; Zhang, Y.; Liu, H.; Tian, L. *Materials.* **2016**, *9* (9).

- (1) Mphuthi, N. G.; Adekunle, A. S.; Fayemi, O. E.; Olasunkanmi, L. O.; Ebenso, E. E. *Sci. Rep.* **2017**, *7*, 43181.
- (2) Parvin, M. H. *Electrochem. commun.* **2011**, *13* (4), 366–369.
- (3) Hummers, W. S.; Offeman, R. E. *J. Am. Chem. Soc.* **1958**, *80* (6), 1339–1339.
- (4) Zhu, Y.; Wang, G.; Jiang, H.; Chen, L.; Zhang, X. *Chem. Commun.* **2015**, *51* (5), 948–951.
- (5) Qian, Y.; Ye, F.; Xu, J.; Le, Z. G. *Int. J. Electrochem. Sci.* **2012**, *7* (10), 10063–10073.
- (6) Rahdar, A.; M. Aliahmad; Y. Azizi. *J. nanostructures* **2015**, *5*, 145–151.
- (7) Farahmandjou, M.; Golabiyani, N. *Trans. Phenom. Nano Micro Scales* **2015**, *3* (2), 100–105.
- (8) Gokulakrishnan, K. *Res. J. Chem. Environ. Sci.* **2014**, *2*, 55–58.
- (9) Ayask, H. K.; Khaki, J. V.; Haddad Sabzevar, M. *J. Ultrafine grained nanostructured Mater.* **2015**, *48* (1), 37–44.
- (10) Zheng, C. H.; Liu, X.; Chen, Z. D.; Wu, Z. F.; Fang, D. L. *J. cent. South Univ.* **2014**, *21*, 2596–2603.
- (11) Goudarzi, M.; Ghanbari, D.; Salavati-niasari, M. *J. nanostructures* **2015**, *5* (2), 110–115.
- (12) Peng, T.; Longjun Xu, H. C. *Cent. Eur. J. Chem.* **2010**, *8* (5), 1059–1068.
- (13) Xiao, W.; Zhou, W.; Feng, T.; Zhang, Y.; Liu, H.; Tian, L. *Materials.* **2016**, *9* (9).

Results

and

Discussion

Results and discussion

This study focused on the investigation of novel sensor materials for the electrochemical detection of methyl parathion. Graphene was used as the sensing material due to its high electrical conductivity and large surface area. Composites of graphene quantum dots with metal nanoparticles were also explored as sensing materials with the anticipation of improved catalytic performance.

The results obtained in this work are separated into two chapters:

Chapter 3: Synthesis and characterisation of nanomaterials

Chapter 4: Electrode fabrication and electrocatalysis of methyl parathion on modified electrodes.

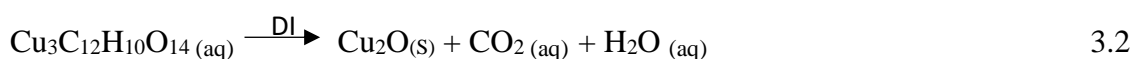
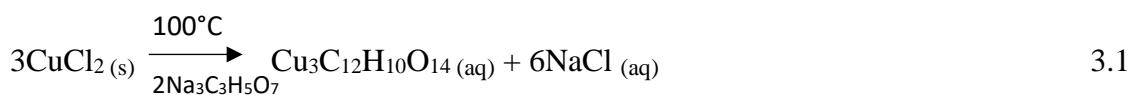
3. Synthesis and characterisation of nanomaterials

3.1 Synthesis of graphene quantum dots (GQDs)

The synthesis of GQDs involves the chemical oxidation of graphite to graphene oxide through Hummers method using oxidising agents such potassium permanganate. Graphene is initially prepared from graphite through exfoliation¹, which is a process of detaching graphene from an already existing graphite crystal.² The oxidation of graphene exfoliates and reduces the graphitic layered structure of graphite to graphene oxide (GO). The exfoliation and fragmentation of graphene oxide into thin sheets and/or dots referred to as graphene quantum dots was facilitated by ultra-sonication and centrifugation. Further exfoliation of the graphene oxide sheets was achieved by the addition of potassium permanganate.³

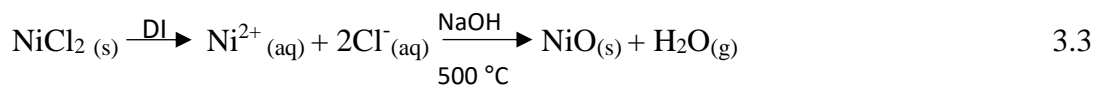
3.2 Synthesis of metal oxide (MO) and metal hydroxide (MOH) nanoparticles

The copper, nickel and aluminium based nanoparticles were synthesized through co-precipitation in the presence of the respective precursor metal salt and a base. An anion was added to a prepared solution of a cation (metal salt) while stirring forming a precipitate.³ In the formation of Cu₂O NPs, Cu(II)Cl₂ was thermally converted in the presence of sodium citrate solution to Cu(I) under sonication⁴ (reaction 3.1). The obtained compound Cu₃C₁₂H₁₀O₁₄ dissociated in DI water producing Cu₂O, CO₂ and H₂O as shown in reaction 3.2

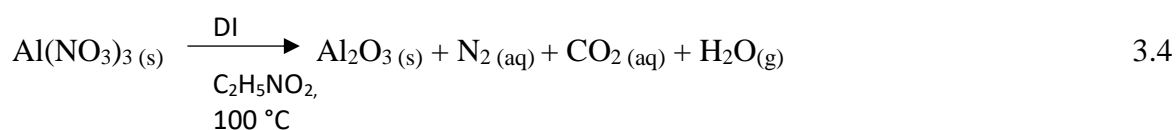


The NiO NPs were also synthesized through co-precipitation with the use of NiCl₂ as the precursor salt.⁵ Reaction 3.3 shows the dissociation of NiCl₂ forming Ni²⁺ and Cl⁻ ions in water.

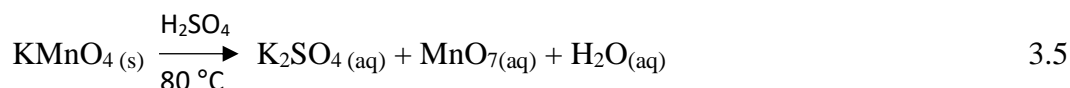
In the addition of sodium hydroxide Ni(OH)₂ formed and it thermally decomposed to form NiO nanoparticles and H₂O_(g) at 500 °C.



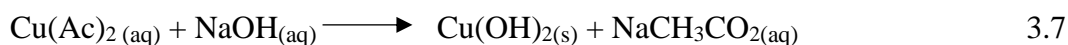
Reaction 3.4 shows the formation of aluminium oxide nanoparticles from co-precipitation of Al(NO₃)₃ and glycine at high temperatures.⁶ Aluminium nitrate was dissolved in DI water forming Al³⁺ and NO₃⁻ ions. Upon the addition of glycine, Al₂O₃ nanoparticles were produced.



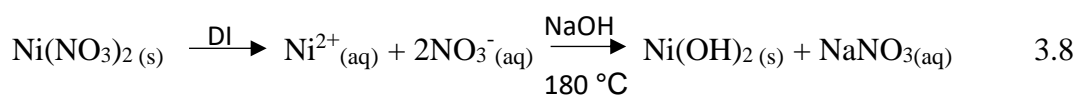
MnO₂ NPs were synthesized using potassium permanganate and sulphuric acid as starting material via hydrothermal treatment⁷ according to reaction 3.5. KMnO₄ was dissolved in sulphuric acid forming K₂SO₄, MnO₇ and H₂O. The resulting MnO₇ (reaction 3.6) was dissolved in water to produce MnO₂ nanoparticles.



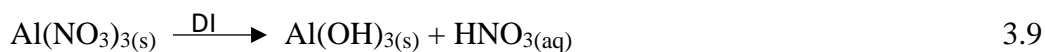
Copper hydroxide nanoparticles were synthesized *via* a solution method by stirring, using copper acetate and sodium hydroxide as starting materials according to reaction 3.7.⁸



Nickel nitrate was used as a salt precursor for the formation of Ni(OH)₂ NPs as shown in reaction 3.8.⁹ The salt was dissolved in DI water forming Ni²⁺ and NO₃⁻ ions, when NaOH was added to the solution Ni(OH)₂ nanoparticles formed.



Aluminium nitrate was also used for the formation of Al(OH)₃ NPs at room temperature according to reaction 3.9.¹⁰ Al(NO₃)₃ was simply dissolved in water to form aluminium hydroxide nanoparticles.



The Mn(OH)₂ NPs were also synthesized through co-precipitation¹¹ using MnSO₄ as the salt precursor according to reaction 3.10. The salt was dissolved in ammonium solution leading to the production of the nanoparticles.



3.2.1 Synthesis of GQDs-MO or GQDs-MOH composites

The GQDs-MO or GQDs-MOH composites were prepared by sonication and centrifugation.¹² An aqueous suspension of metal oxide or metal hydroxide NPs (2 mL) was added dropwise into a 2 mL aqueous suspension of GQDs under vigorous sonication for 1h. The mixture was further sonicated for 3 h to ensure sufficient electrostatic interaction of the GQDs with the MO or MOH to form the composite.

3.3 Characterisation of synthesized nanomaterials

3.3.1 UV-vis spectroscopy of graphene nanoparticles

The ultraviolet-visible (UV-vis) and photoluminescence (PL) spectra of GQDs are shown in Fig 3.1. The UV-vis spectrum (Fig 3.1a) shows two absorption peaks. The peak at 222 nm is ascribed to the π - π^* transition of aromatic C=C bond and the peak at 315 nm was assigned to

the $n\text{-}\pi^*$ transition of $\text{C}=\text{O}$ ¹³. Fig 3.1b the emission spectrum of GQDs were two peaks are observed. An excitation wavelength of 240 nm was used and the emission peak at 470 nm was attributed to the $\pi\text{-}\pi^*$ transitions of GQDs.^{14,15} The red-shifted emission peak at 540 nm corresponds to the electron transition among the non-oxidised ($\text{C}=\text{C}$) and the oxidised carbon atoms ($\text{C}-\text{OH}$).^{14,16} The other possible reason for this maybe due to the presence of GQDs different sizes which is known to have red shift.^{17,18} The larger GQDs absorb the photons emitted by their smaller GQDs followed by the subsequent re-emission at longer wavelengths.¹⁷

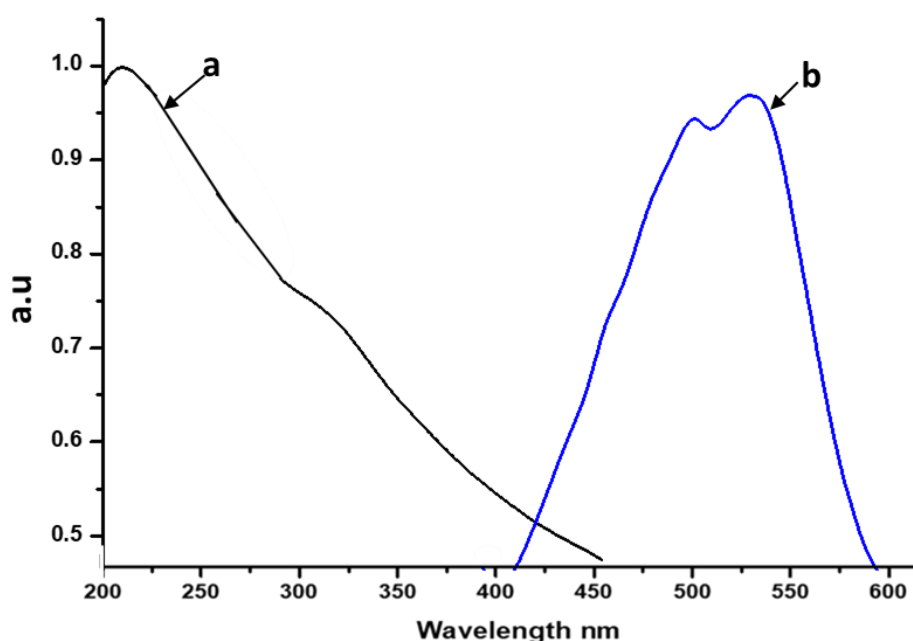


Fig 3.1: UV-vis (a) and emission (b) spectra for GQDs.

A large Stoke shift of 315 nm was observed, this was attributed to the quick geometric relaxation as a result of fast absorption and emission of photons.¹⁹ A large stoke shift is produced as a result of the difference between the ground state (S_0) and excited state (S_1) state based on the Jablosnki diagram shown in Fig 3.2. When a molecule gets excited from the S_0 state due to photon absorption (Fig 3.2a) upon relaxation the emitted photon usually has less

energy than the absorbed photon due to energy lost during internal conversion and vibrational relaxation (3.2b), this shifts the energy of the photon to longer wavelengths.²⁰

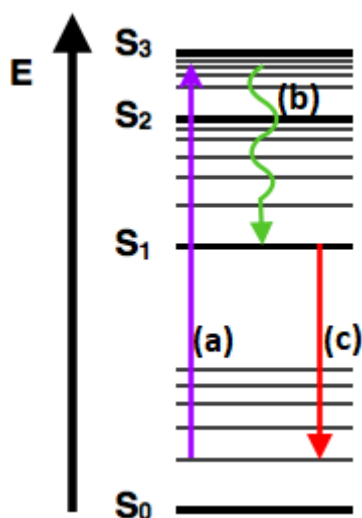


Fig 3.2: Jablonski diagram showing (a) absorption, (b) internal conversion and vibrational relaxation and (c) fluorescence processes.²¹

3.3.2 Fourier transform infrared analysis (FTIR) of GQDs

FTIR was used to determine the functional groups present in the synthesized nanomaterials. Fig 3.3a and 3.3b shows the spectra of GO and GQDs respectively. In Fig 3.3a the peaks at 3225 cm^{-1} , 1710 cm^{-1} , 1230 cm^{-1} and 1050 cm^{-1} were attributed to the O-H, C=O, C-O (epoxy and alkoxy) stretching vibrations of GO respectively. The presence of these oxygen-containing functional groups confirms the successful oxidation of graphite to graphene oxide. Fig 3.3b showed significant reduction in intensity of the OH and C=O peaks which signifies the successful reduction of oxygen containing groups. There was also a shift to lower wavenumber in all four peaks (OH 3210 cm^{-1} , C=O 1610 cm^{-1} , C-O_{epoxy} 1220 cm^{-1} and C-O_{alkoxy} 1000 cm^{-1}) which signifies the successful formation of GQDs from GO. A functional groups such as C=O has a

stronger bond energy compared to C-O or C=C, therefore the reduction of C=O and C-OH intensity leads to lower wavenumbers.²²

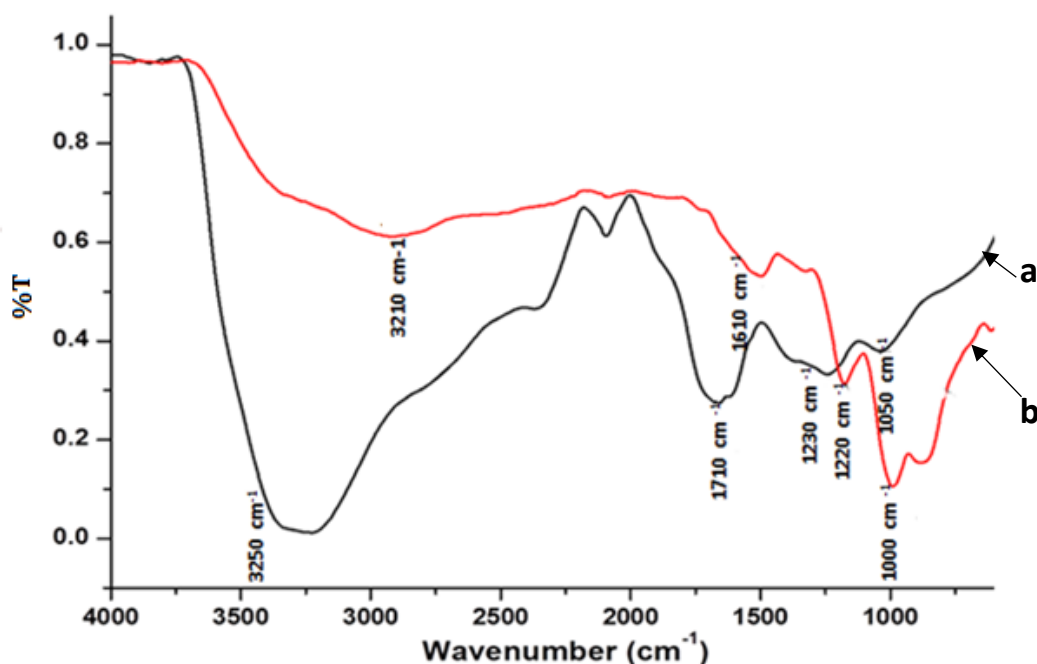


Fig 3.3: FTIR spectra of (a) GO and (b) GQDs.

3.3.3 Raman analysis of graphene nanoparticles

The Raman spectra for the graphene based materials shown in Fig 3.4 showed two distinct peaks one at 1350 cm^{-1} referred to as the D band and another at 1580 cm^{-1} as the G band for all Gr based materials. These peaks indicate that the material has defects in the basal plane (D band) and sp^2 lattice (G band). A peak at 2720 cm^{-1} which correspond to the 2D band was also observed in the materials. The 2D band indicates the number of layers a graphene based material possesses, as expected graphite has the highest number of layers, followed by GO then GQDs.²³ Fig 3.4a shows low-intensity of the D band and a sharp G band; this suggests that there is little destruction of the basal plane and sp^2 lattice in Gr. The sharp G band also indicates the crystallinity of Gr. The oxidation of Gr led to the high intensity of the D band and broadness

of the G band for both GO and GQDs (Fig 3.4 b and c) confirmed by the intensity ratios. The D and G bands appear broader than that of Gr indicating the amorphous nature of GO and GQDs. The change in the D band and G band indicated a higher degree of disorder in the lattice due to the incorporation of oxygen atoms.^{24,25} The intensity ratio of D and G bands (I_D/I_G) was used to determine the defective disorder in the materials. The I_D/I_G ratio for Gr was determined to be 0.16, for GO it was 0.61 and for GQDs it determined to be 0.69. These results indicate that GQDs have more defects followed by GO and lastly GR. This high level of disorder in GQDs is attributed to the many steps synthesis route.

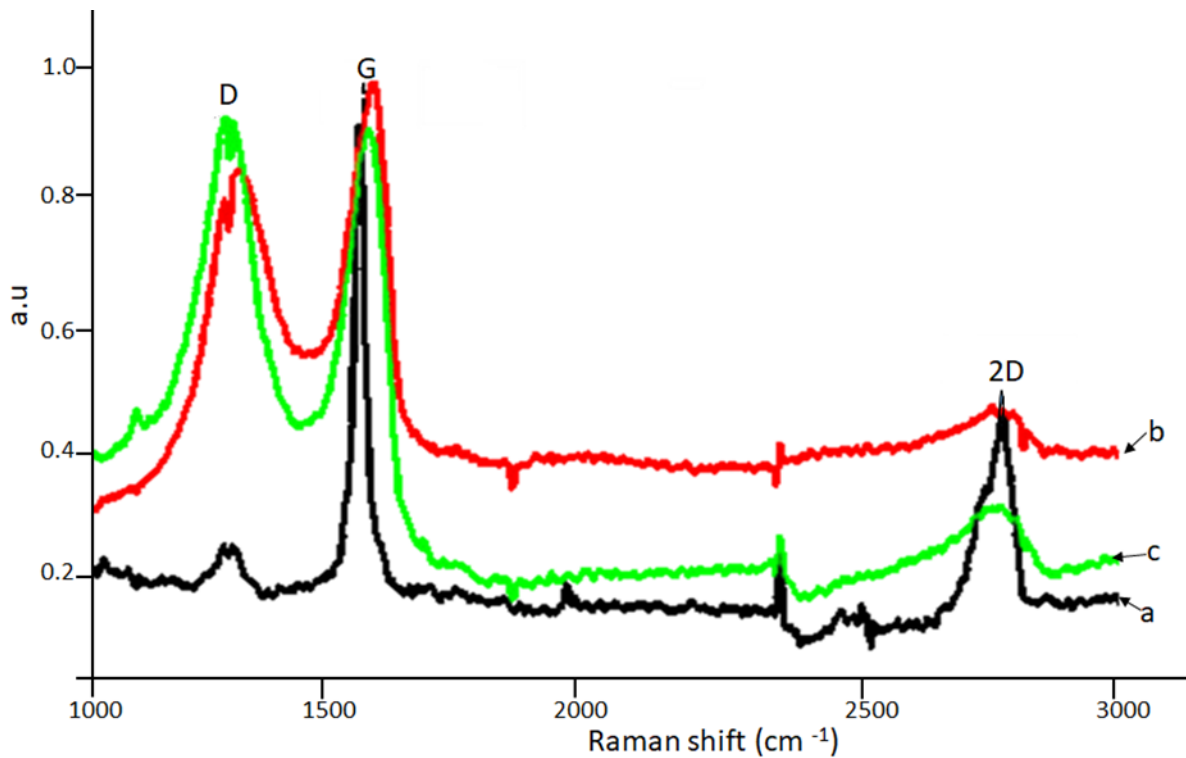


Fig 3.4: The Raman Spectra of (a) Gr; (b) GO and (c) GQDs.

3.4 Characterisation of metal oxide and metal hydroxide nanoparticles

3.4.1 FTIR spectra for copper nanoparticles

The FTIR spectrum of copper oxide nanoparticles is shown in Fig 3.5a which exhibits stretching vibrations at 1270 cm^{-1} , 1200 cm^{-1} and 600 cm^{-1} attributed to Cu(I)-O vibrations in Cu_2O .²⁶ No pure copper (II) oxide (CuO)²⁶ peaks were detected which would appear around 588 , 534 and 480 cm^{-1} . The FTIR peak observed at 600 cm^{-1} corresponds to the vibration of Cu-O (O^{2-}) inside the tetrahedron formed by four surrounding Cu^+ ions in a cuprite structure^{27,28}. Fig 3.5b shows the FTIR spectrum of $\text{Cu}(\text{OH})_2$ NPs, the figure shows an intense peak at 3326 cm^{-1} ascribed to OH stretching and another peak shown at 1640 cm^{-1} due to OH bending. The Cu(II)-O stretch was observed²⁹ at 715 cm^{-1} .

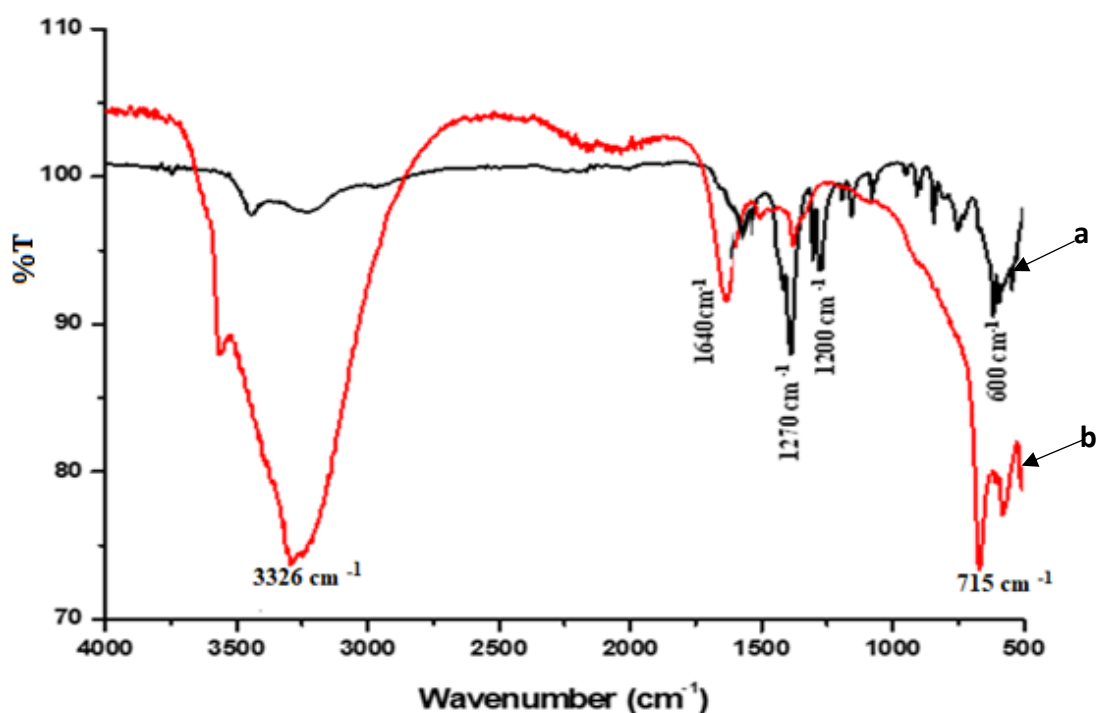


Fig 3.5: FTIR spectra of (a) Cu_2O and (b) $\text{Cu}(\text{OH})_2$ NPs.

3.4.2 FTIR spectra for nickel nanoparticles

The FTIR spectra for NiO and Ni(OH)₂ nanoparticles is shown in Fig 3.6a and 3.6b respectively. Fig 3.6a shows a peak at 810 cm⁻¹ and a shoulder peak at 495 cm⁻¹ ascribed to Ni-O functional group vibrations.⁵ Fig 3.6b exhibit peaks at 3330 cm⁻¹ and 1450 cm⁻¹ attributed to stretching and bending of the hydroxyl functional group respectively. The peak at 605 cm⁻¹ is due to the Ni-OH band stretch.^{30,31}

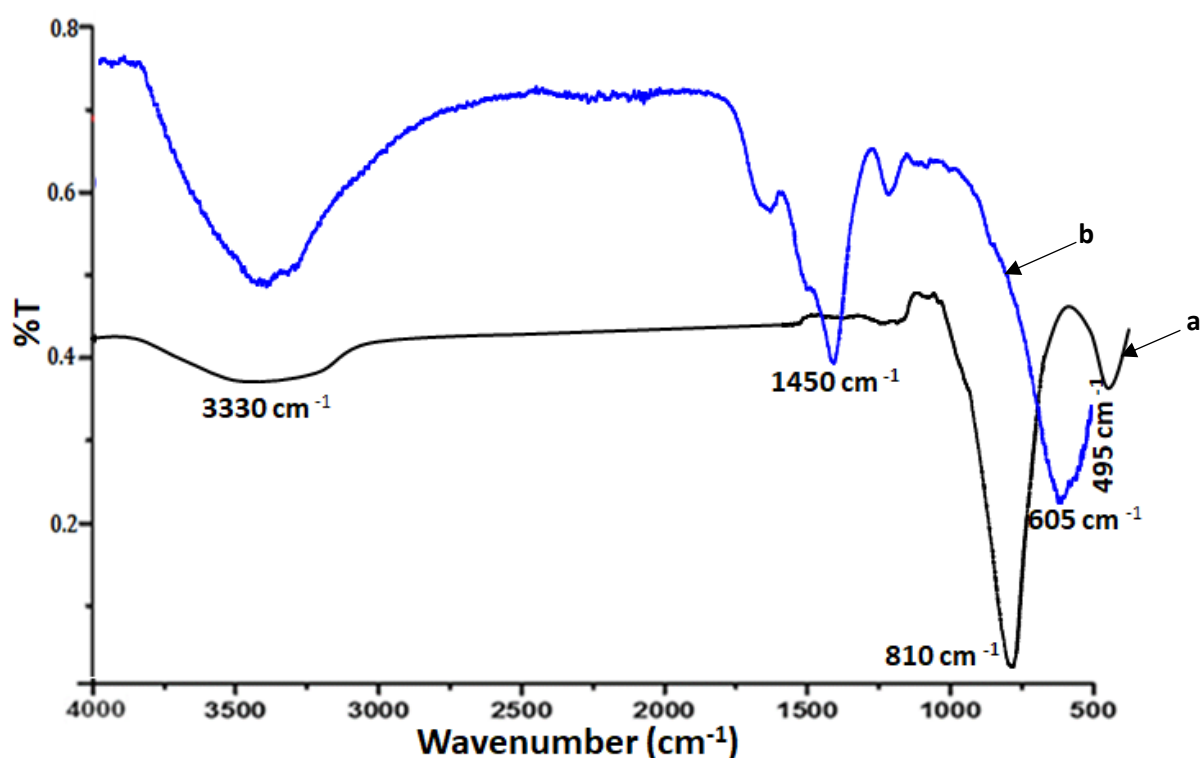


Fig 3.6: FTIR spectra of (a) NiO and (b) Ni(OH)₂ NPs.

3.4.3 FTIR spectra for aluminium nanoparticles

The FTIR spectrum of Al₂O₃ NPs is shown in Fig 3.7a where three major absorption peaks at 3320 cm⁻¹, 1620 cm⁻¹ and 485 cm⁻¹ are observed. These peaks are ascribed to the stretching and bending of the hydroxyl group and the Al-O group respectively. The presence of the OH peak for Al₂O₃ NPs is due to absorbed water despite the drying of the materials. The Al-O

stretch confirmed the successful formation of the Al₂O₃ NPs.^{32,33} The FTIR spectrum of Al(OH)₃ nanoparticles is shown in Fig 3.7b with peaks observed at 3320 cm⁻¹ and 1620 cm⁻¹ attributed to the stretching and bending of the OH group. The band at 510 cm⁻¹ is attributed to Al-O vibrations.^{34,35,36}

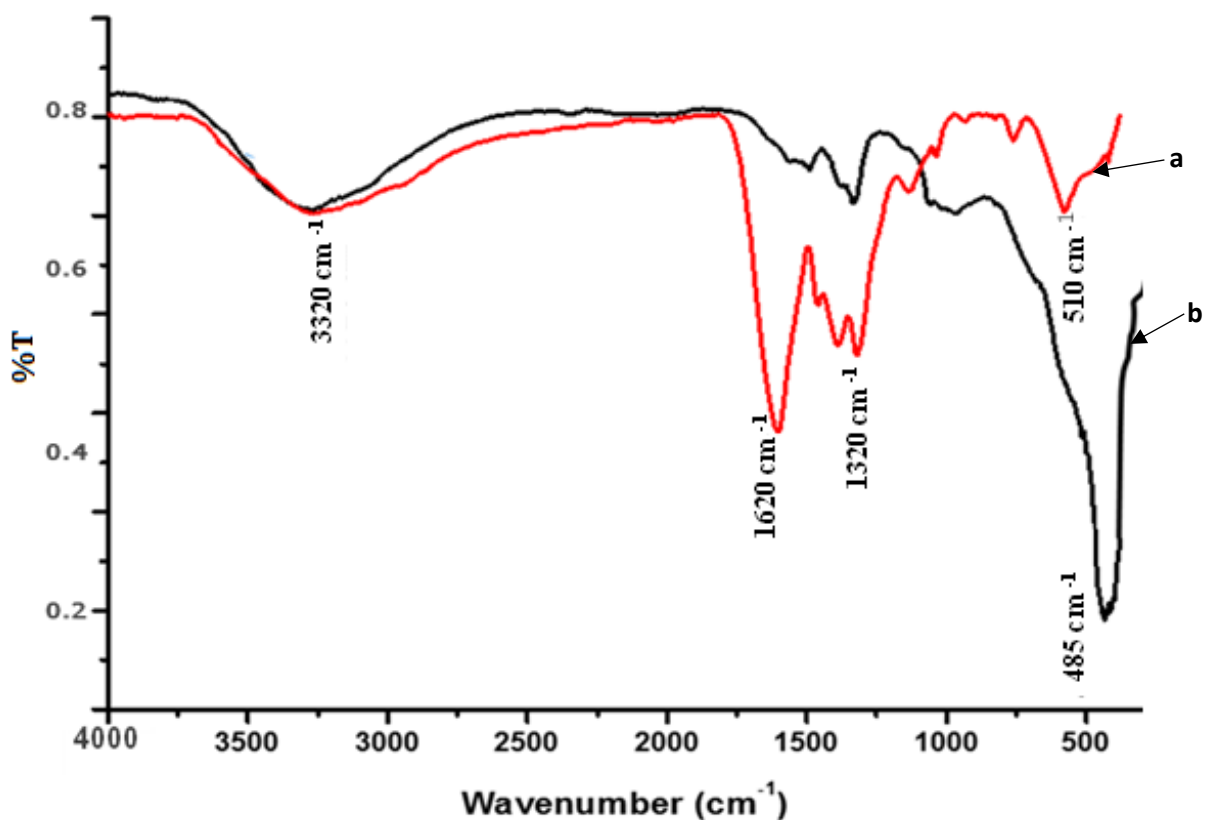


Fig 3.7: FTIR spectra of (a) Al₂O₃ and (b) Al(OH)₃ NPs.

3.4.4 FTIR spectra for manganese nanoparticles

Shown in Fig 3.8a and 3.8b is the FTIR spectra of MnO₂ and Mn(OH)₂ nanoparticles respectively. Fig 3.8a shows a prominent peak at 600 cm⁻¹ due to Mn-O vibrations.³⁷ A weak broad band was also observed at 3410 cm⁻¹ due to the water adsorbed on the lattice. The Mn(OH)₂ NPs spectrum (Fig 3.8b) shows absorption bands at 3410 cm⁻¹ and 1600 cm⁻¹

attributed to the stretching and bending of OH functional group respectively. The peaks at 1050 cm^{-1} and 750 cm^{-1} are attributed to Mn-O vibrations.³⁸

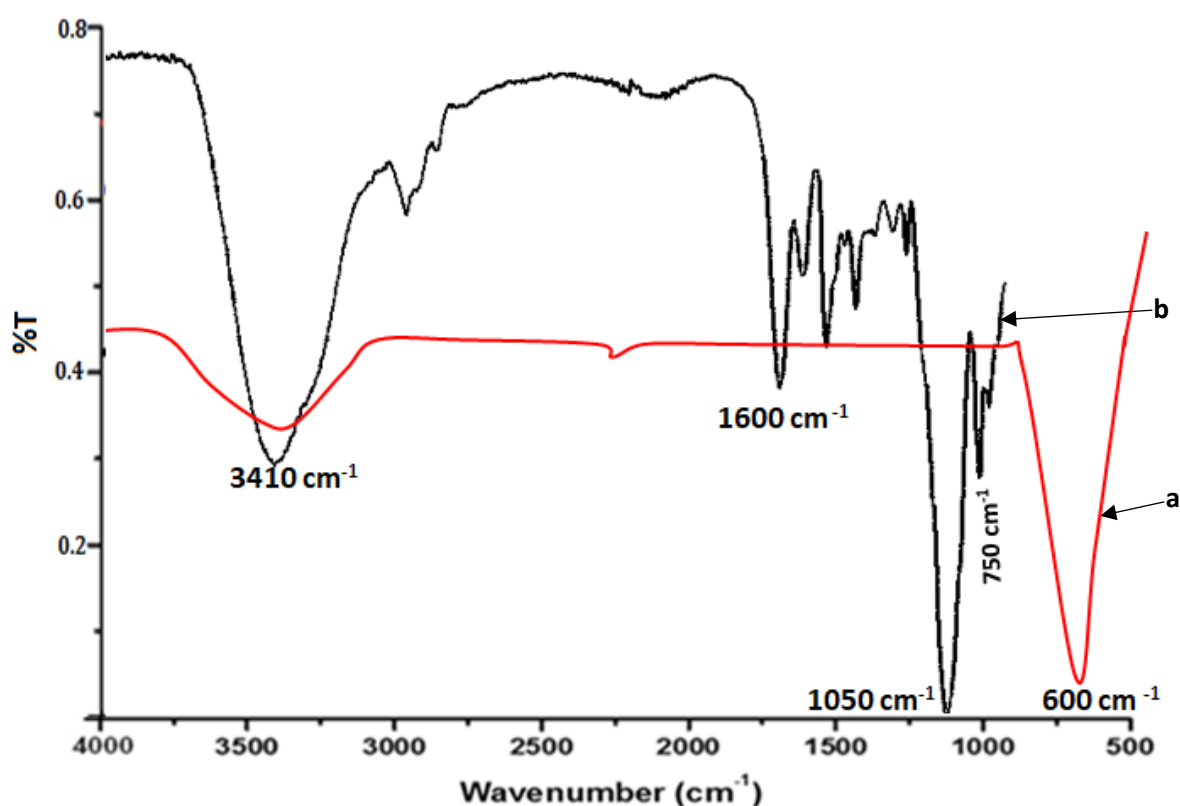


Fig 3.8: FTIR spectra of (a) MnO_2 and (b) Mn(OH)_2 nanoparticles.

3.5 X-ray diffraction (XRD) spectra

3.5.1 XRD pattern for graphene nanoparticles

The XRD spectra of the carbon based material is shown in Fig 3.9. Fig 3.9a shows the XRD spectrum of Gr. A sharp peak confirming the crystalline structure of Gr was observed at $2\theta = 27^\circ$, with an interlayer distance determined to be 3.30 Å. Upon oxidation of Gr to GO the interlayer distance increased to 7.08 Å, this led to an amorphous structure of GO confirmed by the broad peak at $2\theta = 12.5^\circ$ (Fig 3.9b insert). Upon reduction of GO to GQDs, the GQDs showed a slightly broad peak at $2\theta = 26.5^\circ$ corresponding to an interlayer distance of 3.36 Å

(Fig 3.9c). The slight broadness of the peak for GQDs suggested a semi-crystalline structure. The larger interlayer distance of GO and GQDs is mainly due to the presence of oxygen-containing functional groups that hydrate and exfoliate graphene sheets in aqueous media. The interlayer distance of GQDs was found to be smaller than that of GO which indicates that the partial reduction of oxygen in the GO lattice was successful when forming GQDs.

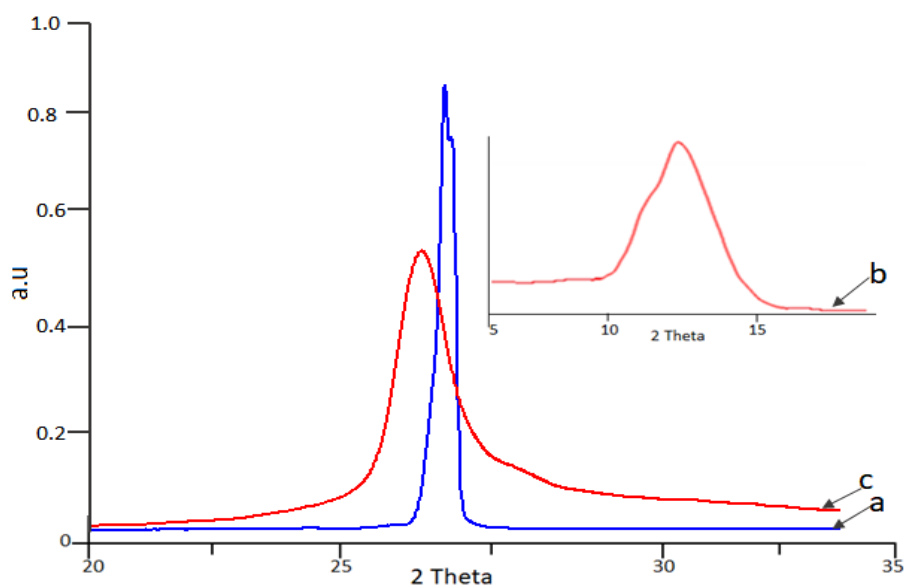


Fig 3.9: XRD spectra of (a) Gr, (b) GO (insert) and (c) GQDs.

3.5.2 XRD pattern for metal nanoparticles

3.5.2.1 XRD pattern for copper NPs

The crystallographic structure of the metal based nanoparticles was analysed by XRD. The XRD diffractogram for Cu_2O in Fig 3.10a show peaks at 32° , 35° , 49.5° , 77.5° and 79.5° , indexed to 110, 111, 200, 311 and 222 respectively. These peaks correlate to the face centred cubic (FCC) structure of Cu_2O in accordance to the library of the Joint Committee on Powder Diffraction Standards (JCPDS 05-0667).⁴⁰ Fig 3.10b shows the XRD pattern of $\text{Cu}(\text{OH})_2$ with

peaks at 12° , 19° , 24.5° , 37° , 47° , 58° and 73.5° , which correspond to indexes 020, 021, 110, 111, 150, 200 and 152 respectively. These peaks are consistent to the presence of an orthorhombic $\text{Cu}(\text{OH})_2$ structure (JCPDS 13-0420).⁴¹

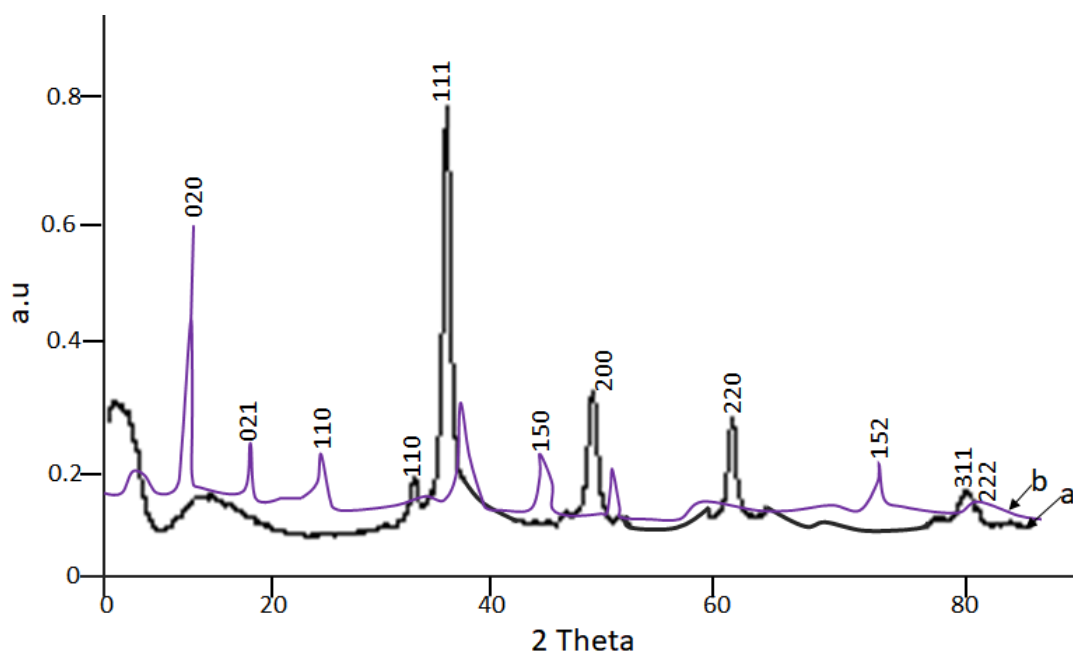


Fig 3.10: XRD spectra of (a) Cu_2O and (b) $\text{Cu}(\text{OH})_2$ NPs.

3.5.2.2 XRD pattern for nickel NPs

The diffractogram of NiO NPs shown in Fig 3.11 a, exhibits diffraction peaks at 37° , 43.3° , 63° , 77° and 80° , correlated to 111, 200, 220, 311 and 222 indexes respectively. The peaks can be readily indexed to the FCC crystalline structure of NiO not only because of peak position, but also by the relative characteristic peak intensity, which is in accordance with that of the standard spectrum (JCPDS 04-0835)⁴² The diffractogram for $\text{Ni}(\text{OH})_2$ NPs shown in Fig 3.11b has peaks at 18° , 30° and 60° , indexed to 100, 101 and 110 respectively for the amorphous β - $\text{Ni}(\text{OH})_2$ structure according to the library of diffraction standards (JCPDS 14-0117).⁴³ $\text{Ni}(\text{OH})_2$ is a hexagonal brucite and it exists in two polymorphs namely α and β . The β phase

is more stable than its counterpart and forms as a result of chemical ageing and high temperatures during synthesis.⁴⁴

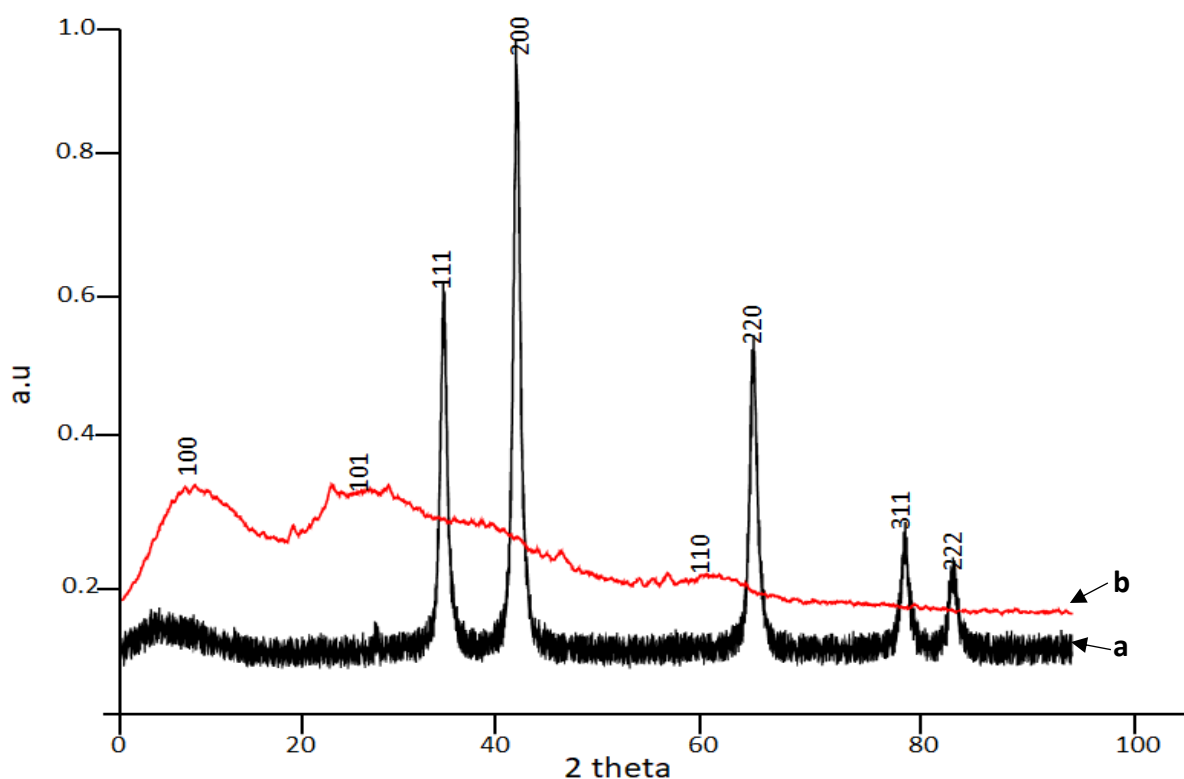


Fig 3.11: XRD spectra of (a) NiO and (b) Ni(OH)₂ NPs.

3.5.2.3 XRD pattern for aluminium NPs

The XRD pattern for Al₂O₃ NPs shown in Fig 3.12a shows peaks at 220, 311, 222, 400, 511 and 440 indexes corresponding to 2θ values of 5°, 19°, 30°, 39°, 55° and 60° respectively. The indexes confirmed the crystalline structure of the material to be γ-aluminium oxide (JCPDS 35-0121).⁴⁵ Al₂O₃ exists in a various polymorphs including γ-, η-, δ-, θ-, κ-, χ-alumina and α-alumina phase. The γ-Al₂O₃ NPs formed as a result of high temperatures.⁴⁶ Fig 3.12b shows the XRD pattern of Al(OH)₃ NPs with diffraction peaks at 12° (002), 19.2° (110), 35° (311), 43.5° (023) and 58° (330), which can be indexed to the monoclinic gibbsite phase of aluminium

hydroxide in accordance to card number (JCPDS PDF 00-33-0018)⁴⁷ of the diffraction standards.

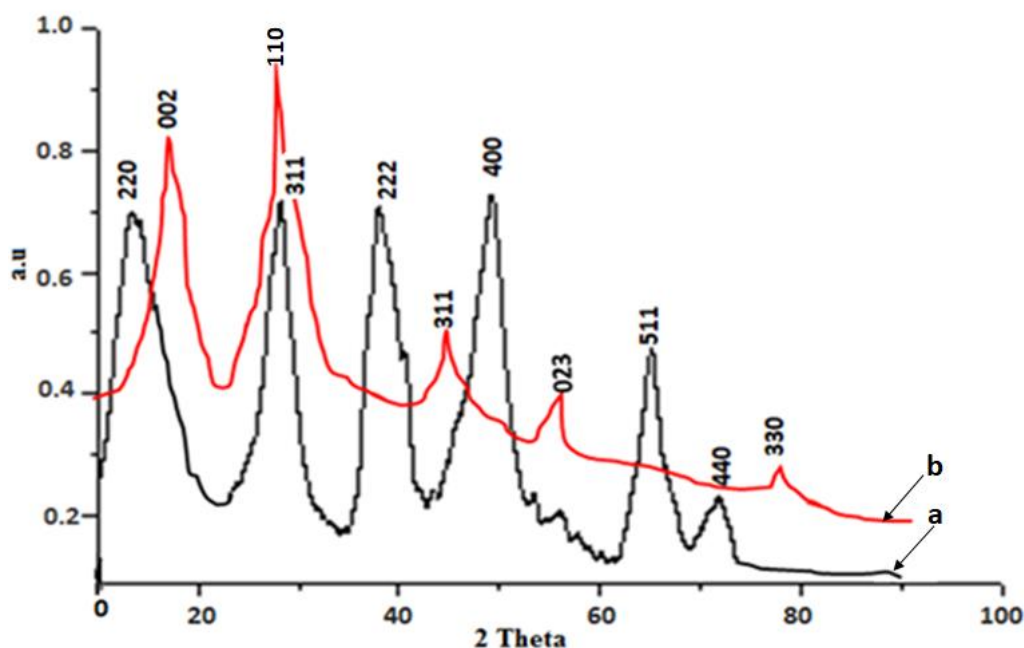


Fig 3.12: XRD spectra of (a) Al_2O_3 and (b) $\text{Al}(\text{OH})_3$ NPs.

3.5.2.4 XRD pattern for manganese NPs

The XRD pattern of MnO_2 NPs is shown in Fig 3.13a, displaying diffraction peaks at 2θ values of 12° , 33° , 37° and 66° , corresponding to indexes 001, 002, 111 and 020 respectively, correlated to an amorphous birnessite-type MnO_2 structure (JCPDS 80-1098).⁴⁸ The $\text{Mn}(\text{OH})_2$ NPs XRD pattern is shown in Fig 3.13b, with diffraction peaks at 32° (100), 39° (001), 51° (012), and 68° (111), indexed to a crystalline pyrochroite-type $\text{Mn}(\text{OH})_2$ according to card number (JCPDS 73-1604)⁴⁹ of diffraction standards library.

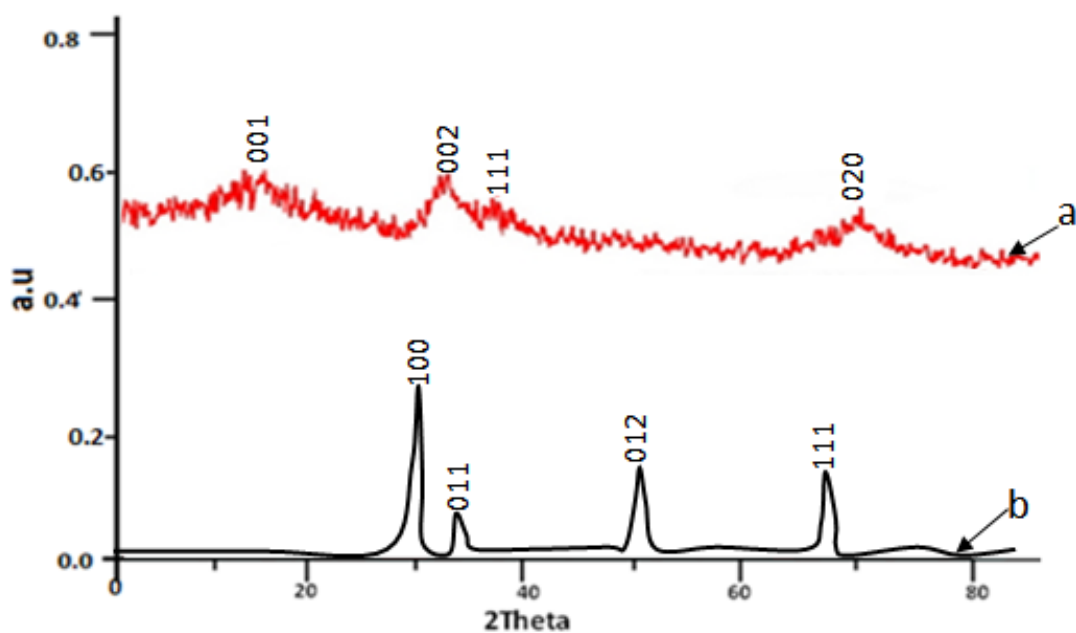


Fig 3.13: XRD spectra of (a) MnO₂ and (b) Mn(OH)₂ NPs.

3.6 TEM and SEM/EDX analysis of nanomaterials

Transmission electron microscopy (TEM) and size distribution analysis (SDA) were used to determine the morphology and particle size of the graphene, metal oxide and metal hydroxide nanoparticles. SDA was obtained by determining the standard deviation of the nanomaterial's particle size. Particles are said to be mono-dispersed if they have a low standard deviation range which indicates narrow size distribution whereas poly-dispersed nanoparticles have a high standard deviation range indicating wide size distribution.⁵⁰ Scanning electron microscopy (SEM) was used to determine surface morphology and elemental dispersive X-ray (EDX) was used for composition analysis.

3.6.1 TEM and SEM/EDX analysis of GQDs

The TEM image of GQDs is shown in Fig 3.14a, GQDs have a dot-like morphology with an average particle size diameter of 5 nm. The standard deviation of the particle size was determined to be 1.79 (Fig 3.14b) suggesting that the particles are mono-dispersed as observed.⁴² The surface morphology of the GQDs was also studied using SEM as shown in Fig 3.14c. A stack-of-sheets-like morphology was observed for GQDs confirming that the dots still contain graphene sheets. Elemental analysis obtained from EDX analysis (Fig 3.14d) showed the presence of oxygen which is expected for GQDs, however the unexpected presence of sulphur and potassium is attributed to sulphuric acid and potassium permanganate used during synthesis.

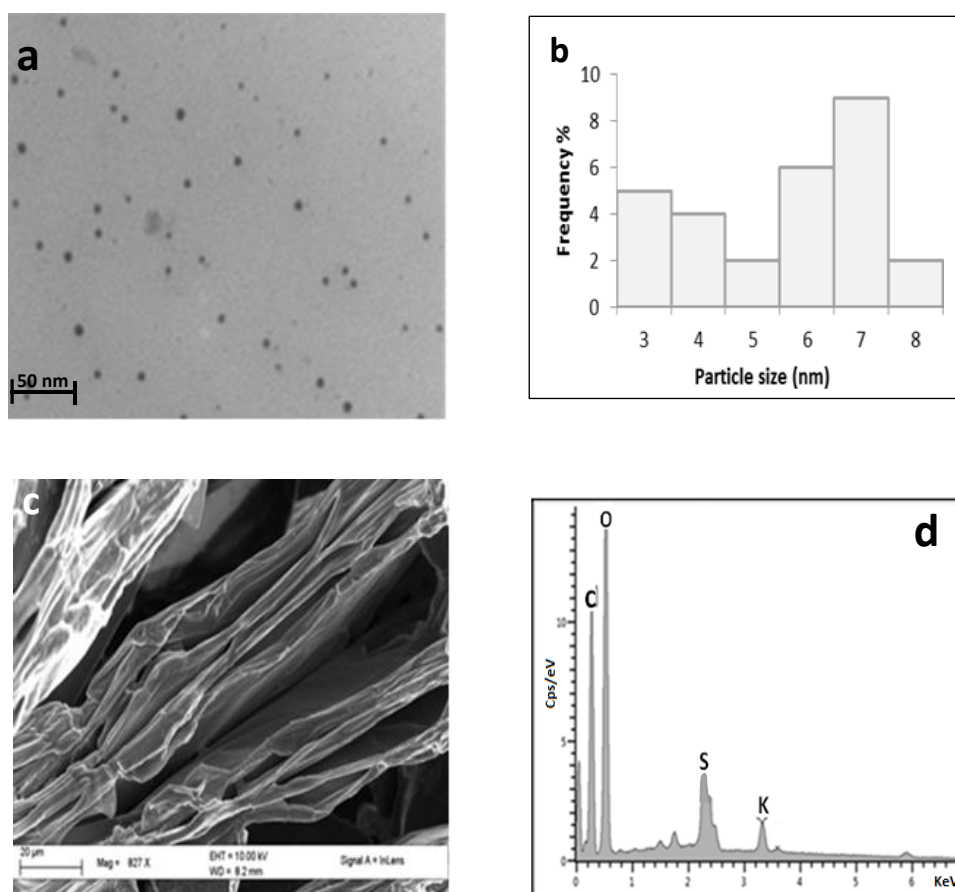
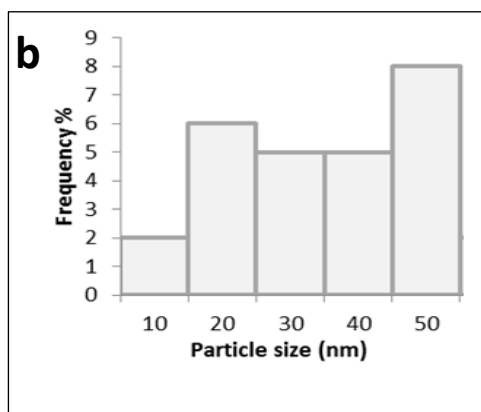
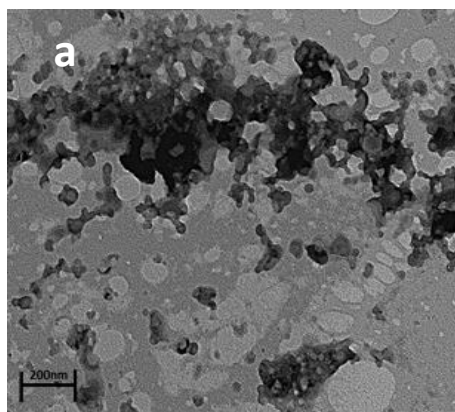


Fig 3.14: (a) TEM image, (b) SDA plot, (c) SEM image and (d) EDX spectrum of GQDs.

3.6.2 TEM and SEM/EDX analysis of metal oxide NPs

3.6.2.1 Analysis of Cu₂O NPs.

The TEM image of Cu₂O NPs is shown in Fig 3.15a and the NPs appear as aggregated spheres. A standard deviation of 14.13 suggested a poly-dispersion of particle size, with an average diameter size of 31 nm (Fig 3.15b). The SEM image (Fig 3.15c) showed a cluster of spheres, this agglomeration of Cu₂O NPs is usual in the absence of stabilizers.⁵² The agglomeration was prevented when the Cu₂O NPs were combined with GQDs. The elemental analysis obtained from the EDX (Fig 3.15d) confirmed the presence of elemental copper and oxygen signals of the Cu₂O nanoparticles. The elemental copper signals were detected at 0.930, 8.055 and 8.895 keV, these peaks arise from the atoms L shell (CuL_{α1}) and core K shell (CuK_{α1} and CuK_{β1}) respectively.⁵³ The Cu₂O NPs showed high purity as no impurities were detected from the EDX spectrum. Fig 3.15e shows the SEM image of GQDs/Cu₂O nanocomposite (NC). The Cu₂O NPs appear well-dispersed NPs on the surface and in between the graphene sheets.



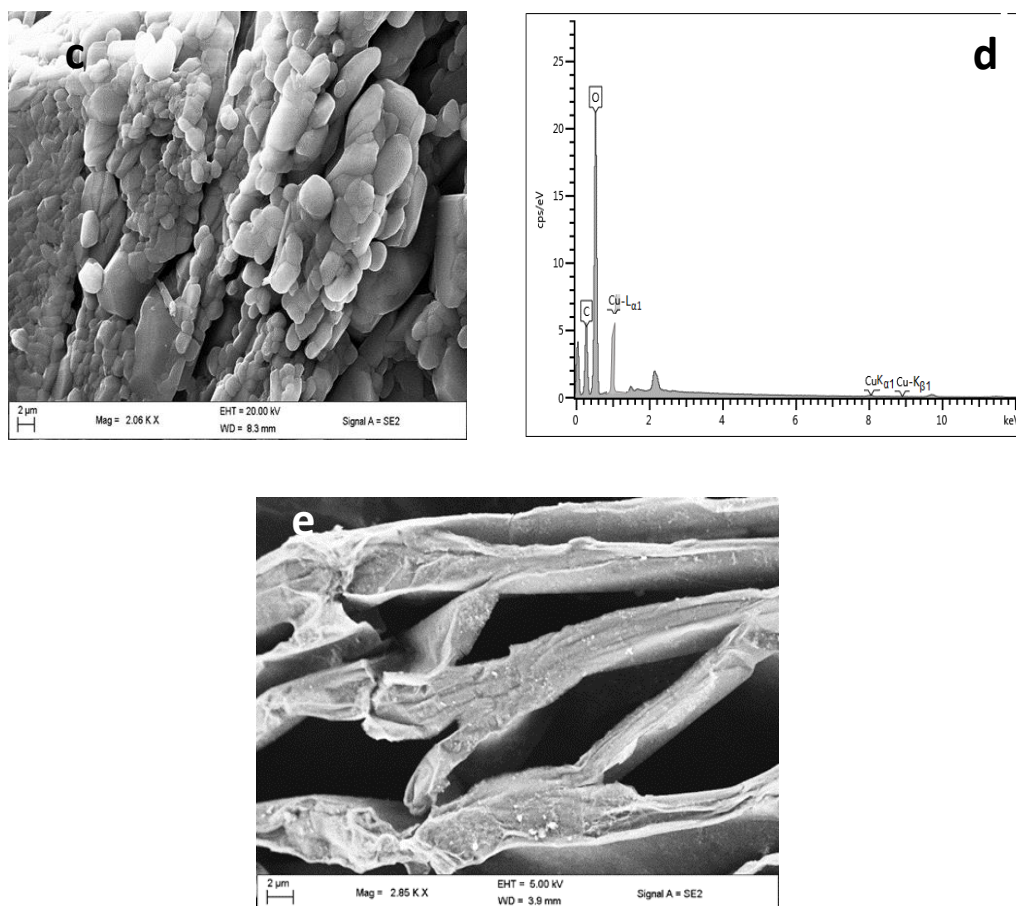


Fig 3.15: (a) TEM image, (b) SDA plot, (c) SEM image, (d) EDX spectrum of Cu₂O NPs and (e) SEM image of GQDs Cu₂O- NC.

3.6.6.2 Analysis of NiO NPs

A TEM image of nickel oxide NPs is shown in Fig 3.16a. The NiO NPs are aggregated and have a spherical morphology with an average particle size of 55 nm in diameter. The standard deviation of 13.65 confirmed the particle size distribution to be poly-dispersed⁵¹ (Fig 3.16b). The SEM image for NiO NPs in Fig 3.16c showed the nanoparticles as aggregated spheres. The EDX analysis in Fig 3.16d displayed the presence of oxygen and nickel elemental signals at different energy-level shells, where the L α 1 (0.853), K α 1 (7.500) and K β 1 (8.525) peaks were observed for Ni.⁵³ The nickel oxide NPs also demonstrated high purity as no impurities were detected. Fig 3.16e shows the SEM image of GQDs-NiO NC showing an even distribution of

NPs on graphene sheets demonstrating that graphene plays an important role in preventing the agglomeration of NiO nanoparticles. The image shows good exfoliation of graphene sheets as a result of the embedded nanoparticles.

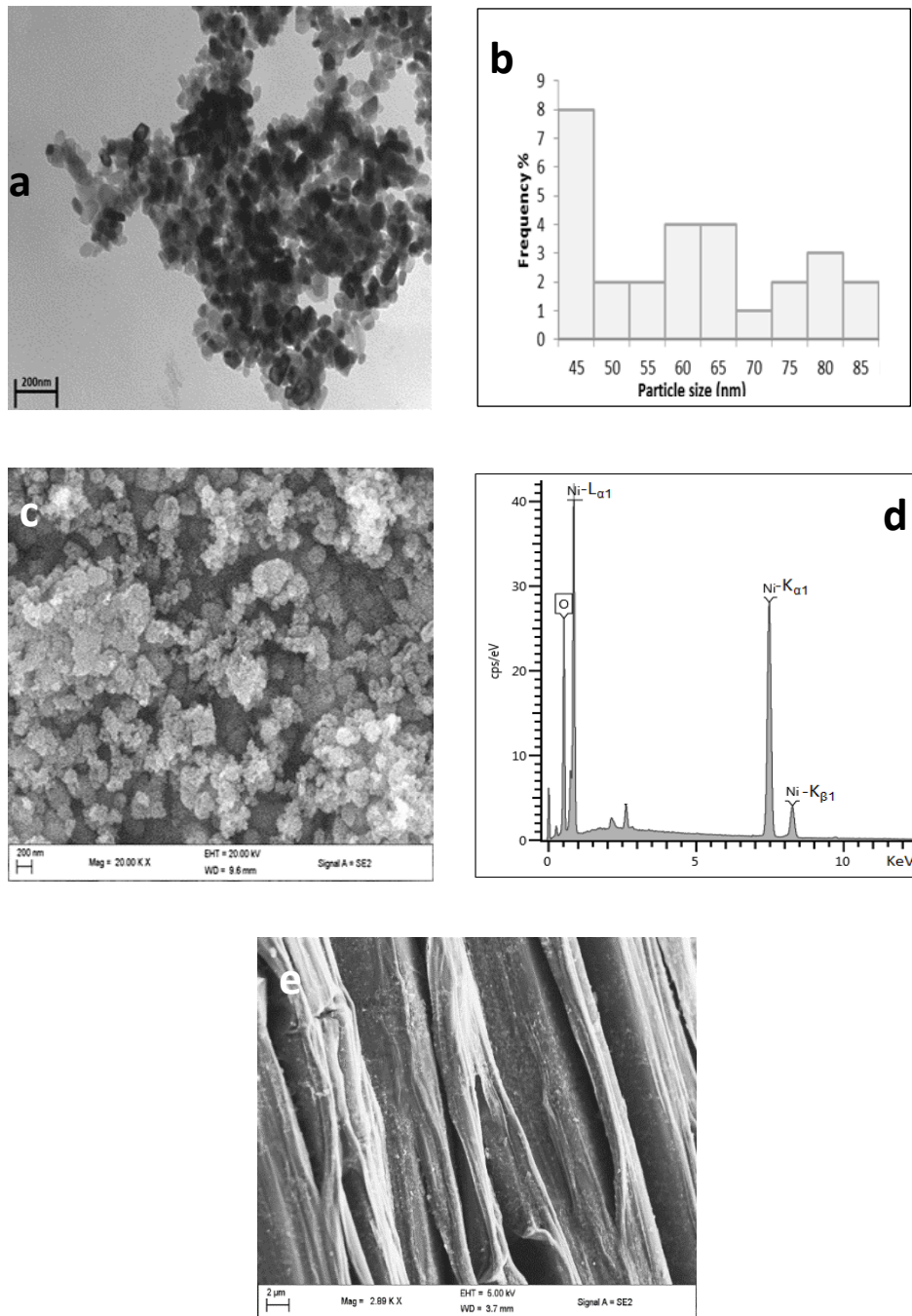
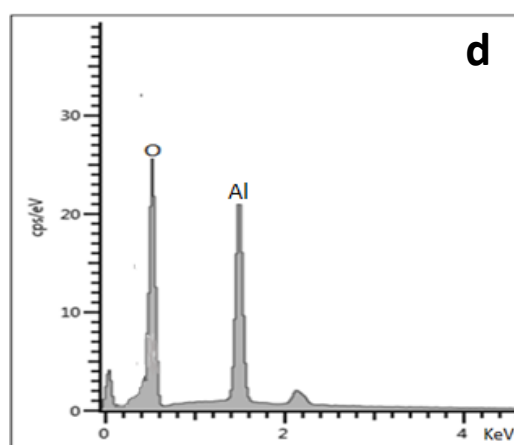
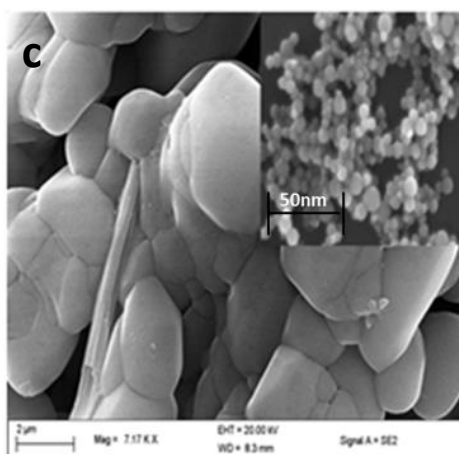
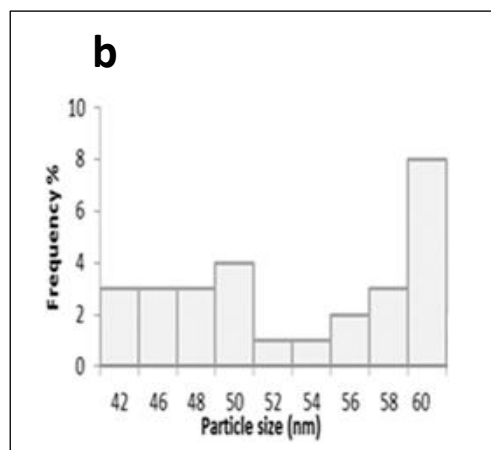
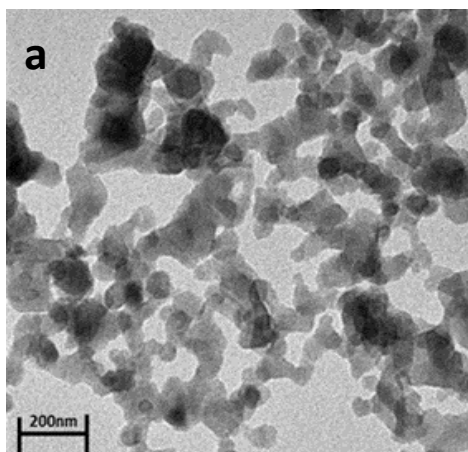


Fig 3.16: (a) TEM image, (b) SDA plot, (c) SEM image, (d) EDX spectrum of NiO NPs and (e) SEM image of GQDs-NiO NC.

3.6.2.3 Analysis of Al₂O₃ NPs

The TEM image of the aluminium oxide NPs shows spherical aggregated particles with an average particle size of 60 nm (Fig 3.17a). A standard deviation of 7.29 was determined suggesting mono-dispersion of particle sizes in Fig 3.17b. The corresponding SEM image in Fig 3.17c shows a smooth surface of spheres forming a cluster. The insert image shows the Al₂O₃ NPs morphology at nanoscale where a similar morphology of aggregated spheres is observed. The EDX analysis in Fig 3.17d shows the presence of elemental Al and O as expected for Al₂O₃ NPs. No impurities were detected by EDX indicating the high purity level of the NPs. The SEM of GQDs-Al₂O₃ NC (Fig 3.17e) shows graphene sheets decorated with Al₂O₃ NPs, the NPs are evenly dispersed within the GQDs.



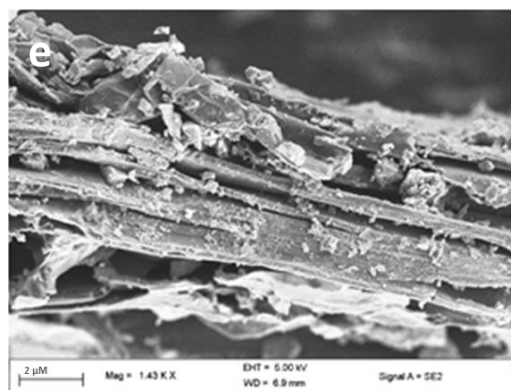


Fig 3.17: (a) TEM image, (b) SDA plot, (c) SEM images (insert: at nanoscale), (d) EDX spectrum of Al₂O₃ NPs and (e) SEM image of GQDs-Al₂O₃ NC.

3.6.2.4 Analysis of MnO₂ NPs

A TEM image of MnO₂ NPs in Fig 3.18a displays a spherical morphology for the NPs with an average diameter size of 70 nm. These spheres were determined to be poly-dispersed by the standard deviation of 18.14 from SDA (Fig 3.18b). The SEM image of these NPs shown in Fig 3.18c display spherically shaped NPs at microscale, the insert at nanoscale shows a flower-like morphology. EDX analysis in Fig 3.18d showed the presence of elemental O and Mn signals at 0.554, 6.000 and 6.325 keV for Mn arising from L_{α1}, K_{α1} and K_{β1} energy shell respectively.⁵³ MnO₂ NPs also showed a high level of purity as no impurities were detected by EDX. The SEM image of GQDs-MnO₂ NC (Fig 3.18d) shows well exfoliated graphene sheets as a result of MnO₂ NPs addition to the GQDs, which aid in preventing the re-stacking of graphene sheets. The graphene surface is wrinkled and decorated with MnO₂ spheres.

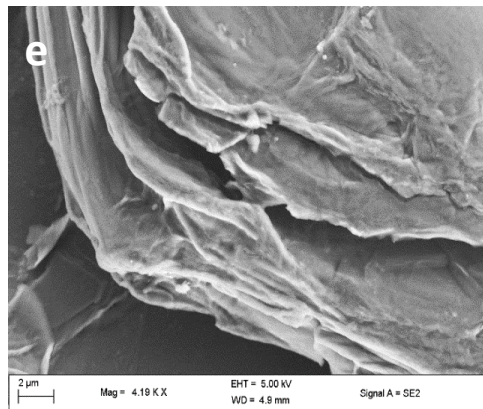
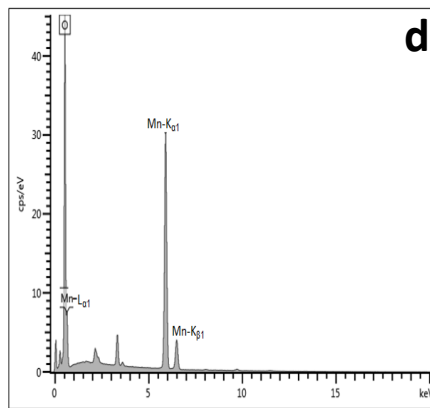
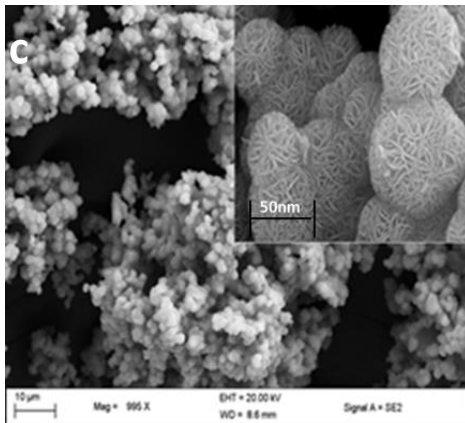
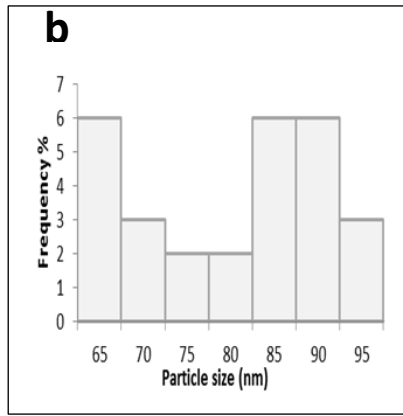
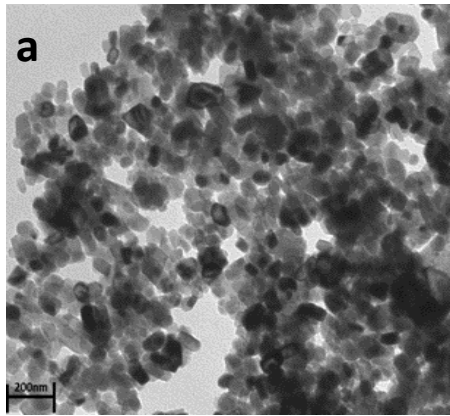
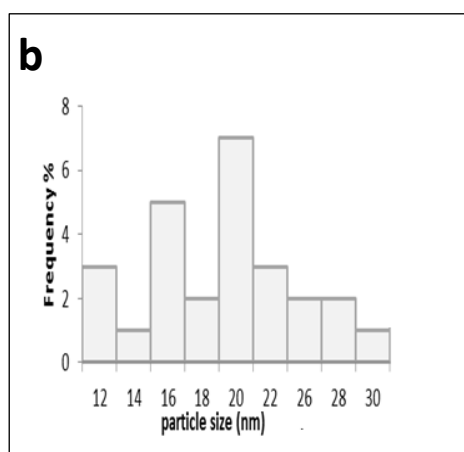
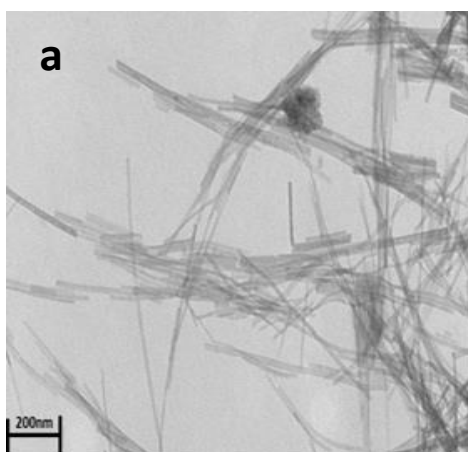


Fig 3.18: (a) TEM image, (b) SDA plot, (c) SEM images (insert: at nanoscale), (d) EDX spectrum for MnO₂ NPs and (e) SEM image of GQDs-MnO₂ NC.

3.6.3 TEM and SEM/EDX analysis of metal hydroxides

3.6.3.1 Analysis of Cu(OH)₂ NPs

The TEM image for copper hydroxide NPs is shown in Fig 3.19a. The NPs have a rod-like morphology with an average diameter size of 20 nm. The Cu(OH)₂ NPs were determined to be mono-dispersed according to the standard deviation of 6.31, suggesting that they have a narrow distribution of particle size (Fig 3.19b). The SEM image (Fig 3.19c) shows the nanoparticles as an interwoven network of numerous nanofibers. The EDX analysis in Fig 3.19d show copper signals corresponding to energy level shell, L_{α1}, K_{α1} and K_{β1} detected at 0.980, 8.001 and 8.920 keV respectively.⁵³ The presence of carbon in the spectrum (although in low concentration) comes from the use of copper acetate during synthesis. Fig 3.19e shows the SEM image of GQDs-Cu(OH)₂ NC displaying uniformly dispersed Cu(OH)₂ NPs on graphene surface. The cracks on the graphene sheets are a result of vigorous sonication and centrifugation during the nanocomposite synthesis.



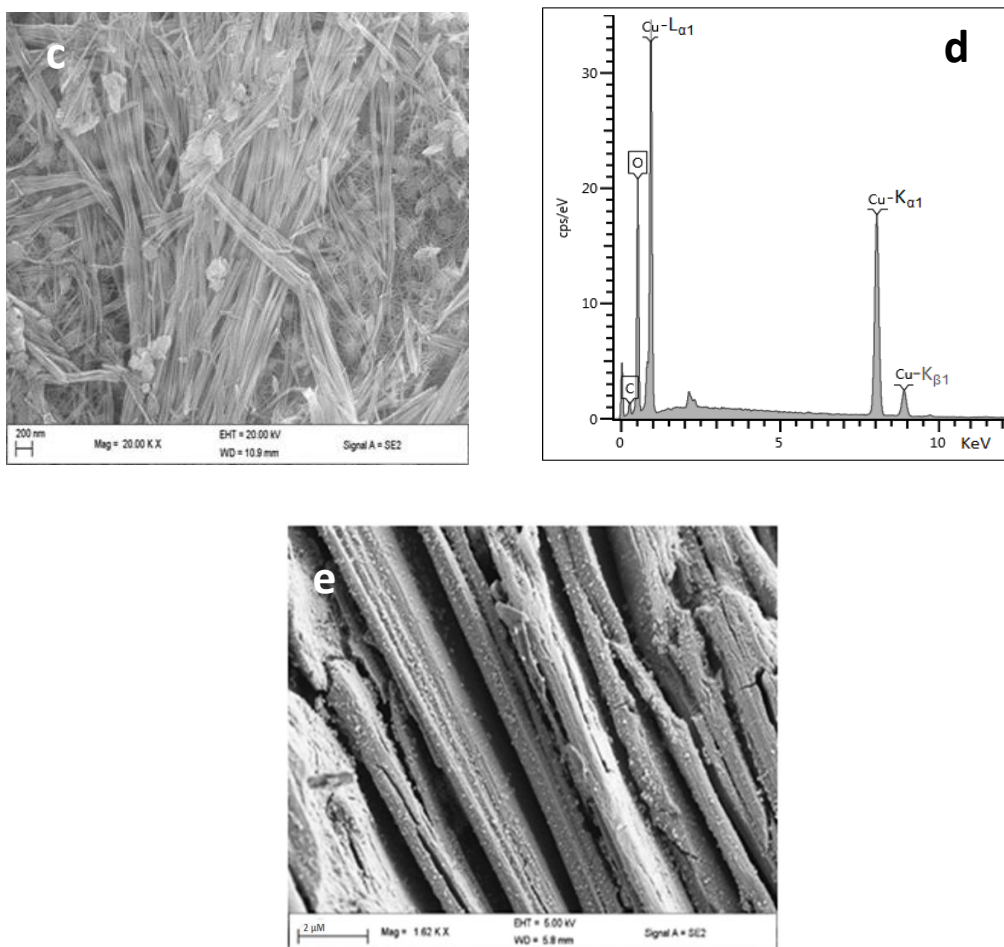


Fig 3.19: (a) TEM image, (b) SDA plot, (c) SEM image and (d) EDX spectrum for Cu(OH)₂ NPs and (e) SEM image of GQDs-Cu(OH)₂ NC.

3.6.3.2 Analysis of Ni(OH)₂ NPs

The TEM image of nickel hydroxide NPs exhibiting porous and spherical nanoparticles is shown in Fig 3.20a. The average particle size was determined to be approximately 50 nm in diameter and the NPs determined to be poly-dispersed according to the particle size standard deviation of 16.92 (Fig 3.20b). The SEM image at high magnification and nanoscale (Fig 3.20c insert) displayed aggregated spheres. The EDX analysis of the NPs (Fig 3.20d) showed three nickel elemental signals at L and K energy shells detected at 0.900 (L α_1), 7.500 (K α_1) and 8.430 (K β_1).⁵³ The presence of chloride is due to the use of nickel dichloride during synthesis. The

SEM image of GQDs-Ni(OH)₂ NC is shown in Fig 3.20e displaying evenly distributed Ni(OH)₂ NPs on graphene quantum dot surface. This image shows high loading of the NPs compared to other composites.

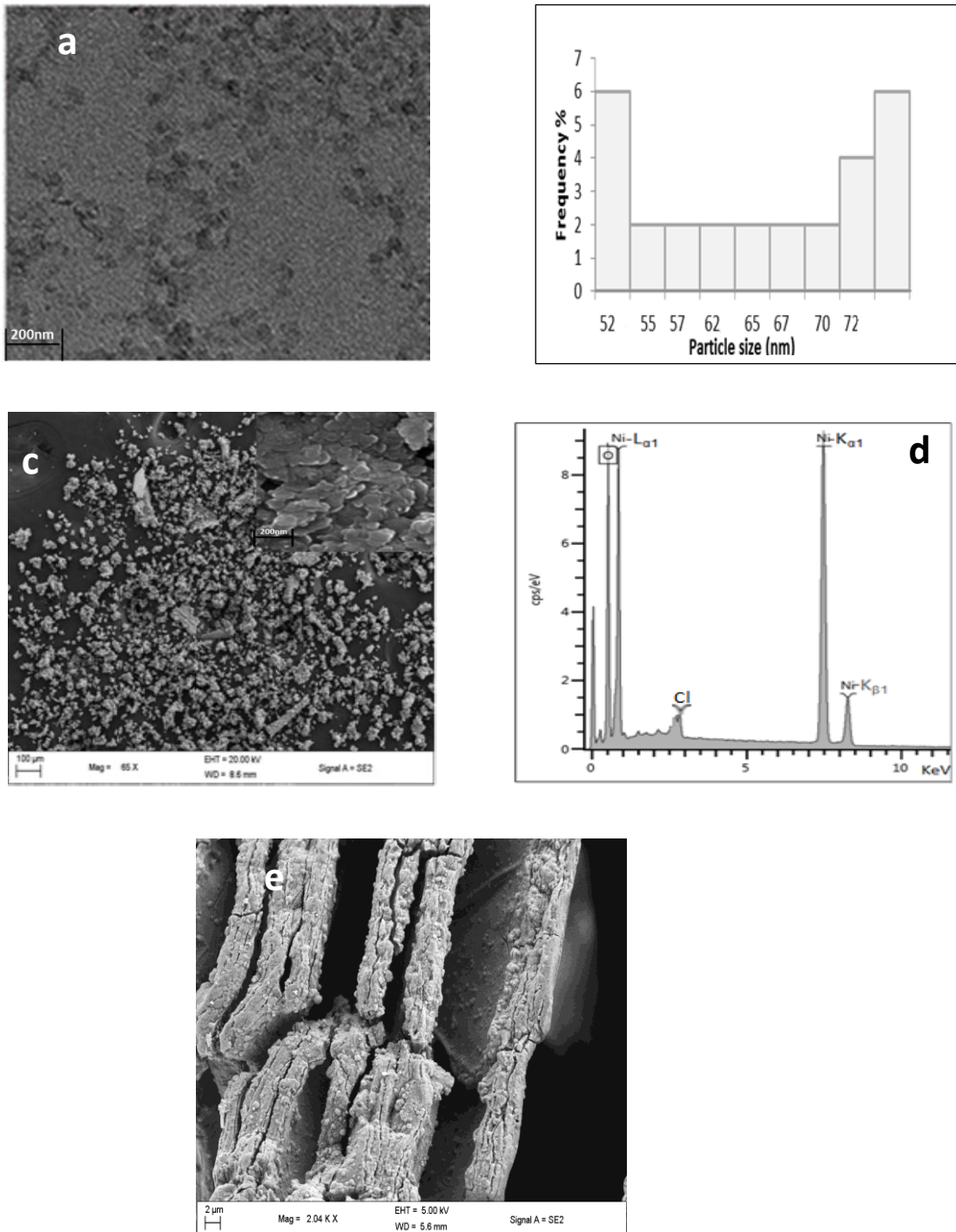
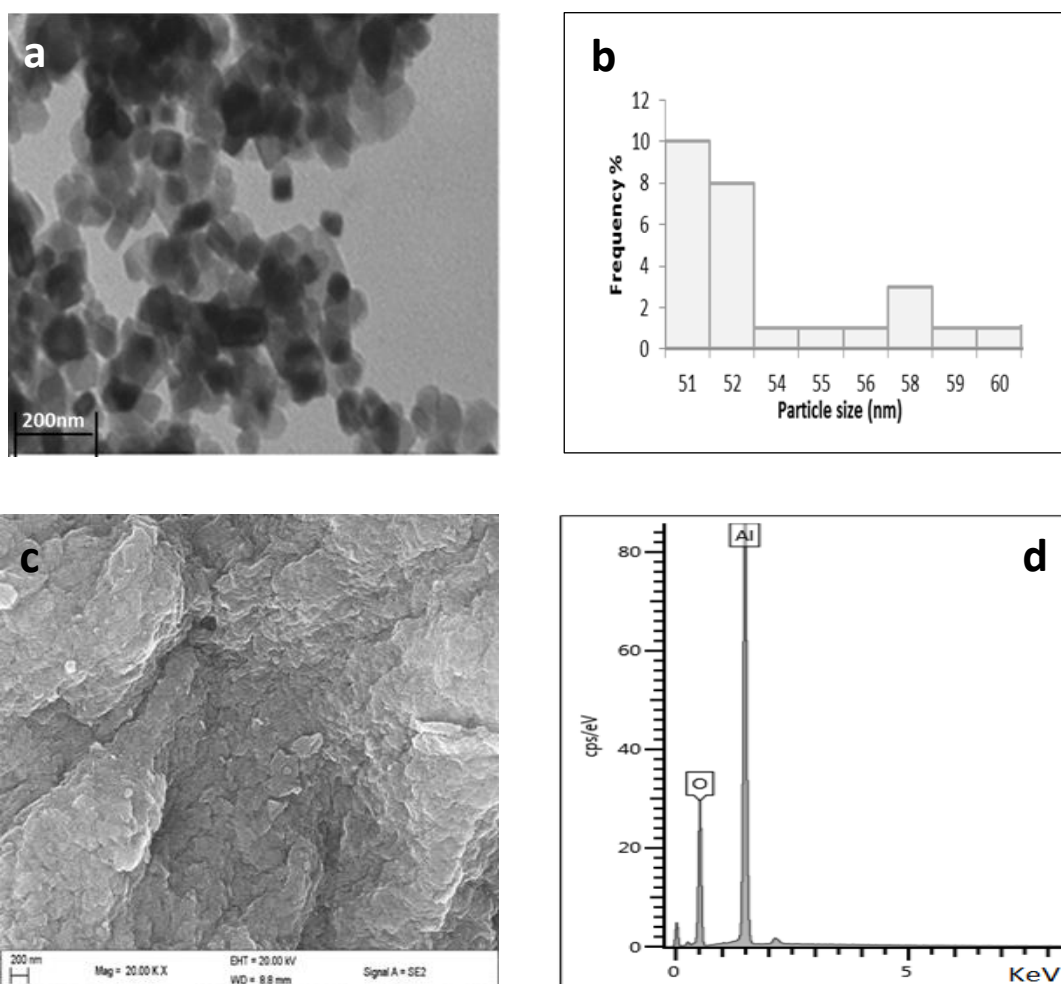


Fig 3.20: (a) TEM image, (b) SDA plot (c) SEM images (insert: at nanoscale), (d) EDX spectrum of Ni(OH)₂ NPs and (e) SEM image of GQDs-Ni(OH)₂ NC.

3.6.3.3 Analysis of Al(OH)₃ NPs

A TEM image of aluminium hydroxide NPs is shown in Fig 3.21a, the nanoparticles display a polygon-like morphology with an average size diameter of 53 nm. These particles were determined to be mono-dispersed according to the standard deviation of 6.92 (Fig 3.21b). The SEM image in Fig 3.21c shows the of Al(OH)₃ NPs morphology as clustered micro-platelets. The elemental composition obtained from the EDX analysis (Fig 3.21d) showed the aluminium and oxygen signal as expected, suggesting high purity of the compound as no Al(OH)₃ NPs impurities were detected. A SEM image of the GQDs-Al(OH)₃NC is shown in Fig 3.21e displaying fragmented graphene quantum dot sheets decorated with Al(OH)₃ NPs.



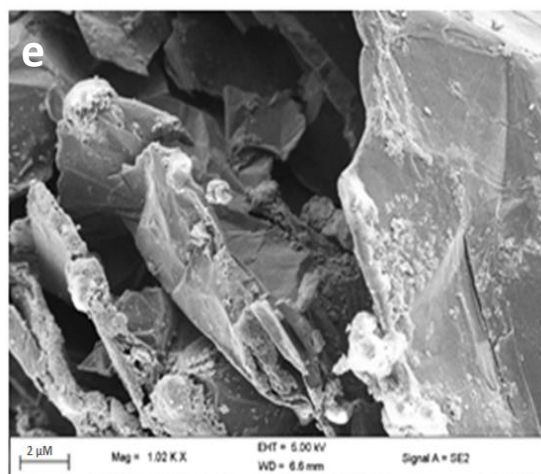


Fig 3.21: (a) TEM image, (b) SDA plot, (c) SEM image, (d) EDX spectrum of $\text{Al}(\text{OH})_3$ NPs and (e) SEM image of GQDs- $\text{Al}(\text{OH})_3$ NC.

3.6.3.4 Analysis of $\text{Mn}(\text{OH})_2$ NPs

The TEM image of $\text{Mn}(\text{OH})_2$ NPs in Fig 3.22a display the NPs as aggregated spherical particles with an average size diameter of approximately 60 nm. These spheres were found to be monodispersed according to the standard deviation of 6.36 (Fig 3.22b). The SEM image in Fig 3.22c showed a surface morphology that is characterised by rough spheres. The elemental composition of $\text{Mn}(\text{OH})_2$ obtained from EDX analysis shown in Fig 3.22e, showed oxygen and manganese elemental signals at L and K energy shells, detected at 0.550 ($L_{\alpha 1}$), 5.910 ($K_{\alpha 1}$) and 6.500 ($K_{\beta 1}$)⁵³ for Mn. The $\text{Mn}(\text{OH})_2$ NPs showed high purity level as no impurities were detected. The SEM image of GQDs- $\text{Mn}(\text{OH})_2$ NC in Fig 3.22d displayed graphene quantum dot sheets uniformly decorated with microcrystalline shaped $\text{Mn}(\text{OH})_2$ NPs.

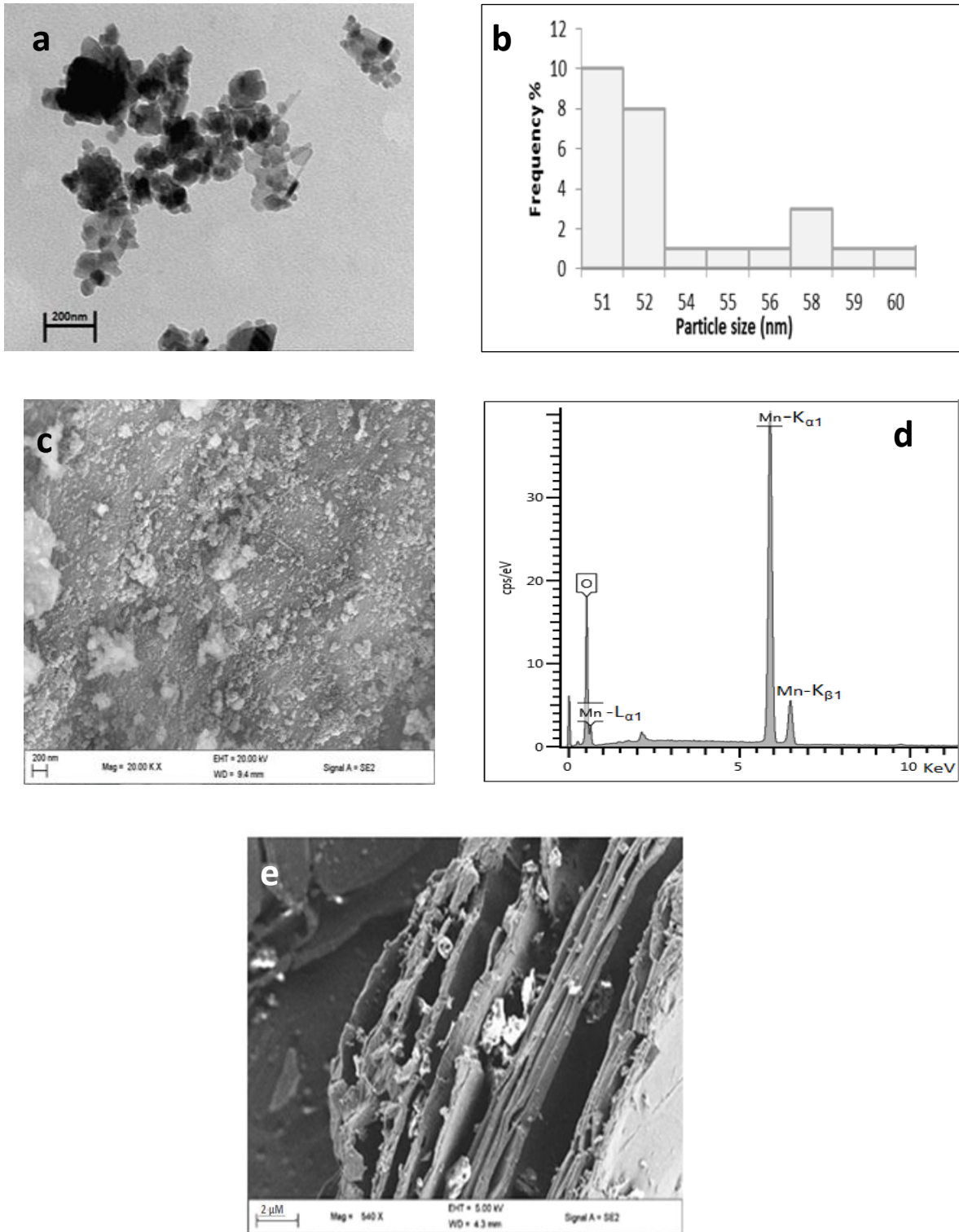


Fig 3.22: (a) TEM image, (b) SDA plot, (c) SEM image, (d) EDX spectrum of Mn(OH)₂ NPs and (e) SEM image of GQDs-Mn(OH)₂ NC.

3.7 Effects of particle size in catalytic behaviour

The activity of a catalyst is relative to its effective surface area exposed. Considerable efforts are often made to maximize the surface area per unit mass of catalytic material and an example of this is the use of nanomaterials.⁵⁴ Nanomaterials often improve the properties of the catalytic material due to their small particle size. Table 3.1 shows the average particle size of MO and MOH nanoparticles. The MOH NPs showed smaller nanoparticle sizes in the following pattern: $\text{Cu}(\text{OH})_2 < \text{Ni}(\text{OH})_2 < \text{Al}(\text{OH})_3 < \text{Mn}(\text{OH})_2$ compared to MO NPs: $\text{Cu}_2\text{O} < \text{NiO} < \text{Al}_2\text{O}_3 < \text{MnO}_2$. The catalytic efficiency of a sensing material is increased with its decreasing particle size.⁵⁴ Therefore it is expected that the MOH NPs in the pattern mentioned above will be better catalysts compared to their corresponding MO NPs.

Table 3.1: Particle sizes of MO and MOH nanoparticles.

Nanoparticles	Average diameter size (nm)
Cu_2O	31
$\text{Cu}(\text{OH})_2$	20
NiO	55
$\text{Ni}(\text{OH})_2$	50
Al_2O_3	60
$\text{Al}(\text{OH})_3$	53
MnO_2	70
$\text{Mn}(\text{OH})_2$	60

3.8 Thermal gravimetric analysis (TGA) of nanomaterials

3.8.1 TGA profile of graphene NPs

Thermal gravimetric analysis was done in order to determine the nanoparticles thermal stability in N₂ atmosphere from 0 °C to 900 °C. Fig 3.23 shows the thermal stability of the graphene based nanoparticles. Gr displayed a 1.33 % weight loss from 0 to 900 °C due to the pyrolysis of the carbon skeleton⁵⁵ (Fig 3.23a). The small amount of weight lost due to minimal functional groups on graphite surface further confirms the crystalline nature of Gr shown in the XRD pattern. The GO TGA profile (Fig 3.23b) showed the highest weight loss which occurred in two stages. The initial weight loss of 5.5% observed at 100 °C was due to the evaporation of adsorbed water and the mass loss of 39.5% between 280 °C and 450 °C was attributed to the decomposition of oxygen containing functional groups on the graphene lattice.⁵⁶ The GQDs (Fig 3.23c) showed that they were more stable than GO as a result of the decreased amount of oxygen containing functional groups lost⁵⁶. The TGA profile of the GQDs displayed an overall weight loss of 18.85% which also occurred in two stages. The initial weight loss occurred between 300 °C and 470 °C due to the decomposition of oxygen containing functional groups.^{57,58} The other mass loss occurred between 750 °C and 900 °C as a result of the pyrolysis of graphene carbon skeleton. Furthermore, the stability of GQDs was confirmed by XRD analysis as it was determined to be semi-crystalline due to the reduction of some oxygen containing functional groups compared to the fully oxidised amorphous GO.

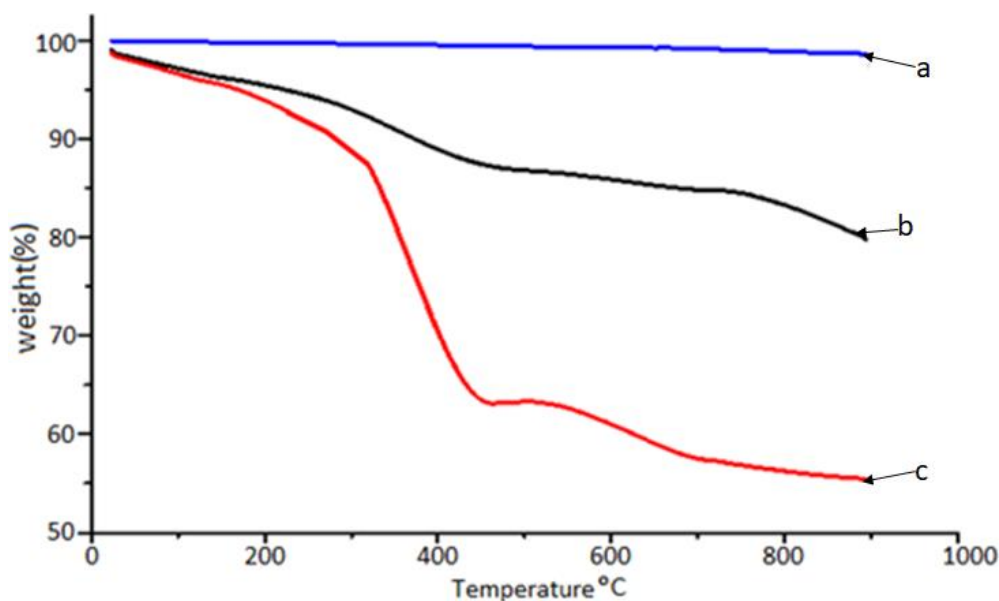


Fig 3.23: TGA profile of (a) Gr, (b) GO and (c) GQDs.

3.8.2 TGA profile of metal nanoparticles

3.8.2.1 TGA profile of copper NPs.

The thermal profile of Cu_2O NPs is shown in Fig 3.24a, an overall mass loss of 38% occurred between 0 °C and 210 °C. This loss was that of water adsorbed on the surface of the NPs.⁵⁹ For the $\text{Cu}(\text{OH})_2$ NPs (Fig 3.24b) an overall mass loss of 32% was observed. The initial mass loss of 24% between 0 °C and 200 °C was attributed to the loss of water adsorbed on the lattice of the NPs and the other weight loss of 8 % between 300 °C to 400 °C was due to the decomposition of the $\text{Cu}(\text{OH})_2$ NPs.⁶⁰ The copper oxide compared to $\text{Cu}(\text{OH})_2$ nanoparticles exhibited better thermal stability as little or no further weight loss occurred beyond 350 °C, this is as a result of its high purity and big nanoparticles as confirmed by EDX and TEM respectively.⁶¹

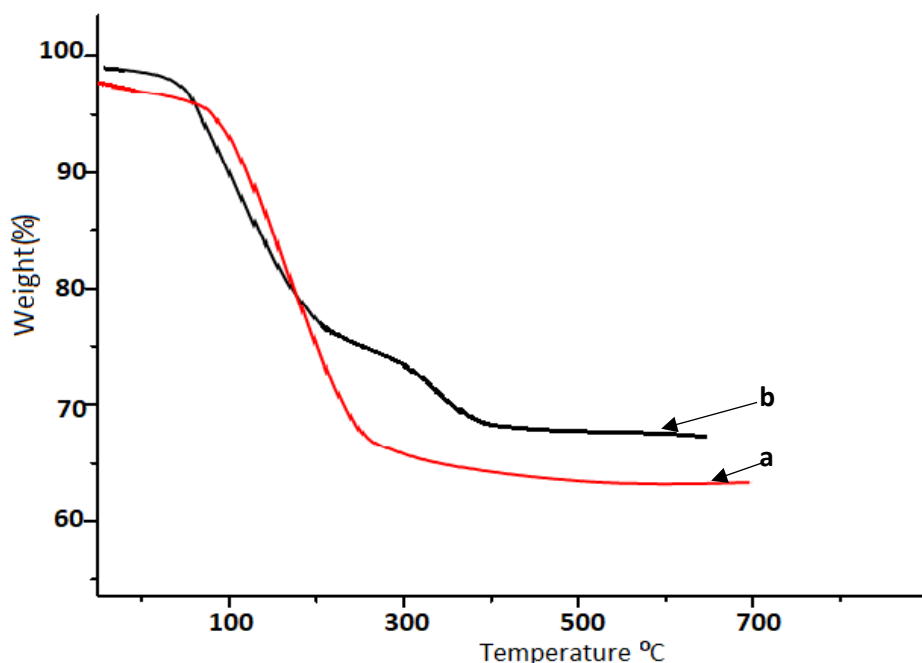


Fig 3.24: TGA profile of (a) Cu_2O and (b) $\text{Cu}(\text{OH})_2$ NPs.

3.8.2.2 TGA profile of nickel NPs

The TGA profile of NiO NPs is shown in Fig 3.25a, an overall weight loss of 15 % is observed. The initial mass loss of 7.7 % between 0 °C and 100 °C was due to the loss of water adsorbed on the surface of the NPs. The other weight loss of 7.3 % between 100 °C and 300 °C was ascribed to the loss of water associated with the decomposition of the $\text{Ni}(\text{OH})_2$ to give NiO NPs.⁶² Fig 3.25b shows the weight loss profile of nickel hydroxide NPs. An initial weight of 12.5% between 60 °C and 80 °C was attributed to the water adsorbed on the surface of the NPs. Another weight loss of 12.5 % between 150 °C and 210 °C was due to dehydration and dihydroxylation of the NPs. Another mass loss of 4.5 % occurring between 210 and 450 °C is the result of $\text{Ni}(\text{OH})_2$ NPs decomposition.⁶³ NiO NPs demonstrated better thermal stability compared to $\text{Ni}(\text{OH})_2$ NPs. This is confirmed by its high purity exhibited by EDX. NiO NPs high crystalline nature shown by XRD analysis.⁶⁴

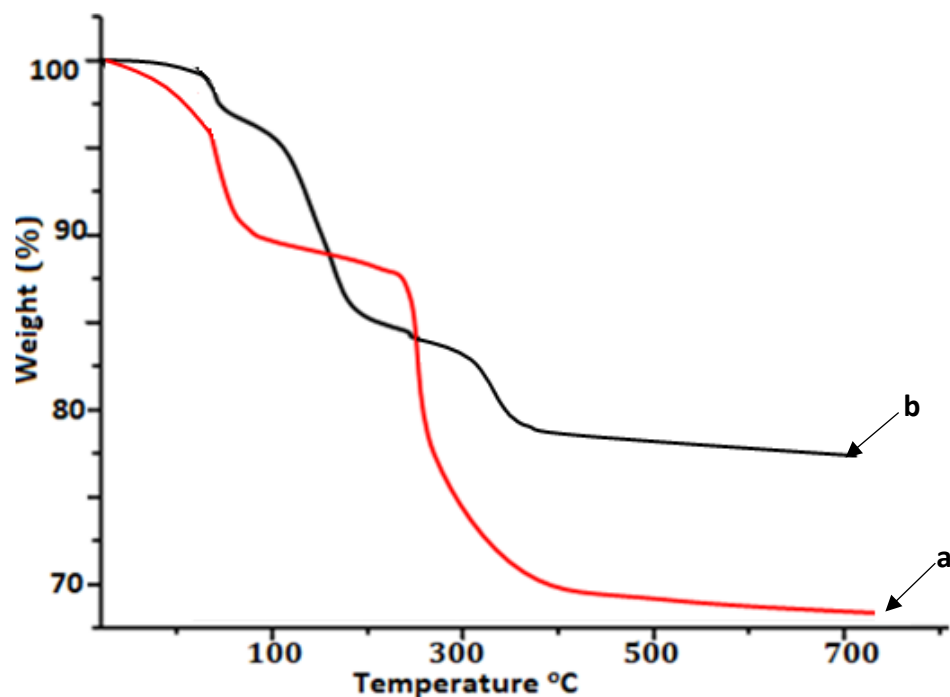


Fig 3.25: TGA profile of (a) NiO and (b) Ni(OH)₂ NPs.

3.8.2.3 TGA profile of aluminium NPs

The thermal stability profile of Al₂O₃ NPs is shown in Fig 3.26a with an overall weight loss of 62 %. The initial mass loss of 5 % occurred between 0 °C and 95 °C was attributed to the loss of water adsorbed on the lattice of NPs. The next weight loss of 37 % occurred between 150 °C and 300 °C was due to the decomposition of the precursor Al(NO₃)₃.9H₂O and its coordinated water.⁶⁵ The last weight loss of 20 % occurred from 310 °C to 520 °C as a result of the decomposition of the nanoparticles.⁴⁶ Fig 3.26b shows the weight loss profile of aluminium hydroxide NPs occurring over two stages. The initial weight loss of 10 % occurred from 0 °C to 95 °C due to the loss of water and the other weight loss of 14 % occurred between 150 °C and 450 °C as a result of the decomposition of Al(OH)₃ nanoparticles.⁶⁶ The Al(OH)₃ NPs are less thermally stable compared to Al₂O₃ NPs. The thermal instability is due to their smaller nanoparticle sizes shown in TEM analysis.⁶⁷

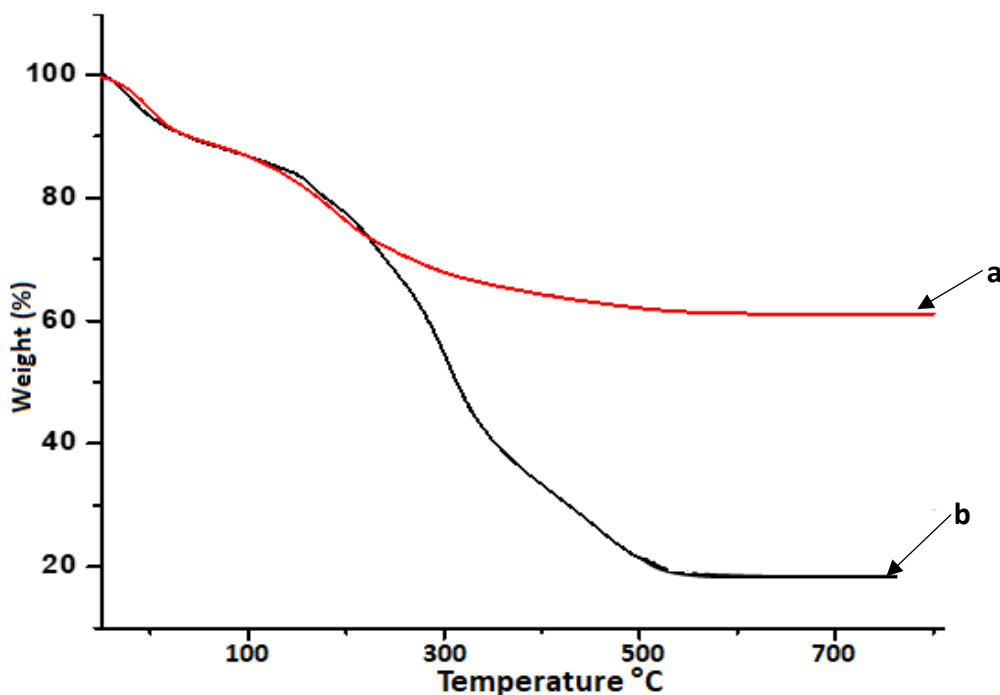


Fig 3.26: TGA profile of (a) Al₂O₃ and (b) Al(OH)₃ NPs.

3.8.2.4 TGA profile of manganese NPs

The TGA profile of the MnO₂ NPs is shown in Fig 3.27a with an overall weight loss of 17.5%. The weight loss occurred in two stages, with the initial mass loss of 9% occurring between 200 °C and 420 °C due to the loss of water adsorbed on the surface of the NPs. The other mass of 8.5% occurred between 560 °C and 640 °C was due to the decomposition of the nanoparticles.⁶⁸ The thermal stability profile of Mn(OH)₂ NPs is shown in Fig 3.27b displaying an overall weight loss of 8.5%. This weight loss occurred between 0 °C and 220 °C attributed to the loss of water adsorbed on the NPs surface.⁶⁹ MnO₂ NPs possess better thermal stability compared to their corresponding hydroxide NPs. This is attributed to their high purity and big nanoparticle sizes demonstrated in EDX and TEM analysis respectively.⁷⁰

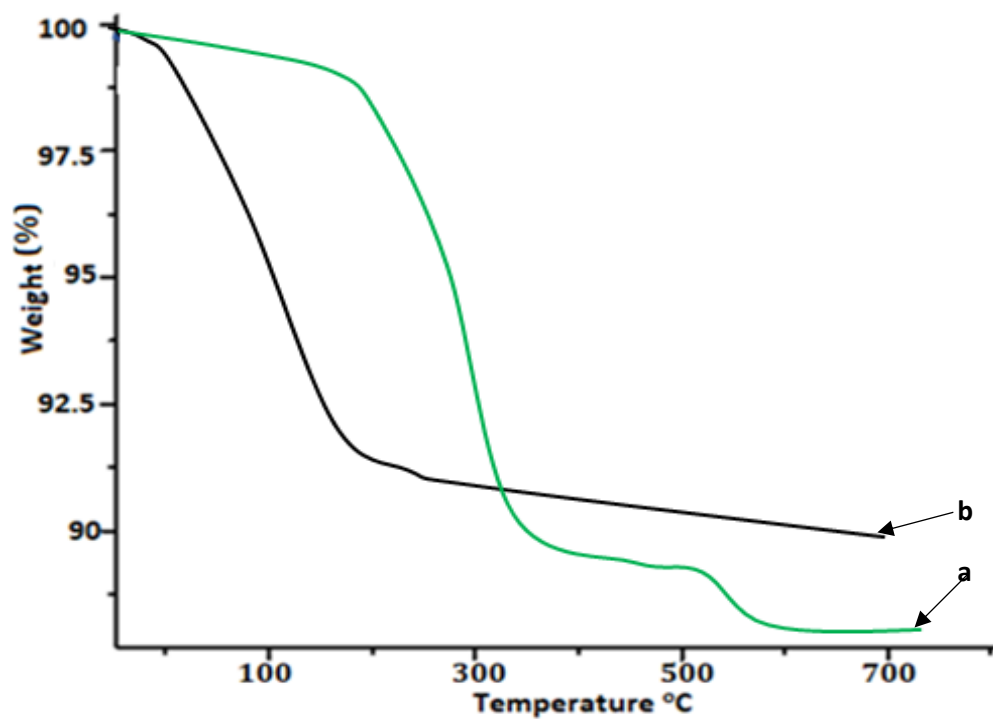


Fig 3.27: TGA profile of (a) MnO_2 and (b) $\text{Mn}(\text{OH})_2$ NPs.

3.9 References

- (1) Krane, N. *Growth Lakel.* **1993**, 4 (4), 1–5.
- (2) Van Chuyen P. *Phys. Chem* **2016**, 16, 24.
- (3) Fernández-garcia, M. J. A.; Rodriguez. *Nanomater. Inorg. Bioinorg. Perspect.* **2007**, 60.
- (4) Qian, Y.; Ye, F.; Xu, J.; Le, Z. G. *Int. J. Electrochem. Sci.* **2012**, 7 (10), 10063–10073.
- (5) Rahdar, A.; M.Aliahmad; Y.Azizi. *J. nanostructures* **2015**, 5, 145–151.
- (6) Farahmandjou, M.; Golabiyan, N. *Trans. Phenom. Nano Micro Scales* **2015**, 3 (2), 100–105.
- (7) Gokulakrishnan, K. *Res. J. Chem. Environ. Sci.* **2014**, 2, 55–58.
- (8) Ayask, H. K.; Khaki, J. V.; Haddad Sabzevar, M. *J. Ultrafine grained nanostructured Mater.* **2015**, 48 (1), 37–44.
- (9) Zheng, C. H.; Liu, X.; Chen, Z. D.; Wu, Z. F.; Fang, D. L. *J cent. South Univ.* **2014**, 21, 2596–2603.
- (10) Goudarzi, M.; Ghanbari, D.; Salavati-niasari, M. *J. nanostructures* **2015**, 5 (2), 110–115.
- (11) Peng, T.; , Longjun Xu, H. C. *Cent. Eur. J. Chem.* **2010**, 8 (5), 1059–1068.
- (12) Xiao, W.; Zhou, W.; Feng, T.; Zhang, Y.; Liu, H.; Tian, L. *Materials.* **2016**, 9 (9).
- (13) Liu, C. *Mater. Today Commun.* **2016**, 8, 127–133.

- (14) Dong, Y.; Shao, J.; Chen, C.; Li, H.; Wang, R.; Chi, Y.; Lin, X.; Chen, G. *Carbon N. Y.* **2012**, *50* (12), 4738–4743.
- (15) Shahriary, L.; Athawale, A. A. *Int. J. Renew. Energy Environ. Eng.* **2014**, *2* (1), 2348–157.
- (16) Cheng, S.-H.; Weng, T.-M.; Lu, M.-L.; Tan, W.-C.; Chen, J.-Y.; Chen, Y.-F. *Sci. Rep.* **2013**, *3*, 2694.
- (17) Pelayo, E.; Zazueta, A.; López-Delgado, R.; Saucedo, E.; Ruelas, R.; Ayón, A. *J. Phys. Conf. Ser.* **2016**, *773*, 12053.
- (18) Fan, T.; Zeng, W.; Tang, W.; Yuan, C.; Tong, S.; Cai, K.; Liu, Y.; Huang, W.; Min, Y.; Epstein, A. J. *Nanoscale Res. Lett.* **2015**, *10* (1), 55.
- (19) Ishikawa-Ankerhold, H. C.; Ankerhold, R.; Drummen, G. P. C. *Molecules* **2012**, *17* (4), 4047–4132.
- (20) Valeur, B. *Molecular Fluorescence Principles and Applications*; Wiley-VCH Verlag, **2001**; 8.
- (21) Han, W.; Xiao-min, W. *acta physico-chimica Sin.* **2016**, *32* (5), 1267–1272.
- (22) Gipson, K.; Stevens, K.; Brown, P.; Ballato, J. *J. Spectrosc.* **2015**, *2015*, 1–9.
- (23) Khan, Q. A.; Shaur, A.; Khan, T. A.; Joya, Y. F.; Awan, M. S.; Khan, Q. A.; Shaur, A.; Khan, T. A.; Joya, Y. F.; Awan, M. S. *Cogent Chem.* **2017**, *3*, 1–9.
- (24) Li, M.; Ni, W.; Kan, B.; Wan, X.; Zhang, L.; Zhang, Q.; Long, G.; Zuo, Y.; Chen, Y. *Phys. Chem. Chem. Phys.* **2013**, *15* (43), 18973–18978.
- (25) Sobon, G.; Sotor, J.; Jagiello, J.; Kozinski, R.; Zdrojek, M.; Holdynski, M.; Paletko, P.; Boguslawski, J.; Lipinska, L.; Abramski, K. M. *Opt. Express* **2012**, *20* (17), 19463.

- (26) Ho, W.; Tay, Q.; Qi, H.; Huang, Z.; Li, J.; Chen, Z. *Molecules* **2017**, *22* (4), 677.
- (27) Ruiz, E.; Alvarez, S.; Alemany, P.; Evarestov, R. a. *Phys. Rev.* **1997**, *56* (12), 7189–7196.
- (28) Korzhavyi, P. A.; Soroka, I. L.; Isaev, E. I.; Lilja, C.; Johansson, B. *Proc. Natl. Acad. Sci.* **2012**, *109* (3), 686–689.
- (29) Zhang, Y. X.; Huang, M.; Li, F.; Wen, Z. Q. *Int. J. Electrochem. Sci.* **2013**, *8* (6), 8645–8661.
- (30) Adekunle, A. S.; Oyekunle, J. A. O.; Oluwafemi, O. S.; Joshua, A. O.; Makinde, W. O.; Ogunfowokan, A. O.; Eleruja, M. A.; Ebenso, E. E. *Int. J. Electrochem. Sci.* **2014**, *9* (6), 3008–3021.
- (31) Ramesh, T. N.; Taj, A. *Int. J. Sci. Res.* **2014**, *1* (4), 487–494.
- (32) Huang, X.; Chen, Z.; Gao, T.; Huang, Q.; Niu, F.; Qin, L.; Huang, Y. *Energy Technol.* **2013**, *1* (12), 751–756.
- (33) Shirai, T.; Watanabe, H.; Fuji, M.; Takahashi, M. *Annu. Rep. Adv. Ceram. Res. Cent. Nagoya Inst. Technol.* **2009**, *9*, 23–31.
- (34) Djebaili, K.; Mekhalif, Z.; Boumaza, A.; Djelloul, A. *J. Spectrosc.* **2015**, *2015*, 1–16.
- (35) Schroeder, P. *Teach. clay Sci.* **2002**, *11*, 181–206.
- (36) Hem, J. D.; Roberson, C. E. *USGS Water Supply Pap.* **1967**, 1827–55.
- (37) Post, J. E. *Proc. Natl. Acad. Sci. U. S. A.* **1999**, *96* (7), 3447–3454.
- (38) Yan, D.; Li, Y.; Liu, Y.; Zhuo, R.; Wu, Z.; Geng, B.; Wang, J.; Ren, P.; Yan, P.; Geng, Z. *Mater. Lett.* **2014**, *136*, 7–10.

- (39) Hu, C.; Liu, Y.; Yang, Y.; Cui, J.; Huang, Z.; Wang, Y.; Yang, L.; Wang, H.; Xiao, Y.; Rong, J. *J. Mater. Chem. B* **2013**, *1* (1), 39–42.
- (40) Meghana, S.; Kabra, P.; Chakraborty, S.; Padmavathy, N. *RSC Adv.* **2015**, *5* (16), 12293–12299.
- (41) Ba, N.; Zhu, L.; Zhang, G.; Li, J.; Li, H. *Sensors Actuators B Chem.* **2016**, *227*, 142–148.
- (42) Nowsath Rifaya, M.; Theivasanthi, T.; Alagar, M. *Nanosci. Nanotechnol.* **2012**, *2* (5), 134–138.
- (43) Wu, Z.; Huang, X.-L.; Wang, Z.-L.; Xu, J.-J.; Wang, H.-G.; Zhang, X.-B. *Sci. Rep.* **2014**, *4*, 3669.
- (44) Hall, D. S.; Lockwood, D. J.; Bock, C.; MacDougall, B. R. *Proceedings. Math. Phys. Eng. Sci.* **2015**, *471* (2174), 20140792.
- (45) Buongiorno, J.; Venerus, D. C.; Prabhat, N.; McKrell, T.; Townsend, J.; Christianson, R.; Tolmachev, Y. V.; Keblinski, P.; Hu, L. W.; Alvarado, J. L.; Bang, I. C.; Bishnoi, S. W.; Bonetti, M.; Botz, F.; Cecere, A.; Chang, Y.; Chen, G.; Chen, H.; Chung, S. J.; Chyu, M. K.; Das, S. K.; Di Paola, R.; Ding, Y.; Dubois, F.; Dzido, G.; Eapen, J.; Escher, W.; Funfschilling, D.; Galand, Q.; Gao, J.; Gharagozloo, P. E.; Goodson, K. E.; Gutierrez, J. G.; Hong, H.; Horton, M.; Hwang, K. S.; Iorio, C. S.; Jang, S. P.; Jarzebski, A. B.; Jiang, Y.; Jin, L.; Kabelac, S.; Kamath, A.; Kedzierski, M. A.; Kieng, L. G.; Kim, C.; Kim, J. H.; Kim, S.; Lee, S. H.; Leong, K. C.; Manna, I.; Michel, B.; Ni, R.; Patel, H. E.; Philip, J.; Poulikakos, D.; Reynaud, C.; Savino, R.; Singh, P. K.; Song, P.; Sundararajan, T.; Timofeeva, E.; Tritcak, T.; Turanov, A. N.; Van Vaerenbergh, S.; Wen, D.; Witharana, S.; Yang, C.; Yeh, W. H.; Zhao, X. Z.; Zhou, S. Q. *J. Appl. Phys.* **2009**, *106* (9), 94312.

- (46) Tabatabaee, M.; Saberi, N. *Int. J. Bio-Inorg. Hybd. Nanomat* **2012**, *1* (4), 253–256.
- (47) Wang, C. J.; O'Hare, D. *J. Mater. Chem.* **2012**, *22* (43), 23064.
- (48) Li, F.; Xing, Y.; Huang, M.; Li, K. L.; Yu, T. T.; Zhang, Y. X.; Losic, D. *J. Mater. Chem. A* **2015**, *3* (15), 7855–7861.
- (49) Liu, J.-S.; Hu, Y.; Chuang, T.-L.; Huang, C.-L. *Thin Solid Films* **2013**, *544*, 186–190.
- (50) Lok, K. P.; Ober, C. K. *Can. J. Chem.* **1985**, *63* (1), 209–216.
- (51) Dinger, D. *Practical Pointers for Ceramists*, **2010**.
- (52) Tran, T. H.; Nguyen, V. T. *Int. Sch. Res. Not.* **2014**, *2014*, 1–14.
- (53) X-rays, C. *Uranium 100*, 14001.
- (54) Anderson, J. R. *Sci. Prog., Oxf.* **1985**, *69*, 461–484.
- (55) Muthoosamy, K.; Bai, R. G.; Abubakar, I. B.; Sudheer, S. M.; Lim, H. N.; Loh, H.-S.; Huang, N. M.; Chia, C. H.; Manickam, S. *Int. J. Nanomedicine* **2015**, *10* (1), 1505–1519.
- (56) Wu, T.; Wang, X.; Qiu, H.; Gao, J.; Wang, W.; Liu, Y. *J. Mater. Chem.* **2012**, *22* (11), 4772–4779.
- (57) Cui, P.; Lee, J.; Hwang, E.; Lee, H. *Chem. Commun.* **2011**, *47* (45), 12370.
- (58) Jana, M.; Saha, S.; Khanra, P.; Murmu, N. C.; Srivastava, S. K.; Kuila, T.; Lee, J. H. *Mater. Sci. Eng. B* **2014**, *186*, 33–40.
- (59) Eskandari, A.; Sangpour, P.; Vaezi, M. R. *Mater. Chem. Phys.* **2014**, *147* (3), 1204–1209.
- (60) Mosaddegh, E.; Hassankhani, A.; Karimi-Maleh, H. *Mater. Sci. Eng. C* **2015**, *46*, 264–269.

- (61) Topnani, N.; Kushwaha, S.; Athar, T. *Int. J. Green Nanotechnol. Mater. Sci. Eng.* **2010**, *1* (2), 67–73.
- (62) El-Kemary, M.; Nagy, N.; El-Mehasseb, I. *Mater. Sci. Semicond. Process.* **2013**, *16* (6), 1747–1752.
- (63) Kavitha, N.; Anantha Lakshmi, P. V. *J. Saudi Chem. Soc.* **2015**, *21*, S457–S466.
- (64) Nome, S. *Communication* **2002**, 1–2.
- (65) Fatima, K.; Nosheen, S.; Azhar, M. *Synthesis.* **2009**, *157*, 1–7.
- (66) Strekopytov, S.; Exley, C. *Polyhedron* **2006**, *25* (8), 1707–1713.
- (67) Molinari, A.; Lonardelli, I.; Demetrio, K.; Menapace, C. *J. Mater. Sci.* **2010**, *45* (24), 6739–6746.
- (68) Kumari, V.; Tripathi, B.; Dixit, A. *J. Nano Energy Power Res.* **2014**, *315*, 1–9.
- (69) Zhang, X.; Qian, Y.; Zhu, Y.; Tang, K. *Nanoscale* **2014**, *6* (3), 1725–1731.
- (70) Sagadevan S. *Cit. Sagad. S J Mater. Sci Eng* **2015**, *4* (3), 3–5.

4. Electrode fabrication and electrocatalysis

4.1 Electrode fabrication

The graphene quantum dot paste electrode (GQDPE) was fabricated using a well-known procedure.¹ The graphene paste mixture was prepared by mixing 0.5 g of graphene quantum dots with 180 μL of paraffin oil using a mortar and a pestle. The mixture was homogenized and then packed into an auto-pipette tip. Electrical contact was made by pushing a copper wire coated with silver paste through the pipette into the mixture. The surface of the electrode was replenished by pushing excess paste out of the tip and polishing the surface on paper. This fabrication method was used to make GQD-MO and GQD-MOH electrodes. The only difference was a homogenized mixture of GQD-MO or GQD-MOH was used instead of the GQDs alone. The GQDs-MO or GQDs-MOH nanocomposites were prepared by adding 1 mL of GQDs to 1 mL of MO/MOH in 2 mL of DMF and sonicating for 2 h.

Before each experiment the GCE was cleaned by gentle polishing in aqueous slurry of alumina nanopowder on a silicon carbide-emery paper. The electrode was then rinsed in double distilled water to remove residual alumina particles and dried at room temperature.² The GCE was modified with the nanocomposites using a drop-dry method. A 20 μL nanocomposite suspension was dropped on the electrode surface and dried for 15 min at room temperature to obtain GCE/GQDs-MO or GCE/GQDs-MOH working electrodes.

4.1.1 Electrode characterisation

The modified and unmodified electrodes were characterised using cyclic voltammetry (CV) and ferricyanide ($[\text{Fe}(\text{CN})_6]^{3-}/[\text{Fe}(\text{CN})_6]^{4-}$) as the redox probe. Fig 4.1a shows the CV response of the GQDPE towards the probe. Two redox peaks were observed, an oxidation peak (E_{pa}) at 0.10 V and reduction peak (E_{pc}) at -0.30 V. The peak-to-peak separation (ΔE) of this couple was determined to be 107 mV, indicating a reversible process. A ΔE value of a reversible process is theoretically ≈ 59 mV.³ The increased ΔE is attributed to a significant uncompensated resistance resulting in an ohmic drop.

On the bare GCE (Fig 4.1b (i)) ΔE was found to be 75 mV, this increased ΔE could be a result of charge transfer resistance between the electrode surface and redox probe.⁴ The current density of the GQDPE was higher than that of the bare GCE confirming that the GQDPE has better electrical conductivity than the GCE.

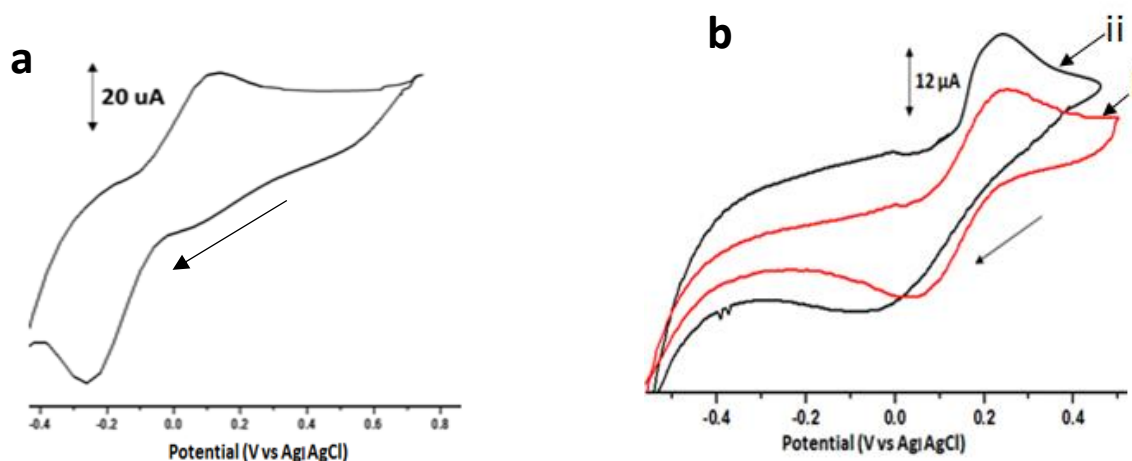


Fig 4.1: Cyclic voltammograms of (a) GQDPE (b) (i) bare and (ii) GQDs/GCE.

Upon GCE modification with GQDs (Fig 4.1 b(ii)) ΔE was determined to be 100 mV. The increased ΔE indicates an electron transfer barrier experienced by the modified electrodes resulting in slower electron transfer rates compared to the bare electrode.³ The modified electrode also showed slightly lower redox potentials and increased peak currents suggesting good conductivity.⁵ Fig 4.2 shows the cyclic voltammogram responses of the GQDs/GCE [Fig 4.2 a(i)] modified with Cu_2O [Fig 4.2 a(ii)] and $\text{Cu}(\text{OH})_2$ [Fig 4.2 a(iii)] nanoparticles. The ΔE of the modified electrodes were determined to be 100 mV, 103 mV and 104 mV respectively showing no significant difference in redox peak potential. Higher current density was observed for the $\text{Cu}(\text{OH})_2$ based electrode, this is attributed to $\text{Cu}(\text{OH})_2$ nanoparticles small particle sizes compared Cu_2O nanoparticles. The small particle size increases the electroactive surface area of the nanoparticles resulting in high sensitivity and electrical conductivity of the electrode.

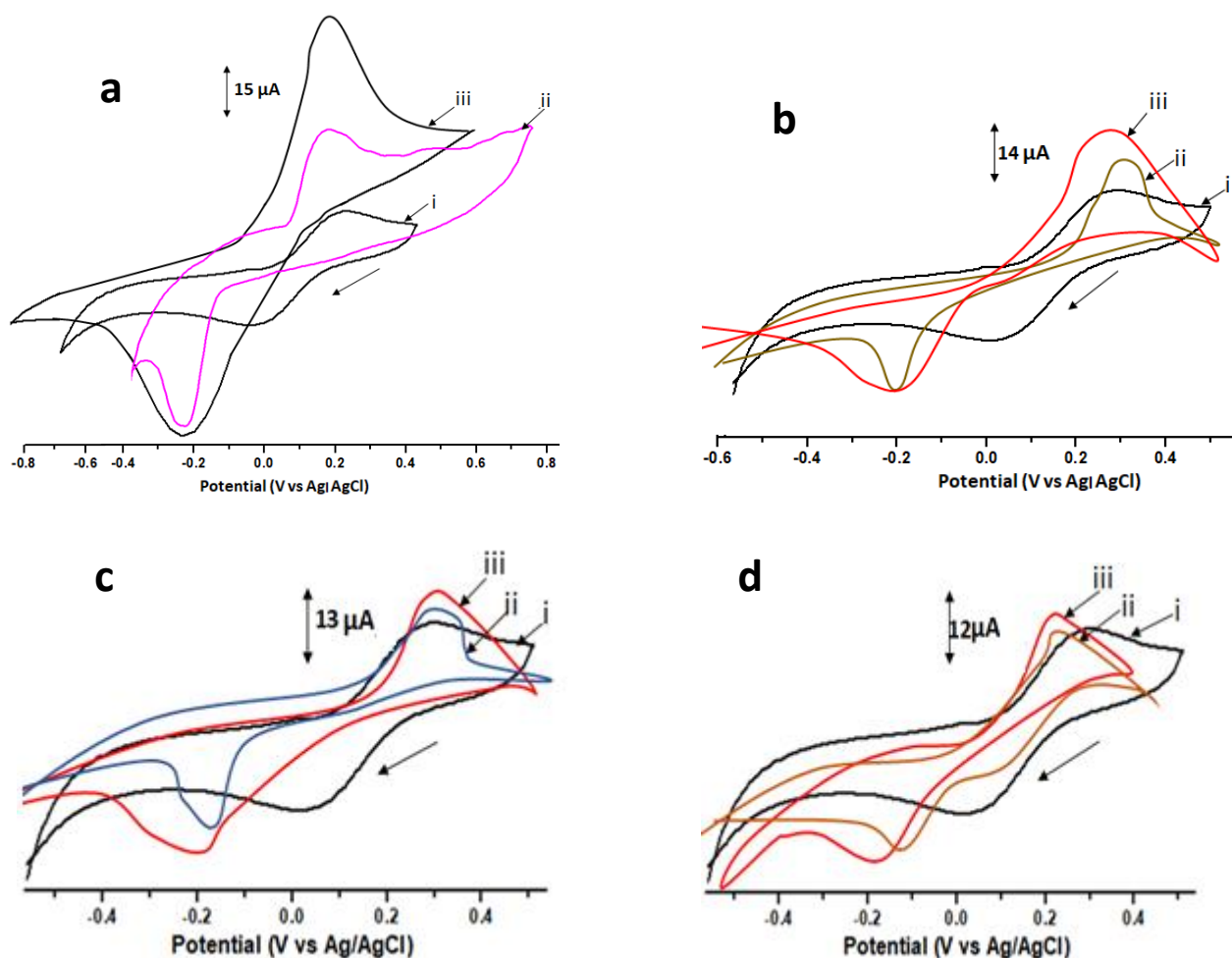


Fig 4.2: Cyclic voltammograms of (a) (i) GQDs/GCE (ii) GQDs/Cu₂O/GCE (iii) GQDs/Cu(OH)₂/GCE, (b) (i) GQDs/GCE (ii) GQDs/NiO/GCE (iii) GQDs/Ni(OH)₂/GCE, (c) (i) GQDs/GCE (ii) GQDs/Al₂O₃/GCE (iii) GQDs/Al(OH)₃/GCE and (d) (i) GQDs/GCE (ii) GQDs/MnO₂/GCE (iii) GQDs/Mn(OH)₂/GCE in 5 mM [Fe(CN)₆]³⁻/[Fe(CN)₆]⁴⁻ containing 0.1 M KCl solution. Scan rate = 100 mV.s⁻¹.

The cyclic voltammograms of GQDs/GCE in Fig 4.2b (i), GQDs/NiO/GCE [Fig 4.2b (ii)] and GQDs/Ni(OH)₂/GCE [Fig 4.2b (iii)] displayed a reversible process with ΔE determined to be 100 mV, 103 mV and 104 mV respectively. Although no significant difference in redox peak potential was observed, the Ni(OH)₂ modified electrode showed higher redox peak currents compared to NiO modified electrode. This is as a result of small particle sizes of Ni(OH)₂ NPs which increased the

electroactive surface area leading to an increased current density. This suggests that Ni(OH)₂ nanoparticles can increase the electrode transfer between the electrode surface and redox probe better than NiO nanoparticles. Fig 4.2c shows the cyclic voltammograms of GQDs/GCE [Fig 4.2c (i)], modified with Al₂O₃ [Fig 4.2c (ii)] and Al(OH)₃ [Fig 4.2c (iii)] nanoparticles. The modified electrodes ΔE was determined to be 100 mV, 103 mV and 104 mV respectively. The Al(OH)₃ showed high redox peak currents compared to Al₂O₃ modified electrode, this was also attributed to small particle sizes of Al(OH)₃ nanoparticles. The small particle sizes increased the electroactive surface area of the nanoparticles resulting in higher electrical conductivity. Fig 4.2d shows the cyclic voltammograms responses of GQDs/GCE [Fig 4.2d (i)] modified with MnO₂ [Fig 4.2d (ii)] and Mn(OH)₂ [Fig 4.2d (iii)] nanoparticles. The ΔE of the modified electrodes were determined to be 100 mV, 103 mV and 104 mV displaying no major difference in redox peak potential. The Mn(OH)₂ modified electrode showed higher redox peak currents as a result of small particle sizes. The small particle sizes increases the electroactive surface area of the nanoparticles resulting in higher electrical conductivity. The GQDPE/MO and GQDPE/MOH modified electrodes showed no response for the redox probe. This could have been due to the clogging of the electrode surface⁶ and/or the use of a non-conductive paraffin oil as binder.⁷

The electroactive surface area (A) of the modified electrodes were determined using the Randles-Sevcik equation⁸, equation 4.1, as shown in Table 4.1

$$I_p = 2.69 \times 10^5 \times A \times D^{1/2} \times n^{3/2} \times \nu^{1/2} C \quad (4.1)$$

where I_p is the peak current in A, A is the surface area in cm², D is the diffusion coefficient in cm² s⁻¹, n is the number of electrons transferred in the redox reaction and ν is the scan rate (V s⁻¹). The electroactive surface area of the GQDPE was determined to be 0.0714 cm² and 0.034 cm² for the bare GCE. The large electroactive surface area of GQDPE is attributed to the small particle sizes of the

nanoparticles which increased the rate of electron transfer indicated by the high redox peak currents observed on the cyclic voltammogram responses of the electrodes.⁹

Table 4.1: The electroactive surface area and ΔE values of the modified electrodes

Electrode	Electroactive surface area (cm ²)	ΔE (mV)
GQDPE	0.0714	107
Bare GCE	0.034	75
GQDs/GCE	0.036	100
GQDs/Cu(OH) ₂ /GCE	0.040	104
GQDs/Ni(OH) ₂ /GCE	0.038	104
GQDs/Al(OH) ₃ /GCE	0.037	104
GQDs/Mn(OH) ₂ /GCE	0.036	104
GQDs/Cu ₂ O/GCE	0.038	103
GQDs/NiO/GCE	0.037	103
GQDs/Al ₂ O ₃ /GCE	0.036	103
GQDs/MnO ₂ /GCE	0.035	103

Generally the modified electrodes showed similar electroactive surface areas with an average area of 0.040 cm². The GQDs/Cu(OH)₂/GCE had the largest electroactive surface area of 0.040 cm² compared to 0.037 cm² of GQDs/Cu₂O/GCE, this is another reason of the high electrical conductivity and high current densities demonstrated by this electrode. The large surface area is attributed to the small particle size of the Cu(OH)₂ NPs compared to Cu₂O NPs. The rest of the electrodes with their respective electroactive surface areas and ΔE values are shown in Table 4.1. The A values show that MOH based electrodes have a larger surface area compared to the MO based electrodes. The larger the surface area of an electrode the more sensitivity it is expected to be towards an analyte.

4.2 Electrocatalysis

4.2.1 Electrochemical behaviour of methyl parathion (MP) on GQDPE

The electrochemical behaviour of MP was assessed on GQDPE, Fig 4.3a shows the CV response of GQDPE in a 0.1 M phosphate buffer solution (PBS) in the absence of MP in which no redox peaks are observed. Fig 4.3b shows the CV response of GQDPE in the presence of MP where a pair of well-defined redox peaks were observed displaying E_{pa} at -0.41 V and E_{pc} at -0.24 V.

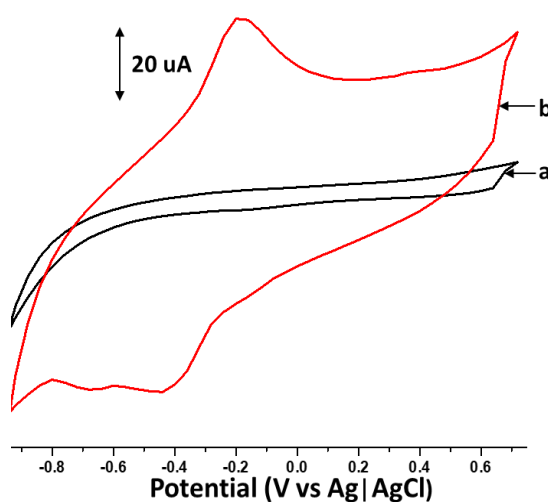
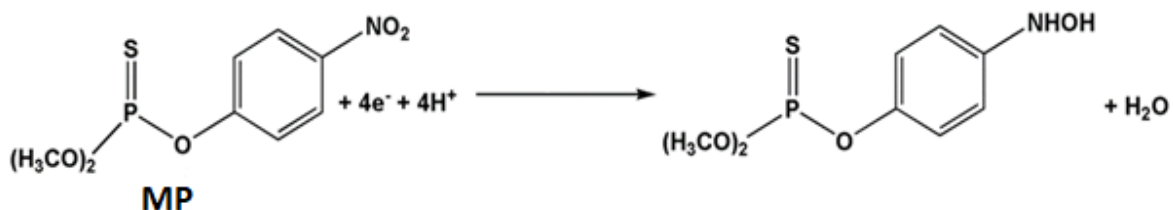
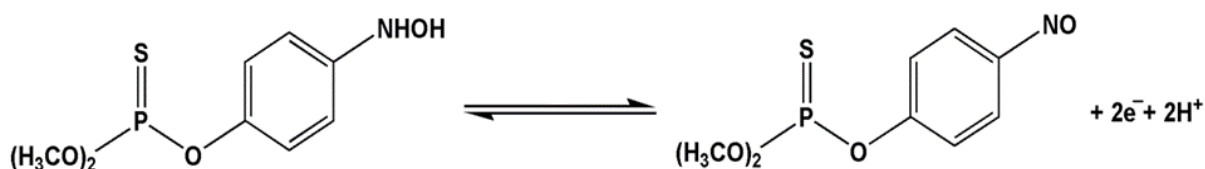


Fig 4.3: Cyclic voltammogram of GQDPE in 0.1 M PBS in the (a) absence and (b) presence of MP. Scan rate = $100 \text{ mV}\cdot\text{s}^{-1}$.

The ΔE was determined to be 85 mV and the current ratio was found to be 1.03 which proves the process as reversible. This reversible process is attributed to a two-electron transfer process, where the hydroxylamine (NHOH) group in MP is oxidised to a nitro (NO) group as shown in Scheme 4.1, reaction 4.2.



Reaction 4.1



Reaction 4.2

Scheme 4.1: The reduction (4.1) and oxidation (4.2) reaction of MP.⁵

An irreversible reduction peak at $E_{pc} = -0.66$ V was also observed in the potential range of -1.0 V to 1.0 V. This irreversible reduction peak corresponds to the reduction of the $-\text{NO}_2$ group in MP to NHOH group shown in reaction 4.1. These results suggest that MP shows high current response on the GQDPE in PBS as a result of the high surface area of GQDPE which favours the adsorption and reduction of methyl parathion.

4.2.1.1 Influence of scan rate on MP electrocatalysis

Fig 4.4a shows the influence of scan rate on the MP redox peaks, the redox peak currents were enhanced by the increase in scan rate indicating a diffusion controlled electrocatalytic process.³ The redox peak potentials of the redox peaks did not change with increasing scan rate and the I_a/I_c ratio was determined to approximately 1. The linear proportional relationship of I_{pa} and I_{pc} to the square root of the scan rate shown in Fig 4.4b also suggests a diffusion controlled process.¹⁰ A logarithm plot of anodic/cathodic current vs the logarithm of the scan rate (Fig 4.4c) revealed a linear relationship with a slope of 0.49.

This value is within 0.5 and 1.0 which are theoretical values for diffusion-controlled and adsorption-controlled processes respectively.¹¹ This information suggests that the overall rate of the reaction is determined by diffusion and adsorption and that an increase in electron transfer does not influence the overall reaction rate.

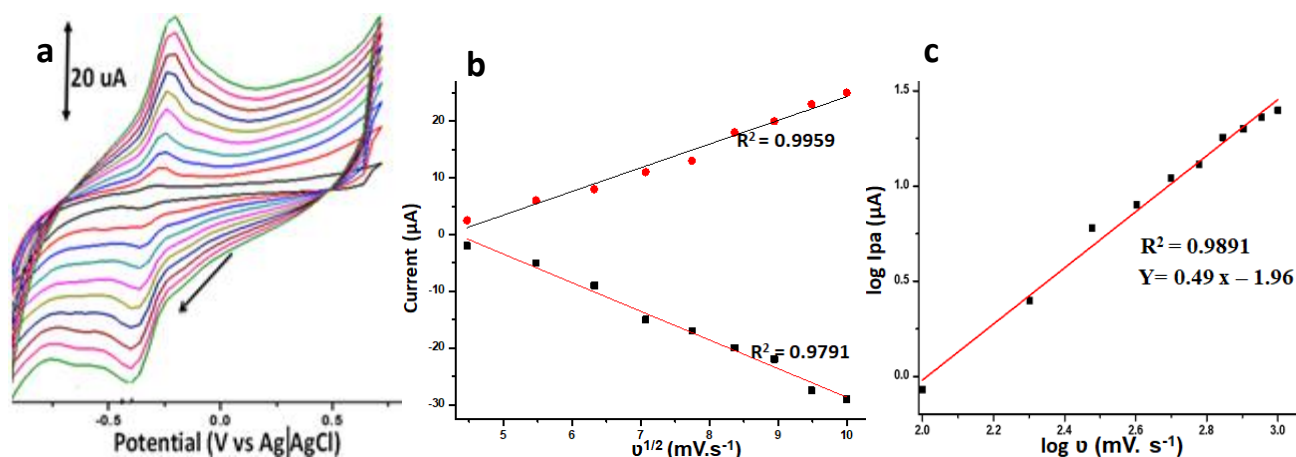


Fig 4.4: (a) Cyclic voltammograms of 0.2 μM MP at different scan rates (10 - 100 $\text{mV}\cdot\text{s}^{-1}$) on GQDPE in 0.1 M PBS at pH 7, (b) corresponding peak current variation with square root of scan rate and (c) corresponding logarithm peak potential variation with logarithm of scan rate.

4.2.2 Electrochemical behaviour of MP on MO or MOH modified electrodes

The GQD paste did not homogenize well with the metal oxide or metal hydroxide nanoparticles. Therefore, MO and MOH modified GQDPE could not be fabricated and assessed for MP electrocatalysis. The use of an ionic liquid such as 1-butyl-3-methylimidazolium hexafluorophosphate ([BMIM]PF₆) as an alternative to the non-conductive paraffin oil could assist in homogenizing GQD paste with MO or MOH NPs.⁷

4.2.2.1 GQDs/Cu(OH)₂ and GQDs/Cu₂O modified glassy carbon electrodes

The electrochemical behaviour of MP was assessed on GQDs/CuO₂/GCE and GQDs/Cu(OH)₂/GCE. Fig 4.5(i) is the CV of a bare GCE in the presence of MP where no redox peaks were observed. This

indicates that MP undergoes surface passivation process at the bare GCE surface.¹² Fig 4.5(ii) shows a CV of GQDs/Cu₂O/GCE displaying a pair of redox peaks at $E_{pa} = -0.20$ V and $E_{pc} = -0.30$ V. The ΔE value was determined to be 50 mV and the current ratio was found to be 1.05. The redox peak observed at $E_{pa} = -0.8$ V is attributed to the reduction of oxygen and it does not affect MP catalysis.^{13,14} Fig 4.5(iii) shows the CV of GQDs/Cu(OH)₂/GCE in the presence of MP. A pair of redox peaks were observed at $E_{pa} = -0.22$ V and $E_{pc} = -0.30$ V. The ΔE was calculated to be 40 mV and the peak current ratio was determined to be 1.04 in accordance to a reversible process that is diffusion controlled. The GQDs/Cu(OH)₂/GCE showed a decrease in ΔE , indicating that no ohmic drop was experienced by the electrode. The GQDs/Cu(OH)₂/GCE also demonstrated slightly lower peak potentials and high current density compared to GQDs/Cu₂O/GCE suggesting a fast electron transfer and better catalytic nature towards MP detection. The GQDs/GCE modified with copper based nanoparticles possess low resistance of the charge transfer resulting in low ΔE values.¹⁵

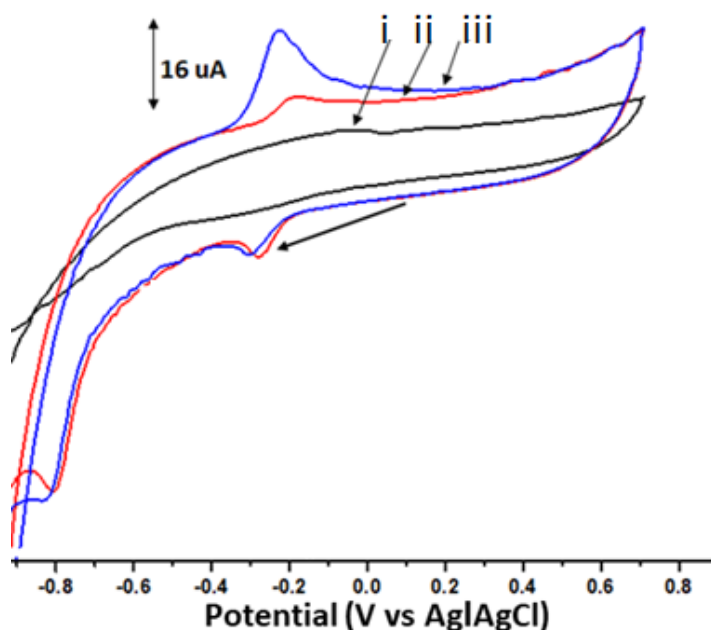


Fig 4.5: Cyclic voltammograms of 0.2 μ M MP on (i) bare GCE, (ii) GQDs/Cu₂O/GCE and (iii) GQDs/Cu(OH)₂/GCE, in 0.1 M PBS. Scan rate = 100 mV.s⁻¹.

Fig 4.6 shows the linear proportional relationship of I_{pa} and I_{pc} to the square root of scan rate for GQDs/Cu₂O/GCE (Fig 4.6a) and GQDs/Cu(OH)₂/GCE (Fig 4.6b), suggesting a diffusion controlled process on both electrodes.¹⁶ The logarithm plot of scan rate vs $\log I_{pa}$ for GQDs/Cu₂O/GCE (Fig 4.6c) and GQDs/Cu(OH)₂/GCE (Fig 4.6d) also revealed a linear relationship with a slope of 0.518 for Cu₂O and 0.501 for Cu(OH)₂ respectively, these values are in agreement with the theoretical slope of 0.5 for a diffusion controlled process.¹¹

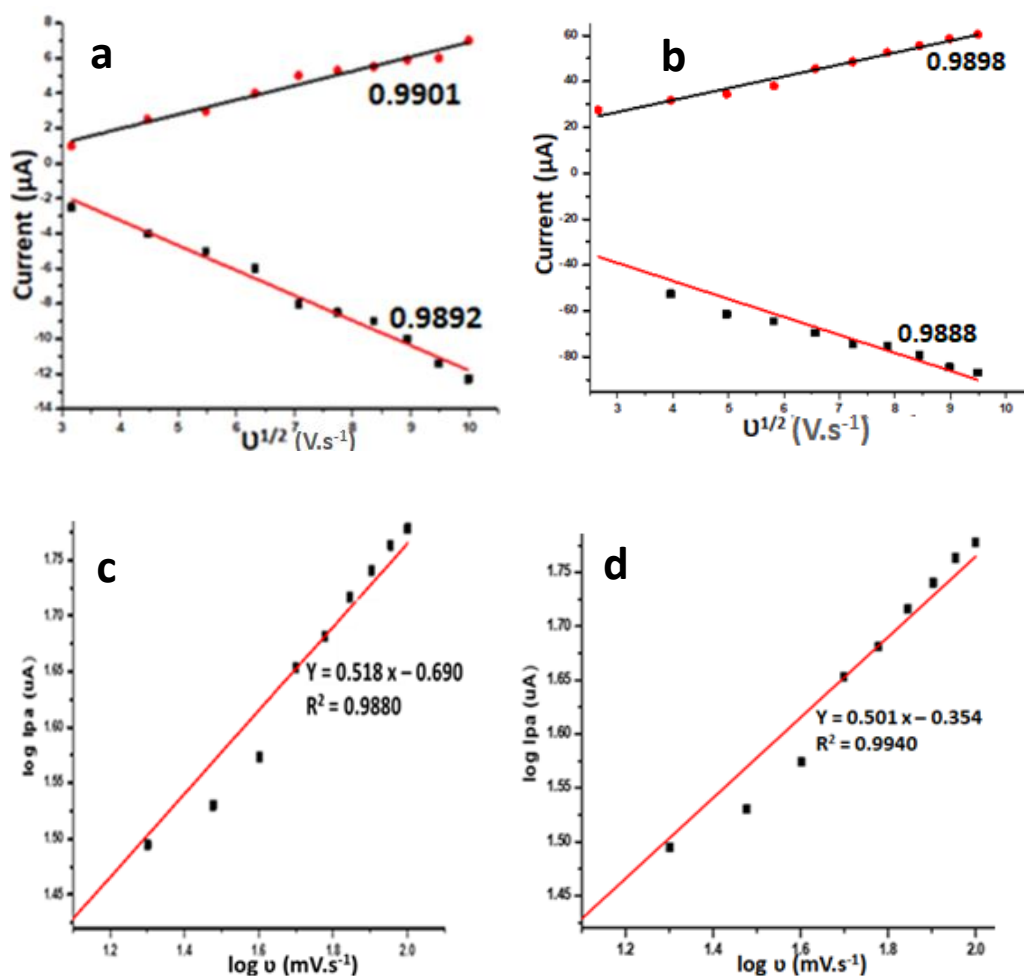


Fig 4.6: Plot of square root of scan rate vs peak current for (a) GQDs/Cu₂O/GCE and (b) GQDs/Cu(OH)₂/GCE. Plot of $\log v$ vs $\log I_{pa}$ for (c) GQDs/Cu₂O/GCE and (d) GQDs/Cu(OH)₂/GCE.

4.2.2.2 GQDs/Ni(OH)₂ and GQDs/NiO modified glassy carbon electrodes

Fig 4.7(i) shows the CV of a bare GCE displaying redox peaks at $E_{pa} = -0.29$ V and $E_{pc} = -0.245$ V with a ΔE of 45 mV. Fig 4.7(ii) shows redox peaks of MP on GQDs/NiO/GCE at $E_{pa} = -0.18$ V and $E_{pc} = -0.30$ V. The ΔE was calculated to be 60 mV and the current ratio was determined to be 1.04. The redox peak observed at $E_{pa} = -0.8$ V is attributed to the reduction of oxygen and it does not affect MP catalysis. When GCE was modified with GQDs/Ni(OH)₂ ΔE was determined to be 55 mV (Fig 4.7(iii)) and a current ratio was found to be 1.06. No significant increase in current densities of GQDs/Ni(OH)₂/GCE and GQDs/NiO/GCE was observed. This could be attributed to their similar particle sizes and the ohmic drop experienced by the electrode. An ohmic drop is the difference in potential needed to mobilize ions through a solution and it is attributed to a solution resistance.³ Therefore, an electrode experiencing high solution resistance will show a large ΔE and an electrode experiencing low solution resistance will show a low ΔE value. The increase in ΔE of GQDs/Ni(OH)₂/GCE compared to GQDs/NiO/GCE is also a result of an ohmic drop.

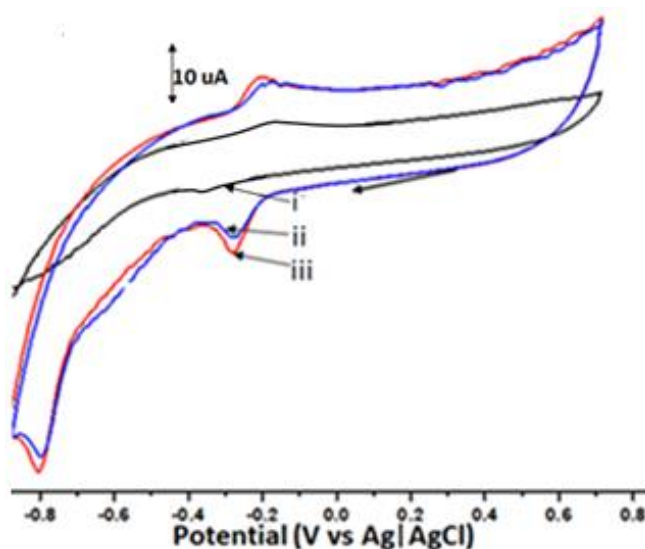


Fig 4.7: Cyclic voltammograms of 0.2 μ M MP on (i) bare GCE, (ii) GQDs/NiO/GCE and (iii) GQDs/Ni(OH)₂/GCE in 0.1 M PBS. Scan rate = 100 mV.s⁻¹.

Fig 4.8 shows the linear proportional relationship of I_{pa} and I_{pc} to the square root of scan rate for GQDs/NiO/GCE (Fig 4.8a) and GQDs/Ni(OH)₂/GCE (Fig 4.8b), indicating that the process is diffusion controlled for both electrodes. The diffusion controlled process was further confirmed by the logarithm plot of scan rate vs log I_{pa} for GQDs/NiO/GCE (Fig 4.8c) and GQDs/Ni(OH)₂/GCE (Fig 4.8d) which revealed a linear relationship with a slope of 0.472 for NiO and 0.493 for Ni(OH)₂ respectively.

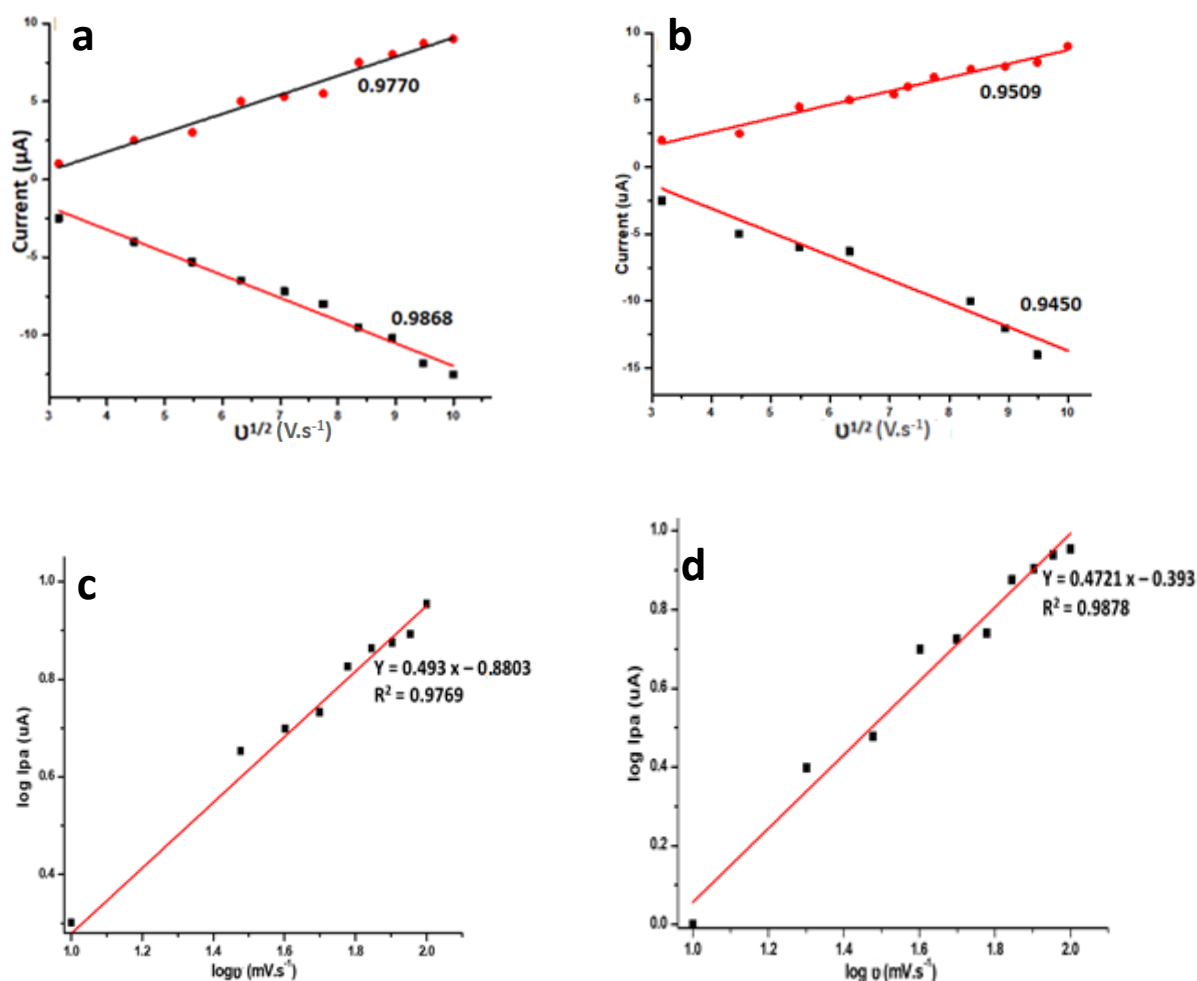


Fig 4.8: Plot of square root of scan rate vs peak current for (a) GQDs/NiO/GCE and (b) GQDs/Ni(OH)₂/GCE. Plot of log v vs log I_{pa} for (c) GQDs/NiO/GCE and (d) GQDs/Ni(OH)₂/GCE.

4.2.2.3 GQDs/Al(OH)₃ and GQDs/Al₂O₃ modified glassy carbon electrodes

Fig 4.9(i) shows the cyclic voltammograms of a bare GCE displaying redox peaks at $E_{pa} = -0.29$ V and $E_{pc} = -0.245$ V with a ΔE of 45 mV. The cyclic voltammograms of GQDs/Al₂O₃/GCE in Fig 4.9(ii) shows a pair of redox peaks of MP at $E_{pa} = -0.30$ V and $E_{pc} = -0.10$ V. ΔE was calculated to be 100 mV and the peak current ratio was determined to be 1.06. The redox peak observed at $E_{pa} = -0.8$ V is attributed to the reduction of oxygen and it does not affect MP catalysis. Fig 4.9(iii) shows the cyclic voltammograms of GQDs/Al(OH)₃/GCE displaying a pair of redox peaks at $E_{pa} = -0.21$ V and $E_{pc} = -0.28$ V. ΔE was calculated to be 70 mV and the peak current ratio was found to be 1.05. The increase in ΔE values of both modified electrodes is a result of a solution resistance¹⁷ experienced by the electrode, this is also shown by the lack of increase in current density of the GQDs/Al(OH)₃/GCE and GQDs/Al₂O₃/GCE.

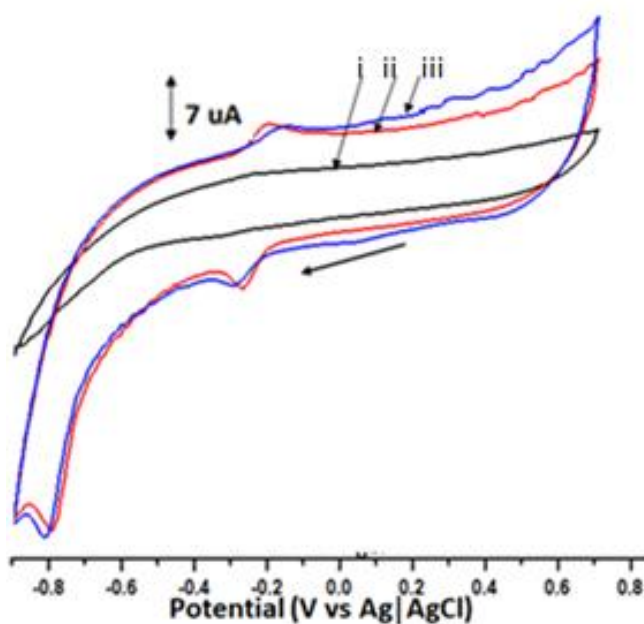


Fig 4.9: Cyclic voltammograms of 0.2 μ M MP on (i) bare GCE, (ii) GQDs/Al₂O₃/GCE and (iii) GQDs/Al(OH)₃/GCE in 0.1 M PBS. Scan rate = 100 mV.s⁻¹

The plot of I_{pa} and I_{pc} to the square root of the scan rate for GQDs/ Al_2O_3 /GCE (Fig 4.10a) and GQDs/ $Al(OH)_3$ /GCE (Fig 4.10b) displays a linear proportional relationship in accordance to a diffusion controlled process. This diffusion controlled process is also shown by the logarithm plot of scan rate vs $\log I_{pa}$ for of GQDs/ Al_2O_3 /GCE (Fig 4.10c) and GQDs/ $Al(OH)_3$ /GCE (Fig 4.10d), which demonstrates a linear relationship with a slope of 0.551 for Al_2O_3 and 0.543 for $Al(OH)_3$ respectively. This is in agreement with the theoretical slope of 0.5 for a diffusion controlled process.¹¹

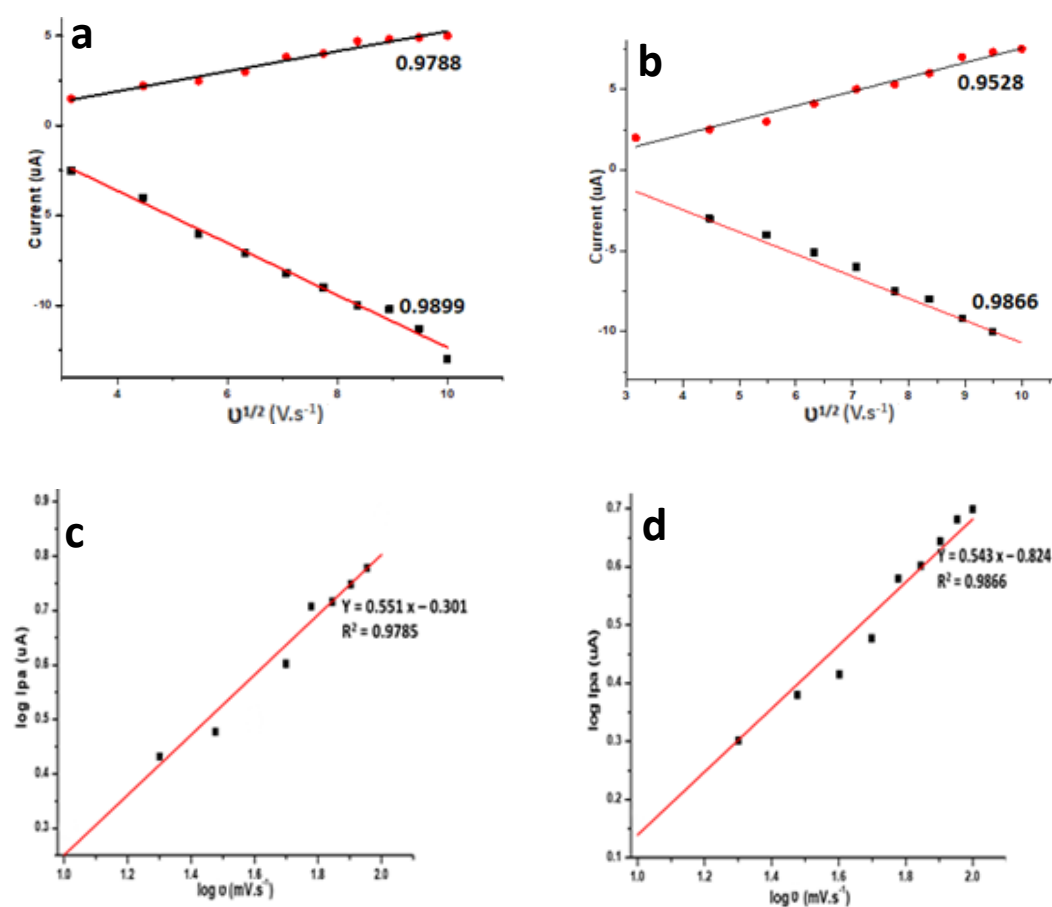


Fig 4.10: Plot of square root of scan rate vs peak current for (a) GQDs/ Al_2O_3 /GCE and (b) GQDs/ $Al(OH)_3$ /GCE. Plot of $\log v$ vs $\log I_{pa}$ for (c) GQDs/ Al_2O_3 /GCE and (d) GQDs/ $Al(OH)_3$ /GCE.

4.2.2.4 GQDs/Mn(OH)₂ and GQDs/MnO₂ modified glassy carbon electrodes

Fig 4.11(i) shows the cyclic voltammogram responses of a bare GCE displaying redox peaks at $E_{pa} = -0.29$ V and $E_{pc} = -0.245$ V with a ΔE of 45 mV in 0.1 M PBS. Fig 4.11(ii) shows the cyclic voltammograms of GQDs/MnO₂/GCE displaying redox peaks at $E_{pa} = -0.1$ V, $E_{pc} = -0.29$ V. The ΔE and peak current ratio were determined to be 95 mV and 1.10 respectively. The redox peak observed at $E_{pa} = -0.8$ V is attributed to the reduction of oxygen and it does not affect MP catalysis. Fig 4.11(iii) shows the cyclic voltammogram responses of GQDs/Mn(OH)₂/GCE displaying redox peaks at $E_{pa} = -0.31$ V and $E_{pc} = -0.14$ V. The ΔE was calculated to be 85 mV and the peak current ratio was found to be 1.09. These results suggested that both processes are reversible.^{18,19} No increase was observed in current densities of GQDs/Mn(OH)₂/GCE and GQDs/MnO₂/GCE, this could be attributed to their similar particle sizes and the solution resistance experienced by the electrode. The increase in ΔE values of both electrodes could also be a result of solution resistance.¹⁵

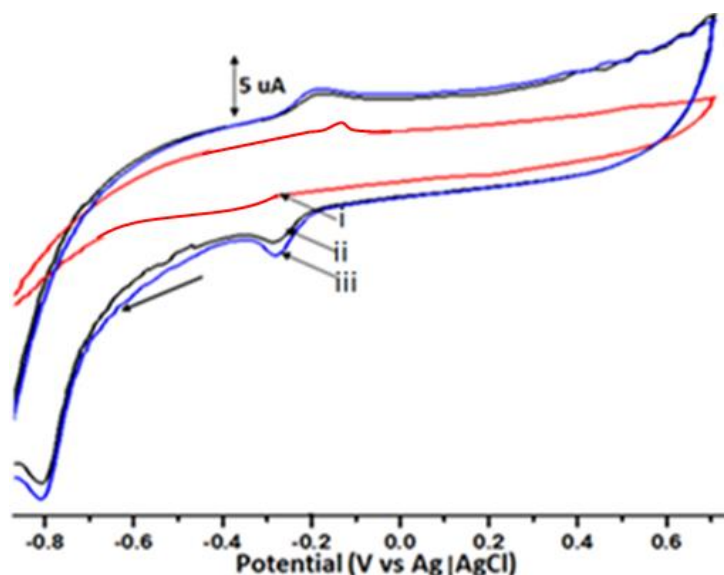


Fig 4.11: Cyclic voltammograms of 0.2 μ M MP on (i) bare GCE, (ii) GQDs/MnO₂/GCE and (iii) GQDs/Mn(OH)₂/GCE in 0.1 M PBS. Scan rate = 100 mV.s⁻¹.

The linear proportional relationship shown by the plot of I_{pa} and I_{pc} vs square root of scan rate for GQDs/MnO₂/GCE (Fig 4.12a) and GQDs/Mn(OH)₂/GCE (Fig 4.12b), proves the process to be diffusion controlled.¹⁶ The plot of logarithm of scan rate vs log of I_{pa} for GQDs/MnO₂/GCE (Fig 4.12c) and GQDs/Mn(OH)₂/GCE (Fig 4.12d) with a slope of 0.555 for Mn(OH)₂ and 0.563 MnO₂ respectively. This is in agreement with the reported theoretical slope of 0.5 for a diffusion-controlled process.¹¹

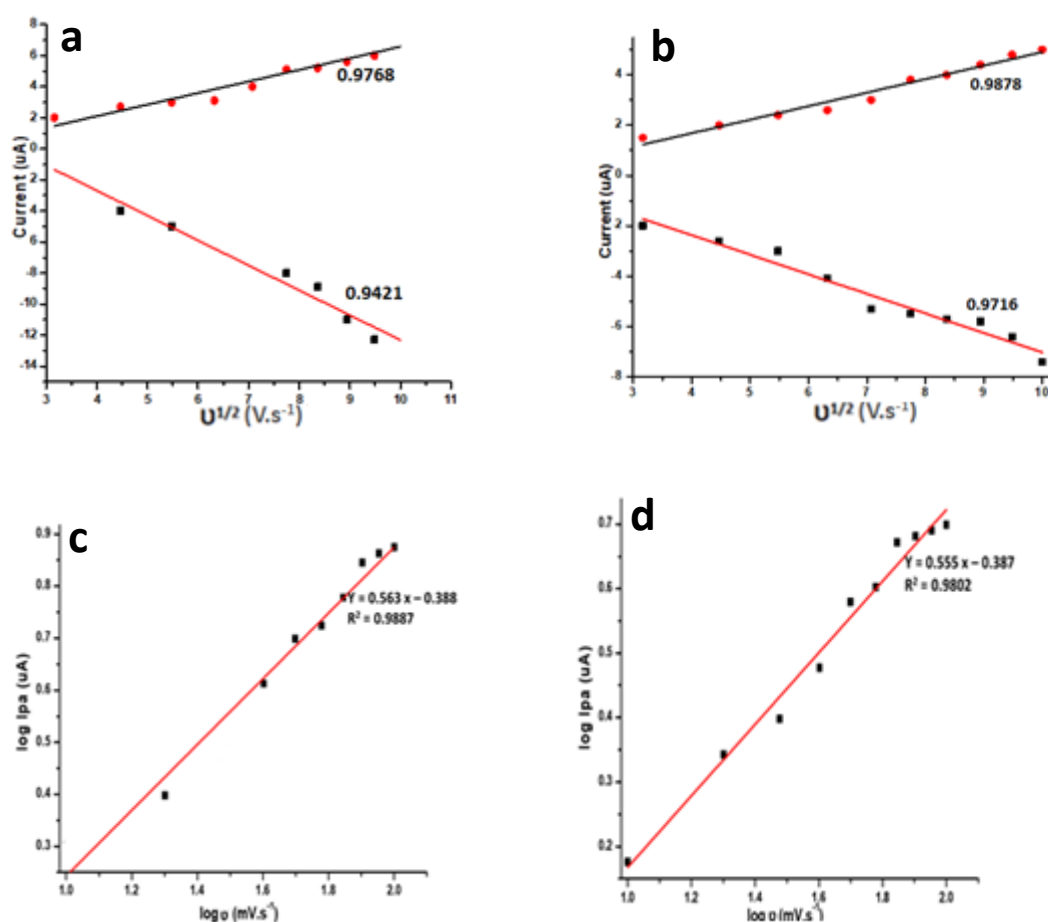


Fig 4.12: Plot of square root of scan rate vs peak current for (a) GQDs/MnO₂/GCE and (b) GQDs/Mn(OH)₂/GCE. Plot of log v vs log I_{pa} for (c) GQDs/MnO₂/GCE and (d) GQDs/Mn(OH)₂/GCE.

Table 4.2 shows the determined ΔE values of the modified electrodes, where GQDs/MO/GCE show increased ΔE compared to GQDs/MOH/GCE. This may be as a result of the big particle sizes of MO nanoparticles and the solution resistance experience the MO modified electrode.

Table 4.2: ΔE , current ratios and slope of $\log I_{pc}$ vs $\log v$ for MP on GQDs/GCE modified with relevant metal nanoparticles.

Metal nanoparticles	ΔE (mV)	Current ratio	Slope of plot: $\log I_{pa}$ vs $\log v$
Cu(OH) ₂	40	1.04	0.501
Cu ₂ O	50	1.05	0.518
Ni(OH) ₂	55	1.05	0.493
NiO	60	1.06	0.472
Al(OH) ₃	70	1.05	0.543
Al ₂ O ₃	100	1.06	0.551
Mn(OH) ₂	85	1.09	0.555
MnO ₂	95	1.10	0.563

Table 4.2 also shows the slope of $\log I_{pa}$ vs $\log v$ where it was observed that for all the electrodes the slope is approximately 0.5, this suggests that the overall rate of the reaction is diffusion-controlled on all modified electrode surfaces.²⁰ The GQDs/MOH/GCE exhibited excellent catalytic behaviour and conductivity compared to the GQDs/MO/GCE. This was demonstrated by the increase in peak current, low ΔE values and lower potentials.

4.2.3 Influence of MP concentration

4.2.3.1 GQDPE

The electrochemical responses of the GQDs, GQDs/MO and GQDs/MOH were investigated in various concentrations of MP (0.2 μM - 1.0 μM). The CVs of GQDPE shows an increase in redox peak current with increasing concentration. Fig 4.13b shows a linear response of concentration vs I_{pc} and all the modified electrodes displayed a similar behaviour.

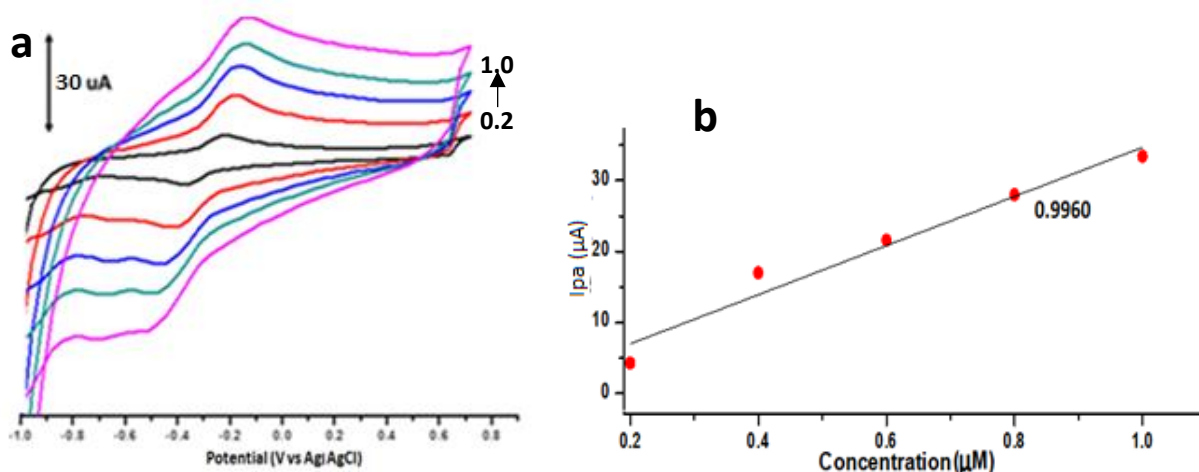


Fig 4.13: (a) Cyclic voltammograms of GQDPE in 0.1 M PBS containing different concentrations of MP and (b) the corresponding MP concentration vs current plot.

The limit of detection (LOD) and limit of quantification (LOQ) values shown in Table 4.3 were determined based on a signal (S)-to-noise (N) ratio equivalent to $S/N = 3$ and $S/N = 10$ respectively (see Appendix A).²¹ The LOD and LOQ describe the smallest concentration of an analyte where detection is possible to measure by this analytical technique. The LOD is the smallest concentration of an analyte that can be readily detected but not necessarily quantified as an exact value. LOQ is the concentration at which quantitative results can be reported using this technique with a high degree of confidence. The LOQ accounts for imprecision therefore it is at much higher concentration than the LOD.²¹ The sensitivity of the electrodes was calculated by dividing the slope of current vs concentration

by the surface area of the electrode (see Appendix A).²² A large surface area of the nanoparticles and nanocomposites enhances the sensitivity of the modified electrodes towards the analyte, therefore increasing the rate of electron transfer.¹¹ Also the electrical conductivity of an atom is directly proportional to its magnetic properties.²³ Magnetic properties of atoms can be classified as paramagnetic, containing unpaired electrons and diamagnetic, containing paired electrons.²⁴ Paramagnetic atoms are more electro-conductive than diamagnetic atoms. The GQDPE showed the lowest LOD and LOQ values compared to other electrodes for MP detection. The electrode sensitivity was determined to be 15.88 $\mu\text{A } \mu\text{M}$ indicating a fast electron transfer between GQDPE and MP as qualified by the high current density.

Table 4.3: LODs, LOQs and sensitivities for MP detection on modified electrodes.

Sensor	LOD (μM)	LOQ (μM)	Sensitivity ($\mu\text{A } \mu\text{M}$)
GQDPE	0.0046	0.0153	15.88
GQDs-Cu(OH) ₂ NPs	0.0095	0.0316	14.92
GQDs-Cu ₂ O NPs	0.015	0.0450	13.61
GQDs-Ni(OH) ₂ NPs	0.209	0.698	12.95
GQDs-NiO NPs	0.219	1.06	12.47
GQDs-Al(OH) ₃ NPs	0.166	0.452	12.24
GQDs-Al ₂ O ₃ NPs	0.204	0.580	12.13
GQDs-Mn(OH) ₂ NPs	0.226	0.819	11.12
GQDs-MnO ₂ NPs	0.230	0.826	11.04

4.2.3.2 GQDs/Cu(OH)₂ and GQDs/Cu₂O modified electrodes

Fig 4.14a and Fig 4.14b shows the current responses of GQDs/Cu(OH)₂/GCE and GQDs/Cu₂O/GCE in varied MP concentrations respectively. Both electrodes showed an increase in redox peak current with increasing concentration which is expected for diffusion controlled process. The calibration plots of copper based nanocomposites displayed a linear range of the concentrations vs I_{pa} as shown in Appendix A (Fig A1). The GQDs/Cu(OH)₂/GCE showed lower LOD and LOQ and higher sensitivity compared to GQDs/Cu₂O/GCE, this is a result of the small nanoparticle sizes of Cu(OH)₂ NPs. High sensitivity enhances vulnerability of the analyte towards the electrode therefore fast electron transfer kinetics occur as a result.¹¹ This is demonstrated by the high current density of GQDs/Cu(OH)₂ nanocomposite compared to GQDs/Cu₂O nanocomposite.

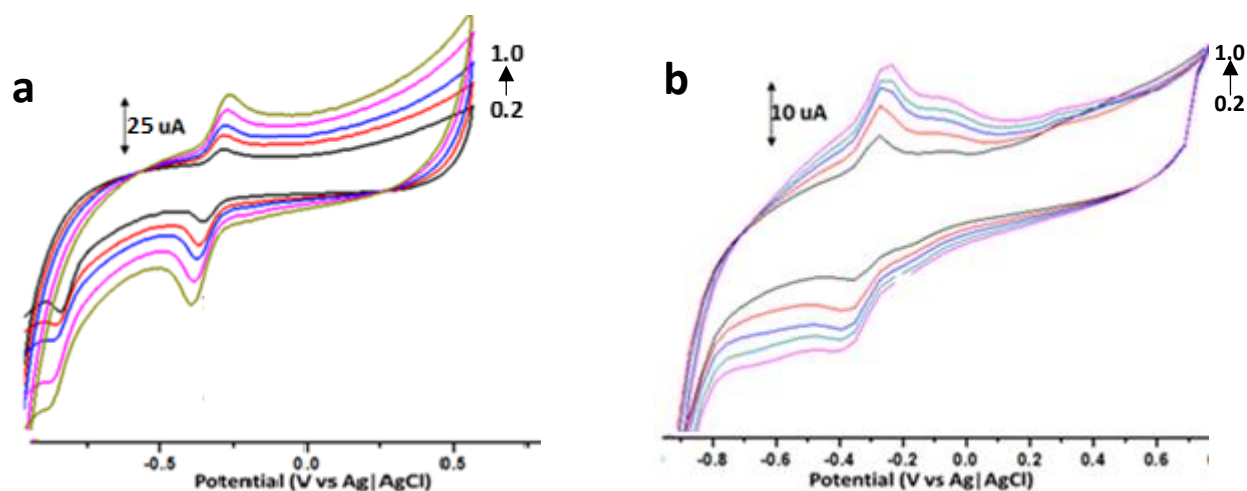


Fig 4.14: Cyclic voltammograms of (a) GQDs/Cu(OH)₂/GCE and (b) GQDs/Cu₂O/GCE in 0.1 M PBS containing different concentrations of MP. Scan rate = 100 mV.s⁻¹.

4.2.3.3 GQDs/Ni(OH)₂ and GQDs/NiO modified electrodes

Fig 4.15 shows the current responses of the GQDs/Ni(OH)₂/GCE (Fig 4.15a) and GQDs/NiO/GCE (Fig 4.15b) towards varied MP concentrations. The increase in current densities with increasing concentration was shown by the linear relationship of the I_{pa} vs concentration plot in Appendix A, Fig

A2. The GQDs/Ni(OH)₂ nanocomposite similar LOD and LOQ to GQDs/NiO nanocomposite, this is as a result of their similar nanoparticle sizes. The GQDs/Ni(OH)₂ and GQDs/NiO also showed similar sensitivities, this could be attributed to the fact that Ni(OH)₂ and NiO are both paramagnetic with the same oxidation state of 2+ and an electron configuration of [Ar]3d⁸ resulting in similar electrical conductivity. Oxygen and hydroxide ions are both weak field ligands therefore it is expected that NiO and Ni(OH)₂ behave similarly. The similar current densities of GQDs/Ni(OH)₂/GCE and GQDs/NiO/GCE suggest that electron transfer kinetics occurred at a similar rate therefore the electrodes demonstrated similar sensitivities towards methyl parathion.

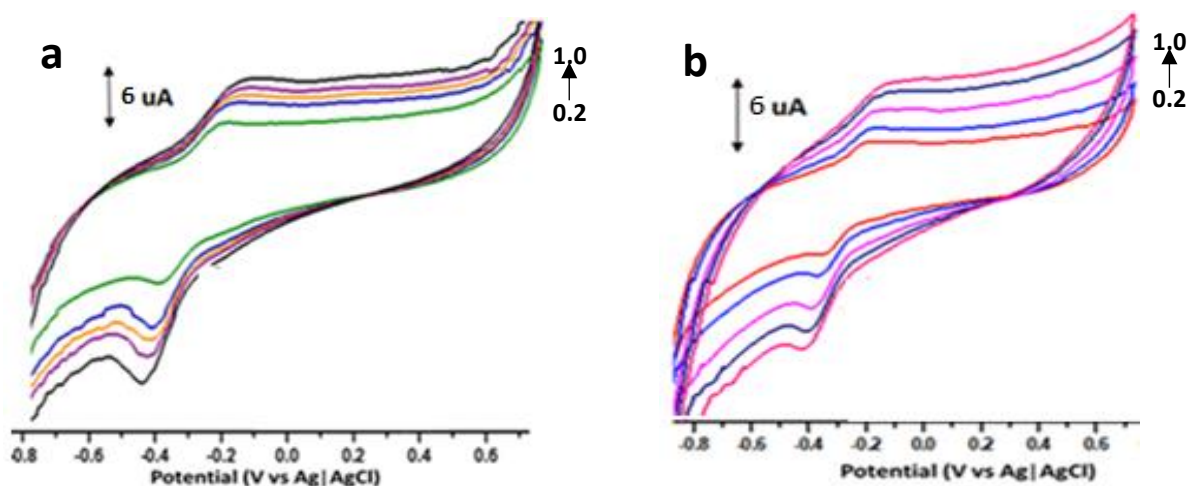


Fig 4.15: Cyclic voltammograms of (a) GQDs/Ni(OH)₂/GCE and (b) GQDs/NiO/GCE in 0.1 M PBS containing different concentrations of MP. Scan rate = 100 mV.s⁻¹.

4.2.3.4 GQDs/Al(OH)₃ and GQDs/Al₂O₃ modified electrodes

The GQDs/Al(OH)₃/GCE (Fig 4.16a) and GQDs/Al₂O₃/GCE (Fig 4.16b) displays current responses towards different concentrations of MP. The calibration plots of *I*_{pa} vs concentration in Appendix A, Fig A3 showed an increase in peak currents with increasing concentration for both the electrodes. The GQDs/Al(OH)₃/GCE showed lower LOD and LOQ compared to GQDs/Al₂O₃/GCE indicating that it can detect the analyte at lower concentrations. This behaviour is attributed to the large electroactive

surface area of GQDs/Al(OH)₃ modified electrode and its paramagnetism resulting in high sensitivity of the electrode towards the analyte. The GQDs/Al(OH)₃/GCE as a result is more sensitive compared to GQDs/Al₂O₃/GCE towards MP. This is demonstrated by the high current density which suggest that electron transfer occurred fast at the surface of GQDs/Al(OH)₃/GCE.

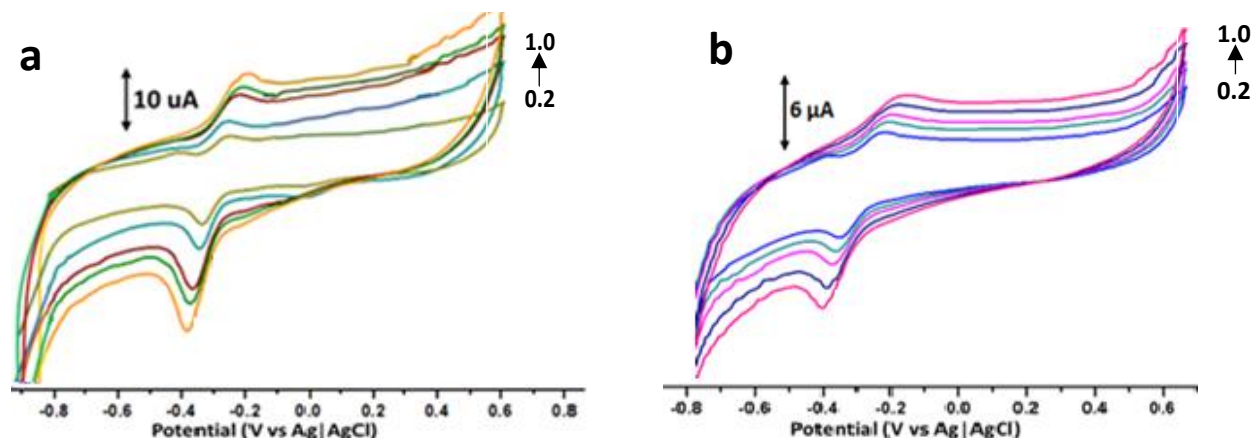


Fig 4.16: Cyclic voltammograms of (a) GQDs/Al(OH)₃/GCE and (b) GQDs/Al₂O₃/GCE in 0.1 M PBS containing different concentrations of MP. Scan rate = 100 mV.s⁻¹

4.2.3.4 GQDs/Mn(OH)₂ and GQDs/MnO₂ modified electrodes

Fig 4.17 show the current responses of GQDs/Mn(OH)₂/GCE (Fig 4.17a) and GQDs/MnO₂/GCE (Fig 4.17b) towards varied MP concentrations. The concentration vs I_{pa} calibration plot in Appendix A, Fig 4A displayed a linear relationship for both the electrodes as seen for previously modified electrodes. The GQDs/Mn(OH)₂ nanocomposite showed similar LOD and LOQ with GQDs/MnO₂ nanocomposite. This could be attributed to the similar nanoparticle sizes and the fact that both MnO₂ ([Ar]3d³) and Mn(OH)₂ ([Ar]3d⁵) are paramagnetic atoms with an oxidation state of 4+ and 2+ respectively, resulting in similar conductivity.²⁵ The electrodes therefore demonstrated similar sensitivities exhibited by the current densities which suggest that electron transfer kinetics occurred at a similar rates.

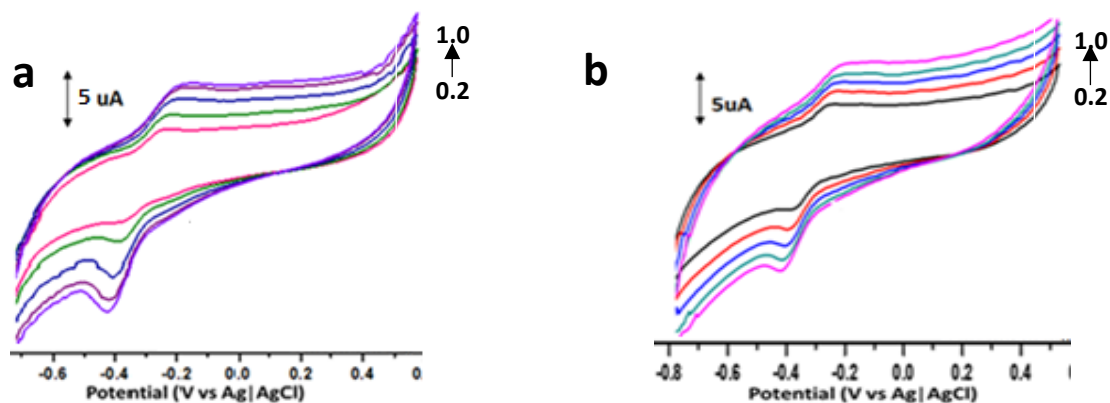


Fig 4.17: Cyclic voltammograms of (a) GQDs/Mn(OH)₂/GCE and (b) GQDs/MnO₂/GCE in 0.1 M PBS containing different concentrations of MP. Scan rate = 100 mV.s⁻¹.

The detection limit of GQDPE was determined to be 0.0046 μM which is significantly lower than the reported value of 0.21 μM at ZrO₂-NPs modified carbon paste electrode.²⁶ The ZrO₂-NPs CPE is regarded as the best electrode for MP detection due to the strong affinity ZrO₂-NPs have towards the phosphate group on methyl parathion. The GQDs/Cu(OH)₂/GCE showed the lowest LOD (0.0095 μM) and highest sensitivity (14.91 μA μM) for MP detection amongst all the other metal based nanocomposite modified electrodes. While the GQDs/MnO₂/GCE showed the highest LOD (0.230 μM) and lowest sensitivity (11.04 μM). This behaviour is due to the fact that copper is rated as the second most electrical conductive metal followed by aluminium, nickel and manganese.²³ Cu (II) is paramagnetic with an electron configuration of [Ar] 3d⁹ whereas Cu (I) is diamagnetic with an electron configuration of [Ar] 3d¹⁰. Single electrons tend to be more electrically conductive than paired electrons therefore GQDs/Cu(OH)₂ proved to be more conductive than GQDs/Cu₂O.

4.4 References

- (1) Parvin, M. H. *Electrochem. commun.* **2011**, *13* (4), 366–369.
- (2) Mphuthi, N. G.; Adekunle, A. S.; Fayemi, O. E.; Olasunkanmi, L. O.; Ebenso, E. E. *Sci. Rep.* **2017**, *7*, 43181.
- (3) Bard, A. J.; Faulkner, L. R. *Electrochemical methods : fundamentals and applications*; Wiley, **2001**.
- (4) Chirea, M. *Catalysts* **2013**, *3* (1), 288–309.
- (5) Huang, B.; Zhang, W. De; Chen, C. H.; Yu, Y. X. *Microchim. Acta* **2010**, *171* (1), 57–62.
- (6) Tukimin, N.; Abdullah, J.; Sulaiman, Y. *Sensors* **2017**, *17* (7), 1–12.
- (7) Bagheri, H.; Shirzadmehr, A.; Rezaei, M. *J. Mol. Liq.* **2015**, *212*, 96–102.
- (8) Gau, V.; Ma, S.-C.; Wang, H.; Tsukuda, J.; Kibler, J.; Haake, D. A. *Methods* **2005**, *37* (1), 73–83.
- (9) Liu, C.; Zhang, J.; Yifeng, E.; Yue, J.; Chen, L.; Li, D. *Electron. J. Biotechnol.* **2014**, *17* (4), 183–188.
- (10) Von Stackelberg, M.; Pilgram, M.; Toome, V. Z. *Elektrochem* **1953**, *57* (342), 1–44.
- (11) Boateng, A.; Cohen-shohet, R.; Brajter-toth, A. *Electroanalysis* **2010**, *22* (24), 2915–2923.
- (12) Liu, C.-Y.; Liu, Z.-Y.; Peng, R.; Zhong, Z.-C. *J. Anal. Methods Chem.* **2014**, *2014*, 724538.

- (13) Li, S.-J.; Xia, N.; Lv, X.-L.; Zhao, M.-M.; Yuan, B.-Q.; Pang, H. *Sensors Actuators B Chem.* **2014**, *190*, 809–817.
- (14) Arvand, M.; Gholizadeh, T. M.; Zanjanchi, M. A. *Mater. Sci. Eng. C* **2012**, *32* (6), 1682–1689.
- (15) Al-Qasbi, N.; Tahir Soomro, M.; Ismail, I. M. I.; Danish, E. Y.; Al-Ghamdi, A. A. *Arab. J. Chem.* **2015**.
- (16) Veeramani, V.; Sivakumar, M.; Chen, S.-M.; Madhu, R.; Dai, Z.-C.; Miyamoto, N. *Anal. Methods* **2016**, *8* (30), 5906–5910.
- (17) Hyodo, T.; Hashimoto, T.; Ueda, T.; Nakagoe, O.; Kamada, K.; Sasahara, T.; Tanabe, S.; Shimizu, Y. *Sensors Actuators, B Chem.* **2015**, *220*, 1091–1104.
- (18) Zaidi, S. A.; Shin, J. H. *RSC Adv.* **2015**, *5*, 88996–89002.
- (19) Jaiswal, N.; Tiwari, I.; Foster, C. W.; Banks, C. E. *Electrochim. Acta* **2017**, *227*, 255–266.
- (20) Shinagawa, T.; Garcia-Esparza, A. T.; Takanabe, K. *Sci. Rep.* **2015**, *5*, 13801.
- (21) Armbruster, D. A.; Pry, T. *Clin. Biochem. Rev.* **2008**, *29 Suppl 1* (Suppl 1), S49-52.
- (22) Adams-McGavin, R. C.; Chan, Y.; Gabardo, C. M.; Yang, J.; Skreta, M.; Fung, B. C.; Soleymani, L. *Electrochim. Acta* **2017**, *242*, 1–9.
- (23) Kasap, S.; Capper. *Handb. Electron. photonic Mater.* **2017**, *1*, 19–45.
- (24) Atkins, P. W. *Shriver & Atkins' inorganic chemistry*; Oxford University Press, **2010**.
- (25) Townshend, A. *Anal. Chim. Acta* **1987**, *198*, 333–334.

(26) Parham, H.; Rahbar, N. *J. Hazard. Mater.* **2010**, *177* (1–3), 1077–1084.

CHAPTER 5: Conclusion and future work recommendations

5.1 Conclusion

The work investigated the synthesis and use of graphene quantum dots and GQDs/MO and GQDs/MOH nanocomposites as sensing materials for the electrochemical detection of MP. The synthesis of the nanomaterials was achieved using standard synthetic methods. The characterisation techniques used in this work demonstrated that the GQDs NPs, MOH NPs, MO NPs were successfully synthesized. The MOH nanoparticles gave bigger nanoparticle sizes compared to the MO nanoparticles. The characterisation of the nanocomposites showed that both MOH and MO nanoparticles were well dispersed on the surface and in between the GQDs sheets. The GQDs and metal based nanocomposites displayed good electrochemical response towards MP compared to the GQD modified paste electrodes. The following catalytic pattern was observed: GQDPE > GQDs/MOH > GQDs/MO. The GQDs/MOH sensing nanomaterials demonstrated a wide linear concentration range (0.1 μM – 1.0 μM), low LODs (0.0095 μM – 0.226 μM), low LOQs (0.0153 μM – 0.816 μM) and high MP sensitivities (11.12 μM – 15.88 μM). The synergy effects of copper and graphene as one of the best electrical conductive materials resulted in GQDs/Cu(OH)₂/GCE best catalytic behaviour.

5.2 Future work recommendation

The study showed that GQDs/MOH nanocomposites showed best catalytic activity compared to the GQDs/MO nanocomposites for the detection of MP. There is not adequate work done using these metal based nanosensors and future recommendations include the use of these nanosensors for the detection of other organophosphate pesticides such as malathion and nitro phenols. Future work also involves selectivity studies with interfering carcinogenic species

such as nitro phenols and nitrobenzene which are found in the same matrix as MP. The other recommendation is to apply these nanosensors in real sample analysis.

APPENDIX A

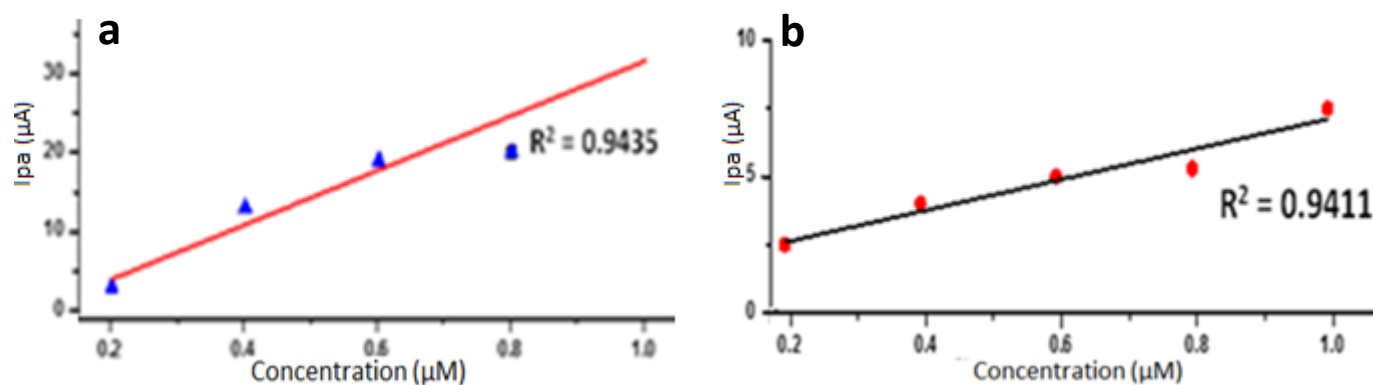


Fig A1: The concentration vs I_{pa} plot for (a) GQDs/Cu(OH)₂/GCE and (b) GQDs/Cu₂O/GCE.

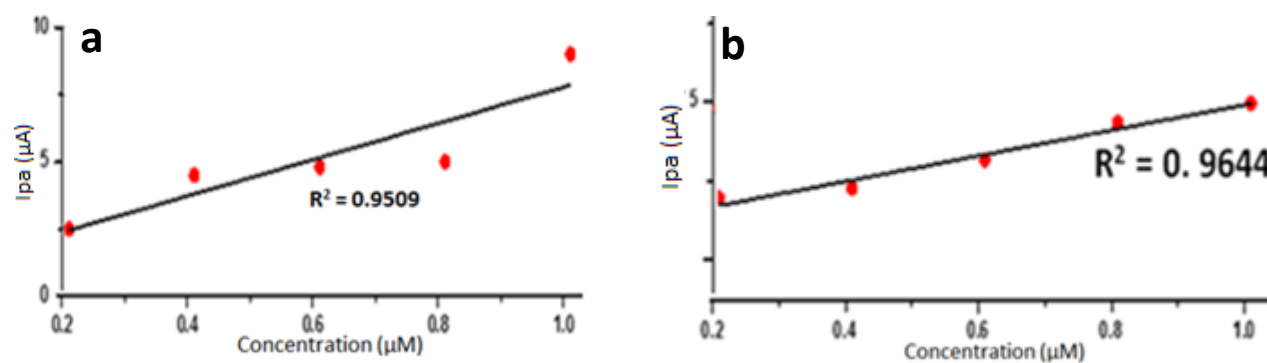


Fig A2: The concentration vs I_{pa} plot for (a) GQDs/Ni(OH)₂/GCE and (b) GQDs/NiO/GCE.

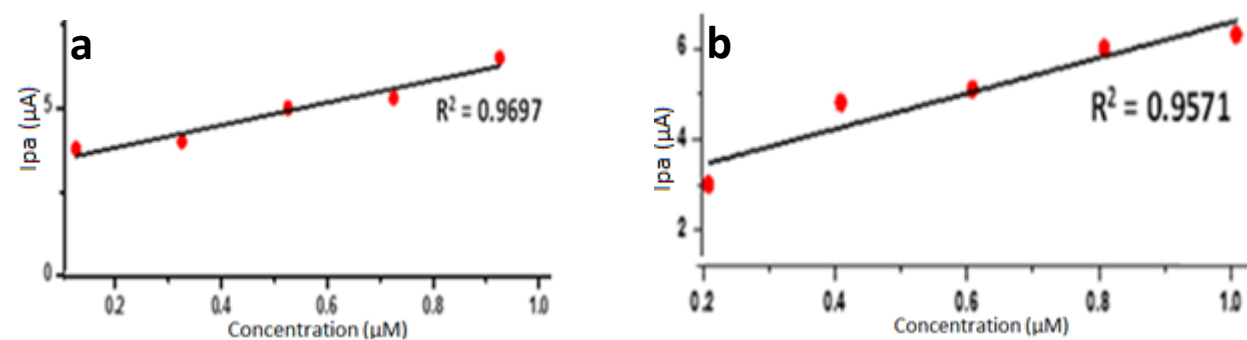


Fig A3: The concentration vs I_{pa} plot for (a) GQDs/Al(OH)₃/GCE and (b) GQDs/Al₂O₃/GCE.

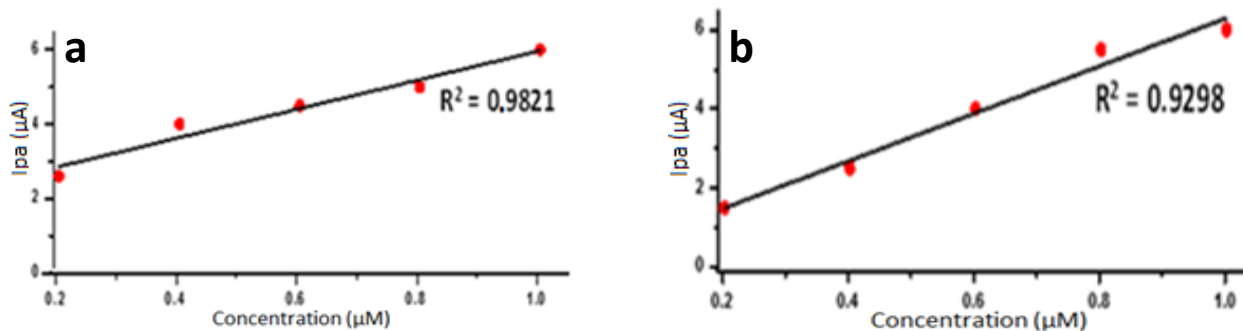


Fig A4: The concentration vs I_{pa} plot for (a) GQDs/Mn(OH)₂/GCE and (b) GQDs/MnO₂/GCE.

$$*LOD = 3 \times SD / S$$

$$*LOQ = 10 \times SD / S$$

LOD = Limit of detection, SD = standard deviation and S = Slope of current vs concentration

LOQ = Limit of quantification, SD = standard deviation and S = slope of the current vs concentration

$$*S = mx / Sa$$

S = sensitivity, m = slope of current vs concentration, Sa = the surface area of the electrode